THESIS

FLUID INTRACAVITY LASER DIODE (FILD) SENSOR

Submitted by

Dhiraj Kumar

Electrical and Computer Engineering Department

In partial fulfillment of the requirements

For the Degree of Master of Science

Colorado State University

Fort Collins, Colorado

Summer, 2005

COLORADO STATE UNIVERSITY

June 28, 2005

We hereby recommend that the thesis prepared under our supervision by Dhiraj Kumar entitled **'Fluid Intracavity Laser Diode (FILD) Sensor'** be accepted as fulfilling in part requirements for the degree of Master of Science in Electrical Engineering.

Committee on Graduate Work

Adviser

Co-Adviser (if applicable)

Department Head

ABSTRACT OF THESIS

FLUID INTRACAVITY LASER DIODE (FILD) SENSOR

Laser based microfluidic devices, especially ones in which a microfluidic channel is an integral part of the laser cavity, are very attractive for biomedical diagnostics applications. The fluid intracavity laser diode (FILD) sensor constructed in this research work is an electrically pumped vertical cavity surface emitting laser (VCSEL) based microfluidic device. It has the potential to detect different biological cells in a fluid.

The FILD sensor was constructed by attaching a bottom emitting VCSEL above an external dielectric mirror with an intervening ~10 μm thick photoresist spacer which forms the sidewall of the fluidic channel. The VCSEL contained a complete top DBR mirror and gain region, but only a partially reflecting bottom mirror so that the external dielectric mirror completed the resonator cavity. The external dielectric mirror was made on a BK7 polished substrate with a high reflective coating (~99%) at the laser wavelength (980nm). The sensor was assembled by heating the dielectric mirror with patterned photoresist at 125 °C and attaching the VCSEL die to the softened photoresist. The result was a closed fluidic cavity formed between the dielectric mirror and the VCSEL diode. This closed fluidic channel allowed fluids and other biological samples through the reservoirs to the cavity of the laser.

Lasing operation of FILD sensors were observed under CW and pulsed input current conditions. Output power vs. input current characteristics of various FILD sensors were

measured under pulsed, room temperature conditions, for different fluids inside the fluidic cavity. The majority of the sensors exhibited a trend of increase in slope efficiency and decrease in threshold current with increase in fluid index of the fluidic cavity. Spectral measurements of a FILD sensor were also performed, which showed ~1nm wavelength shift with change in homogeneous fluid index from 1 to 1.33. Modulation of transverse confinement of laser beam was also observed when 10μm diameter polystyrene spheres, used as prototype biological cells, were flown inside the FILD's fluidic cavity.

Several theoretical phenomena were investigated to explain the modulation trends of FILD's output characteristics due to change in fluid index. Complete qualitative and quantitative analysis of these phenomena are presented in the form of a thesis chapter and appendices.

Dhiraj Kumar
Department of Electrical and Computer Engineering
Colorado State University
Fort Collins, CO 80523
Summer 2005

Acknowledgements

I extend my sincere gratitude and appreciation to many people who made this Masters thesis possible. My foremost thank goes to my research adviser Dr. Kevin Lear. Without him, this thesis would not have been possible. I thank him for his patience and encouragement that carried me on through difficult times, and for his insights and suggestions that helped to shape my research skills. His valuable feedback contributed greatly to this thesis.

I am grateful to Linda Shao for working with me and providing her valuable suggestions in this project. I also thank her for allowing me to be a co-author in her publications.

I would like to convey my appreciation to my committee members, Dr. Jorge Rocca and Dr. Charles Henry for reviewing this thesis and providing their valuable comments.

I thank all my research associates at Colorado State University whose presences and fun-loving spirits made the otherwise grueling experience tolerable. They are: Abdul Matheen Raza, Raghu Vanga, Rohan Arora, Guangwei Yuan, Ahmad Al-Omari, Sulaiman Al-Sowayan, Zhiyan Liu, Adrienne Iguchi, and Bob Pownall.

Last but not the least, I thank my family and friends, for always being there when I needed them most, and for supporting me throughout these years.

Dhiraj Kumar

Table of Contents

Chapter 3

Literature Review and Previous Work Done At CSU

Chapter 7

Conclusions and future work

Appendices

Chapter 1

Introduction

1.1 Motivation

The developments in microfabrication technologies have had a tremendous impact on the progress of analytical systems for biology and chemistry. The integration of microfluidic systems (e.g., channels, mixers, and pumps) with chemical processes and analysis (e.g., fluorescence based chemical or biological assays, electrophoresis, etc.) has led to the realization of micro-total analytical systems (μ-TAS) [1,2]. The trend towards μTAS is also motivated by portability, automation, low volumes of samples required, low volumes of waste produced, and rapid detection. The main applications include detection of biological agents and monitoring bioprocesses. Many applications of μTAS are based on optical methods developed in conventional systems employing bulky and discrete elements like lasers, LEDs and detectors. The deployment of such optical systems coupled to μTAS has been cost prohibitive and impractical. Several groups have proposed the integration of photodetectors directly onto a biochip [3,4] but have not shown an integrated excitation source.

On the other hand, semiconductor microtechnology has reduced the size of a laser to the size of a biological cell (2-100μm). By integrating these ultra small lasers with μTAS, it is possible to create micro-electrical mechanical systems that will revolutionize the bio-detection and chemical processes involving optical methods of transduction [5-8].

The fluid intracavity laser diode (FILD) sensor presented in this thesis report has the potential to detect different biological cells in a fluid. It consists of a 100 μm aperture vertical cavity surface emitting laser diode integrated to a microfluidic channel on a glass substrate. It utilizes an optical method of intracavity spectroscopy [5-11] to detect and distinguish between different biological cells. It provides a common platform for all the lab-on-chip type laser based μTAS, for numerous applications based on optical methods like fluorescence based assays, optical tweezers, cell spectroscopy and interferometric methods. This thesis work presents successful construction of such a platform, and experimental data proving functionality of the first generation FILD sensor based on intracavity spectroscopy.

1.2 Summary of research work done in this thesis

In this thesis work, an electrically pumped vertical cavity surface emitting laser diode is successfully integrated to a micro-fluidic channel to construct a fluid intracavity laser diode (FILD) sensor. The sensor system is tested for output power-input current characteristics for different fluids inside the fluidic cavity. It was observed that the laser's threshold current and slope efficiency is modulated by changes in fluid index of the fluidic cavity. The wavelength spectrum of the FILD sensor was measured for 10μm diameter polystyrene spheres as prototype biological cells inside the fluidic cavity. The spectroscopy results show modulation of laser spectrum with polystyrene spheres.

1.3 Organization of thesis

Chapter 2 provides the background information on certain topics that are directly associated with the FILD sensor. Since the FILD sensor is a photonic device, consisting of a vertical cavity surface emitting laser (VCSEL) diode operated under external cavity conditions, this chapter provides background information on three topics, which are photonic sensors, VCSEL diodes and external cavity applications of VCSELs. The first part discusses various types of photonic biosensors already in the market and their applications. It also presents the current research work going on novel photonic sensors. The second part provides a brief tutorial on VCSEL operation, construction and fabrication techniques. The third part talks about external cavity conditions in VCSELs and discusses some related published work.

Chapter 3 discusses the prior work done in constructing VCSEL based microfluidic cavity devices. It is also divided into three major parts. The first part reviews the work done on "biocavity lasers" by Dr. Paul Gourley at Sandia National Labs. The biocavity laser is another prototype device that has shown capability to detect and distinguish between different biological cells. The second part of this chapter discusses the work done by Tom Yu on an electrically injected vertical cavity surface emitting laser based microfluidic sensor. Tom was a Master's student in the Electrical Engineering department of Colorado State University during the years 2000-2002. The third part of this chapter presents the passive cavity microfluidic biosensor, which does not employ any active

photonic device like a VCSEL integrated to the microfluidic chip. Linda Shao, a PhD candidate in Electrical Engineering Department at CSU, is currently pursuing her research work in constructing such a sensor.

Chapter 4 presents the device structures of the FILD sensors and discusses the fabrication procedures in detail. Two different types of vertical cavity surface emitting laser diodes are used to construct the two FILD sensors. The fabrication methods and the associated challenges are discussed in detail in this chapter.

Chapter 5 discusses the experimental set up for testing FILD sensors. It presents preliminary experimental data that proves the functionality of the sensors. Spectroscopy data on polystyrene spheres that are used as prototypes for real biological cells is also presented in this chapter. It also discusses some of the experimental observations with different trends of measurements and briefly talks about the theoretical phenomena that support the trend of experimental data.

Chapter 6 is mainly concentrated on presenting a comprehensive study of the physics of the FILD sensor. It discusses the actual and simplified resonator configurations of the FILD sensor. Five different theoretical phenomena are presented and are qualitatively and quantitatively compared with the experimental data.

Chapter 7 gives a brief conclusion on the work done in this thesis. It also presents outline for some future work, which can improve the FILD sensor in terms of sensitivity and consistency.

References:

[1] David J. Beebe, Glennys A. Mensing, and Glenn M. Walker, *"Physics and applications of micorfluidics in biology"*, Annual review Biomedical Engineering, 2002, **4**, 261-286

[2] J.C. Rife, M.I. Bell, J.S. Horwitz, M.N. Kabler, R.C.Y. Auyeung, and W.J. Kim, *"Miniature valveless ultrasonic pumps and mixers"*, Sensors and acuators, 2000, **86**, 135-140

[3] M.L. Chabinyc, D.T. Chiu, J. Cooper McDonald, A.D. Stroock, J.F. Christian, A.M. Karger, G.M. Whitesides *"An Integrated fluorescence detection system in Polydimethylsiloxane (PDMS) for microfluidic applications"*, Analytical Chemistry, 2001, **73**, 4491-4498

[4] J.R. Webster, M.A. Burns, D.T. Burke, C.H. Mastrangelo, *"Monolithic capillary electrophoresis device with integrated fluorescence detector"*, Analytical Chemistry 2001, **73**, 1622–1626

[5] P.L. Gourley and A. E. McDonald, "Semiconductor microlasers with intracavity microfluidics for biomedical application", *Proc. SPIE* 2978, pp.186-196 (1997).

[6] K.E. Meissner, P.L.Gourley, T.M.Brennan, B.E.Hammons, and A.E.McDonald, "Intracavity spectroscopy in vertical cavity surface emitting lasers for micro-optical mechanical systems", *Applied Physics Letters*, **69**, pp 1517-1519 (1996)

[7] P. L. Gourley, *et al.*, "Detecting cancer quickly and accurately", *Proc. SPIE* 3912, pp.2-10 (2000).

[8] P. L. Gourley, "Biocavity laser for high-speed cell and tumor biology", *Journal of applied physics D,* **36** pp R228-R239 (2003)

[9] Tao (Tom) Yu, "Fabrication and characterization of electrically pumped VCSEL based interacavity fluidic biosensor" *Master's of science in electrical and computer engineering, Thesis report*, Colorado State University (2002)

[10] H. Shao, D. Kumar, S. Feld, and K. L. Lear, "Fabrication of a Fabry-Perot cavity in a microfluidic channel using thermocompressive gold bonding of glass substrates", to appear in *J. of Microelectro-mechanical Systems.*

[11] T.Yu, T.Ao, C. W. Wilmsen and K. L. Lear "Electrically pumped fluidic cavity (EPFC) VCSEL for the detection of biological agents", *Proc. SPIE 4994,* pg 206-215, San Jose, 2003

Chapter 2

Background: Photonic biosensors and VCSELs

INTRODUCTION

This chapter covers background information on photonic biosensors and VCSELs. It gives an overview of the various principles of optical biosensing and discusses the different types of photonic biosensors. It also discusses some of the novel sensing methods developed recently and presents the trend of current research in this field. This is followed by a brief tutorial on vertical cavity surface emitting lasers. The basic structure, operation and various fabrication techniques of a VCSEL diode are thoroughly explained. At the end of the chapter, some sensor applications of VCSELs are discussed, followed by a literature review on external cavity VCSELs. While writing this chapter, the author has used References 1 and 4 extensively. These references are handbooks on photonic biosensors written by Dr. Prasad and on VCSELs edited by Drs. Wilmsen, Temkin, and Coldren. Much of the material in this chapter is reproduced directly from these references. The author strongly recommends these handbooks to the readers as a great source of information and knowledge.

2.1 Photonic biosensors

Biosensors are analytical devices that can detect chemical or biological species or a microorganism or directly monitor a bioprocess and provide either qualitative or quantitative results about an analyte. The use of biosensors in the detection of toxins, bacteria or viruses and fight against the dangers posed by chemical and biological

terrorism is recently of great interest. Biosensors thus find a wide range of applications in:

- Clinical diagnostics
- Drug development
- Environmental monitoring (air, water, and soil)
- Food quality control

Biosensors have been in a great topic of research for many decades. Earlier, they were mainly based on concepts utilizing electrochemical response [1]. This type of sensor still tends to dominate the current commercial market. However, progress in fiber optics and integrated optics (such as channel waveguides and surface plasmon waves) and the availability of microlasers have made photonic biosensors a very attractive alternative for many applications.

A photonic biosensor, in general, utilizes a change in the amplitude, phase, frequency or polarization of light created by a recognition element in response to a physical change or the presence of a chemical or a bio-organism. Enhancement of the sensitivity and selectivity of the optical response is achieved by immobilizing a biorecognition element (such as an antibody or an enzyme) on an optical element such as a fiber or a channel waveguide.

The main components of a photonic biosensor are (i) a light source, (ii) an optical transmission medium (fiber, waveguide, etc.), (iii) immobilized biological recognition

element (enzymes, antibodies or microbes), (iv) optical probes (such as a fluorescent marker) for transduction, and (v) an optical detection system. Some important principles of photonic biosensing are discussed in the next section.

2.1.1 Principles of photonic biosensing

The two important principles involved in biosensing are biorecognition and optical transduction. They are discussed in this section together with the various geometries used for optical stimulation and collection of the transducer's optical response.

2.1.1.1 Biorecognition

The biorecognition elements are biological organisms such as enzymes, antibodies, and biological cells. They are often immobilized to increase their local concentration near an optical sensing element and to allow them to be reused. Some of the molecular bioreceptors used for biorecognition in biosensitization are described here.

Enzymes: Enzymes are microorganisms that selectively combine or react with specific reactants or antigens and thus provide selectivity in terms of biorecognition. In addition, the reaction of certain analytes/substrates with enzymes can also provide optical transduction by producing a product that absorbs at a different wavelength (change in absorption), or is fluorescent (fluorescence sensor).

Antibodies: Antibodies are proteins that selectively bind with an antigen or analyte because of their geometric (site) compatibility. Very often an antibody-antigen pair's

selective association in terms of their conformational compatibility is represented as a lock (antibody) and key (antigen) combination. This specific physical association can also produce an optical response that can be intrinsic such as a change in the optical property of the antibody or the antigen.

2.1.1.2 Optical transduction

Optical or photonic biosensing utilizes a wide variety of optical processes, in response to the presence of an analyte detected by a recognizing element or induced by an optical stimulation. Figure 2.1 lists some of the principal optical transduction mechanisms used for biosensing. In the words of Prasad [1] "Phase change produced by a change in the real part of the refractive index manifests itself as (i) a change of polarization of linearly polarized light, (ii) a change in the propagation characteristics, particularly in relation to a light-confining geometry such as a fiber or a planar channel waveguide, or (iii) a change in the optical field distribution, particularly at an interface."

Amplitude change derived from absorption, reflection, or other transmission loss mechanisms produces changes in the intensity of the sensing light. Frequency changes associated with biosensing utilize (a) fluorescence where the optical signal generated is at a Stokes-shifted frequency from the exciting (absorbed) light, (b) Raman scattering, which is again Stokes-shifted, but now by vibrational excitation, or (c) frequency shift by a nonlinear optical interaction mechanism such as second-harmonic generation."

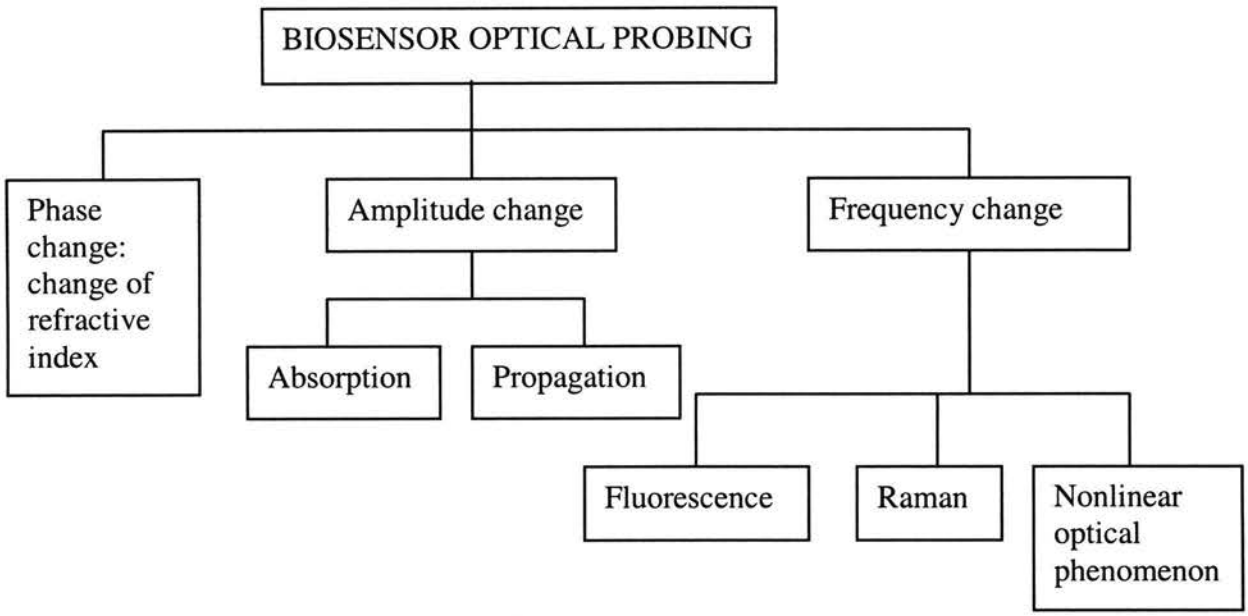

Figure 2.1 Optical transductions used for biosensiong (Reproduced from [1])

2.1.1.3 Optical geometries of biosensing

A number of optical geometries have been used in the design of various optical biosensors. Some commercially available optical sensor geometries are listed in Figure 2.2. The choice of any geometrical configuration depends upon the method of optical detection and the nature of bio-analytes. The main criteria upon which a geometrical configuration is chosen for a certain application are sensitivity and specificity of the analyte detection.

Optical fibers and planar waveguides utilizing guided wave geometries also provide an opportunity to use the evanescent waves that extend externally beyond the waveguiding region. "The evanescent waves are non-propagating optical fields whose strength decays exponentially as a function of distance away from the surface of the optical guiding

region. This evanescent wave can be utilized both for phase and amplitude modulation biosensors", as stated by Prasad [1]. Some other common optical geometries are discussed briefly in Section 2.1.3.

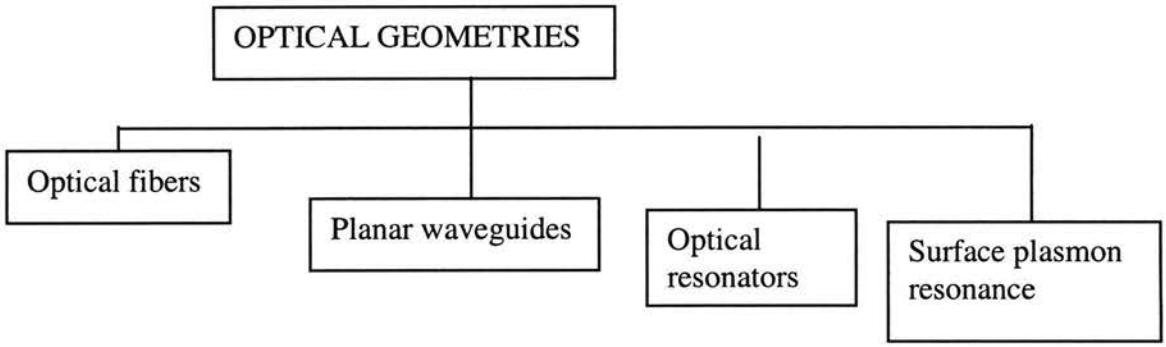

Figure 2.2 Commercial available optical sensor geometries (Reproduced from [1])

2.1.2 Immobilization and support for biorecognition elements

Immobilizing biorecognition elements at the detection sites helps in getting a stable optical response. The solid supports that are generally used to immobilize them usually include dielectrics like silicon oxide and silicon nitrides, membranes, polymers, copolymers or sol-gel processed glasses. They are immobilized generally by a physical method such as adsorption, absorption or by chemical attachment. In cases of evanescent wave sensing, the surface of a fiber or a waveguide itself acts as a solid support for biorecognition elements.

2.1.3 Types of photonic biosensors

This section discusses the different types of photonic biosensors that operate on the basis of above mentioned optical biosensing principles. They are the most common types of

photonic sensors that are commercially available for numerous applications. In this section, their basic construction and operation are briefly discussed.

2.1.3.1 Fiber optic biosensors

Fiber-optic biosensors are the most widely studied optical biosensors and have been a subject of extensive investigation over more than two decades. Fiber-optic biosensors offer a number of advantages. Some of these are listed here:

- Due to the development in fiber optic technology, optical fibers with many characteristics such as single-mode/multimode operation, and polarization preservation etc. are easily available. The accessibility of these well-defined characteristics has led to the applications of optical fibers in biosensing based on the principles discussed in Table 2.1.
- Longer length fibers provide greater surface area for analyte interaction and can further lead to an opportunity for multi-analyte detection.
- Optical fibers also offer compatibilities with catheters or endoscopes for in vivo biosensing. Thus, invasive optical biosensing methods can be used to measure in vivo blood flow, glucose content, and so on.

Fiber optic biosensors are further classified into two categories based on the role of the fiber for biosensing. They are (i) extrinsic fiber optic biosensors and (ii) intrinsic fiber optic sensors. In an extrinsic fiber-optic sensor, the optical fiber is simply used as a transmission channel to take light to and from the sensing elements. In an intrinsic sensor, the fiber itself acts as a sensing element (transducer) because one or more of the physical

properties of the optical fiber changes in response to the presence of an analyte. Another type of classification for fiber optic biosensors is based on whether a direct or indirect sensing scheme is used. In the case of a direct fiber-optic sensor, the intrinsic optical properties of the analyte are measured, while in the case of an indirect sensor, optical properties (absorbance, fluorescence) of an immobilized indicator dye, label, or optically detectable bioprobe is monitored.

2.1.3.2 Planar waveguide biosensors

Like optical fibers, planar waveguides are media in which the propagation of an optical waveguide is confined in a dimension comparable to the wavelength of light. In a planar waveguide the optical confinement can be in one or two dimensions in the form of thin films or ridge wavegudies respectively.

The three important techniques for coupling light into a planar waveguide are (i) prism coupling, (ii) grating coupling, and (iii) end-fire coupling. Just like an optical fiber sensor, a planar waveguide utilizes immobilization of the biorecognition element on its surface. Most planar waveguide sensors are evanescent wave sensors, described in the next section. The advantage of a planar waveguide sensor is that it allows the immobilization of multiple biorecognition elements, thus providing the prospect for multianalyte detection using a single substrate. Dr. Kevin Lear and some other members at Colorado State University are working on constructing such a multianalyte detection system on a silicon substrate using silicon nitride planar waveguides. The detection mechanism is based on analysis of evanescent electromagnetic waves modulated by bio-

analytes [16]. This approach utilizes patterns of immobilized biomolecules. A number of techniques have been used to create such a patterned structure. The most common techniques are photolithographic patterning and ink jet printing technology. Many different kinds of materials have been used for waveguides. They include silica glass, polystyrene, and Teflon. Depending upon the material used, different surface chemistry approaches have been used to immobilize a molecule on the surface of a waveguide.

2.1.3.3 Evanescent wave biosensors

Evanescent wave sensors utilize the interaction with the electromagnetic field (evanescent wave) that extends away from the surface of the light guiding medium, whether a planar waveguide, a channel waveguide, or a fiber. In other words, these sensors rely on the light that is not confined within the waveguide itself, but penetrates into the surrounding medium of lower refractive index (cladding or air or into a surface immobilized biorecognition element) and thus senses the chemical environment on the surface of the waveguide (or fiber). In contrast to a propagating mode (oscillating electromagnetic field), an evanescent wave has rapidly decaying electric field amplitude, with an imaginary propagation constant. Evanescent wave biosensing can utilize a number of optical transduction mechanisms, such as fluorescence excitation, evanescent wave coupling, and spectroscopy.

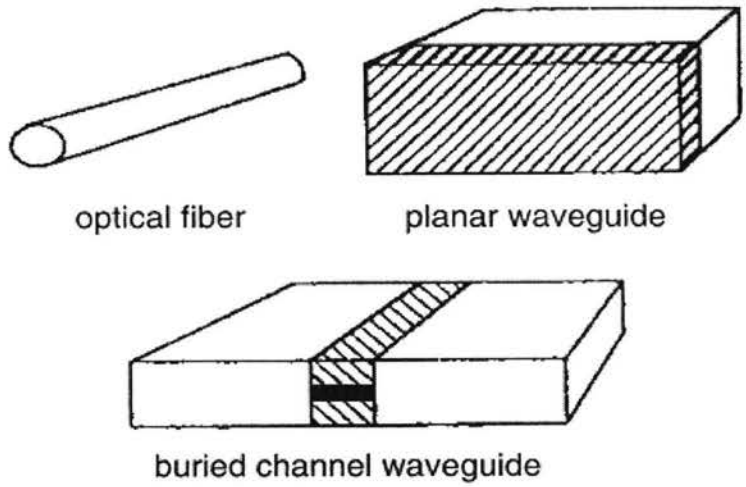

Figure 2.3 Typical examples of optical waveguides [1]

2.1.3.4 Interferometric biosensors

In the words of Prasad, "An interferometric biosensor utilizes interference between the light from a waveguiding channel with a sensing layer on its surface, and that from a reference channel. In this type of sensing, the phase of the sensing beam is modulated by binding of an analyte with a biorecognition element, immobilized on the surface of the sensing waveguide channel. This phase change is detected by an interferometric technique by creating interference between the two beams." The Mach-Zehnder interferometer has been most commonly used for constructing interferometric biosensors. Figure 2.4 shows the schematics of such a biosensor. The two arms of the interferometer are made exactly identical, so that there is no initial phase difference at the output. When the binding of antigen to the biorecognition element modulates the phase of the sensing beam, interference occurs between the reference and sensing beam and the output intensity is modulated.

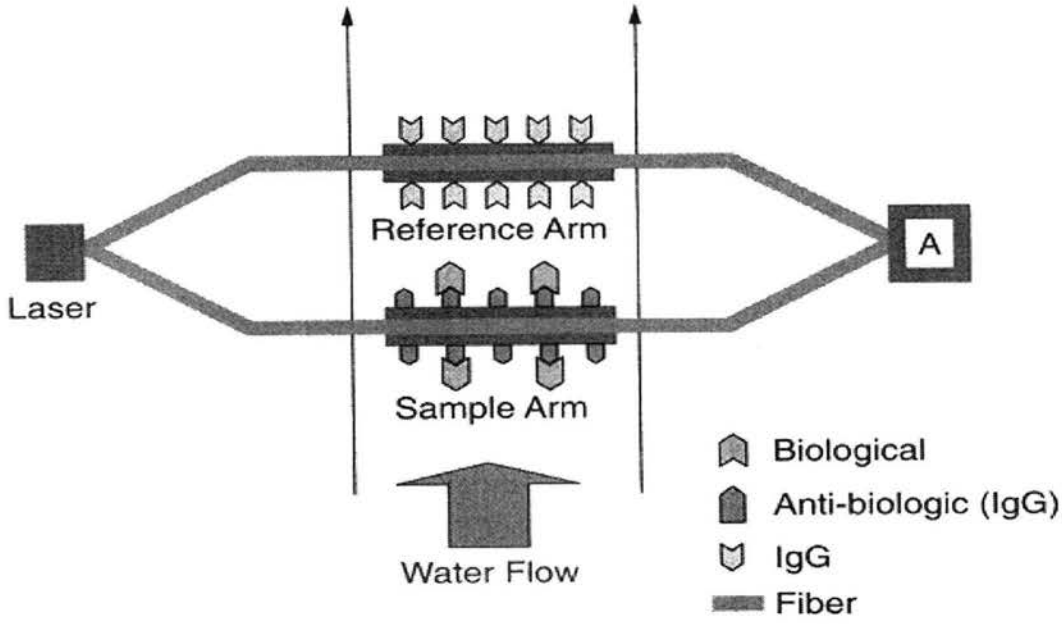

Figure 2.4 Mach Zehnder interfometer based biosensor [1]

2.1.3.5 Surface plasmon resonance biosensors

Surface plasmon resonance (SPR) biosensing technique is an extension of evanescent wave sensing as described earlier, except that a planar waveguide is replaced by a metal-dielectric interface. "Surface plasmons are electromagnetic waves that propagate along the interface between a metal and a dielectric material such as organic films. Since the surface plansmons propagate in the frequency and wave-vector ranges for which no light propagation is allowed in either of the two media, no direct excitation of surface plasmons is possible", as quoted by Prasad. The most commonly used method to generate a surface plasmon wave is attenuated total reflection (ATR).

SPR sensors work by launching a polarized light beam at a totally internally reflecting surface within a piece of glass, which has been metallized on the outside. This creates two optical paths: an evanescent wave created by the total internal reflection process, and a wave propagating in the metal. At the correct angle of incidence the interaction between these two waves, neither of which is directly detectable, creates a drop in the light reflected from the surface - and this is detectable.

To use the device as a sensor, a thin coating is employed whose thickness or optical index changes when it adsorbs the molecule to be sensed. The presence of that molecule causes a detectable change in the reflected light.

2.1.4 Novel sensing methods

Although there are numerous examples of novel optical biosensing techniques developed in the past decade, this section however discusses only those, which are relevant to the work done in this thesis report. The biosensor reported here is basically a photonic device integrated to a microfluidic system, and can be used to detect some of the fluid's properties. For this reason, this section includes discussion of some other novel microfluidic devices, integrated to photonic devices either intrinsically or extrinsically.

The microfluidic application area has evolved tremendously in the last decade. Moving from traditional test-tube reactions and titerplate based tests to laboratories on a square centimeter is the next step in laboratory automation, resulting in tremendous advantages. The main benefits of using microfluidic applications include:

- Huge decrease in reagent consumption and waste; decreased cost per analysis;
- Results of analyses in a few seconds;
- Better controllable process parameters in chemical reactions;
- Enabling of portable analysis systems;
- Increased resolution of separations.

It was less than a decade ago, when the researchers realized the potential of microfluidics and started integrating them to photonic devices to construct the so-called "micro-total analytical systems" or "lab-on-a-chip" type systems. The next few paragraphs discuss some novel photonic microfluidic sensors and the corresponding sensing techniques to provide the reader some intuition about the functionality of such types of biosensors.

2.1.4.1 Photonic crystal biosensors

Photonic crystals are relatively new to the world of photonic devices. They have emerged as important basic structures for the realization of a new class of optical waveguides, filters, optical interconnects, lasers and detectors. They are basically materials in which, the refractive index changes periodically, creating a bandgap at optical frequencies. These devices exploit defects, in an otherwise periodic lattice designed to exhibit a wide photonic bandgap. By using photonic crystals and artificially introduced defect states in photonic crystals, scientists and engineers can control spontaneous emission, bend light very sharply, and trap photons that can provide other important advances in optical technology.

Bhattacharya's group [2] have demonstrated the use of a two-dimensional photonic crystal slab waveguide in the design of microfluidic sensors, which can serve as building blocks for micron scale fluid and gas detection systems. The operation principle of these devices is based on the change in light transmission through a waveguide branch induced by the change of refractive index of a crystal defect with the fluid.

In another application, Domachuk et al [3] have demonstrated a method for using microfluidics to dynamically tune a photonic band-gap material. They fabricated a photonic crystal fiber and transversely probed it. An index matching fluid is thermally driven to tune the photonic band-gap of the crystal by discretely plugging the crystal voids. This method provides simple tunable functionality to air-void photonic crystals, both spatially and temporally. This methodology may be developed further into cost-effective fabrication techniques for tunable microphotonic components, filtering, or sensing devices.

2.2 VCSELS

In the 1970's, Iga et al from Tokyo Institute of Technology, Japan, first proposed the idea of a vertical cavity surface-emitting laser. This idea was instigated by the need to revolutionize the existing laser diode modules for fiber optic communication systems. A vertical cavity surface emitting laser is a semiconductor micro laser diode that emits light in a cylindrical beam vertically from the surface of a fabricated wafer. It has significant

advantages over conventional edge emitting lasers used predominantly for fiber optic communication systems. Its design allows the chips to be manufactured and tested on a single wafer. Large arrays of devices can be fabricated exploiting methods such as 'flip-chip' optical interconnects and optical neural network applications. In the telecommunications industry, its uniform, single mode beam profile is desirable for coupling into optical fibers. In the next few paragraphs, the basic structure, operation and different fabrication techniques of these devices are discussed.

2.2.1 Basic structure and operation

The basic physics governing the operation of a VCSEL is not different from that of other types of diode lasers. Current is injected into an p-n junction active region where stimulated emission provides gain for an optical mode that is confined by an optical cavity. The active region generally incorporates a stack of 3-5 pairs of quantum wells. The optical cavity length of a VCSEL is typically very short, 1-2 wavelengths of the emitted light. As a result, in a single pass of the cavity, a photon has a small chance of a triggering a stimulated emission event at high carrier densities. Therefore, a VCSEL requires highly reflective mirrors to be efficient. In an edge-emitting laser, the reflectivity of a facet is about 30%. For VCSELs, the reflectivity required for low threshold currents is greater than 99%. Such a high reflectivity cannot be achieved by the use of metallic mirrors or polished facets. As a result, VCSELs employ distributed Bragg reflectors (DBRs). A DBR is formed by laying down alternating layers of semiconductor or dielectric materials with a small difference in refractive index. Figure 2.5 shows the most basic structure of a VCSEL diode.

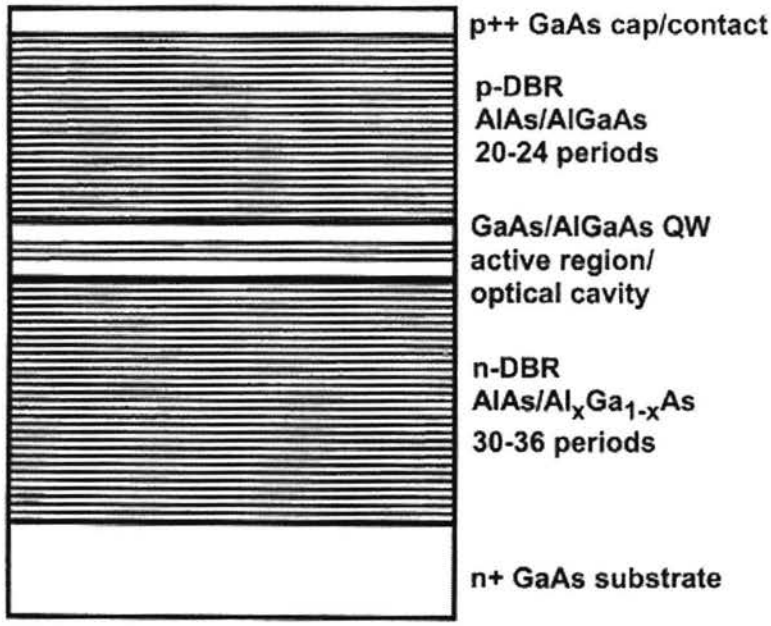

Figure 2.5 Basic structure of an AlGaAs-GaAs VCSEL [4]

2.2.1.1 Distributed Bragg reflectors

DBRs provide longitudinal confinement to the laser field. A DBR is basically a multilayer stack of alternate low and high refractive index material layers of specific thickness. It consists of several periods, where each period contains a high refractive index layer adjacent to a low refractive index layer. Light incident on a DBR stack is reflected back into the optical cavity from each interface of the stack The thickness of each layer in the stack is equal to $\lambda/4$, where λ is the wavelength in that layer. This is an important condition for all the reflections to interfere constructively. Thus a DBR accumulates reflections from all the interfaces, and combines them constructively to produce a net high reflectivity. The materials for the DBR layers are chosen such that

they have maximum index contrast to achieve high reflectivity from each interface, and at the same time they are transparent to the lasing wavelength. The layers can be made of dielectric materials, where a large refractive index difference between layers is possible, so that high reflectivity with a small number of DBR periods is obtained. However, in case of most of the epitaxially grown VCSELs, semiconductor materials are employed for constructing DBRs, as they allow current injection through them and they can be epitaxially grown over the gain region. The index contrast in semiconductor DBRs is not as high as in dielectric DBRs, which is compensated by using a larger number of layer pairs (>20) to achieve high reflectivity.

Electrical resistance is another important characteristic of a DBR, which is critical to the device performance. High resistance DBRs result in greater power dissipation and poor performance due to increased temperature. Electrical resistance of a DBR is attributed to the heterojunctions formed at the interfaces of the DBR, which inhibit carrier flow due to difference in bandgaps of layer materials. This problem can be solved by suitably doping the DBR materials, thereby increasing the free carrier concentration. However, the doping densities cannot be arbitrarily increased throughout the structure, because doing so also increases optical absorption. A more effective solution is the use of alloy grading at interfaces, often in conjunction with varied doping profiles such as increased doping at interfaces, delta doping, and modulation doping. Further details on DBR engineering can be found in reference [4].

2.2.1.2 Quantum well gain region

The typical length of the optical cavity of a VCSEL is about one wavelength. It contains the active region of the laser, which is basically a stack of very thin (~10nm) layers of direct bandgap semiconductor layers surrounded by barrier layers with a greater bandgap. The resulting offset in the conduction and valence bands between the lower bandgap semiconductor and barrier material confine the charge carriers and form quantum wells for carriers to recombine radiatively. The barrier layer semiconductor material is chosen in such a way that its bandgap is higher than that of active material and also its lattice constant matches closely with that of the active material, which prevents excessive tensile or compressive stress at the quantum wells. As shown in Figure 2.6, the quantum wells are positioned within the optical cavity to optimally overlap the antinodes of the electromagnetic field to provide the optical gain. The quantum well materials are selected to provide gain for the desired VCSEL emission wavelength. For example InGaP, AlGaAs, GaAs, InGaAs and InGaAsP are appropriate quantum well materials for VCSELs emitting near 650, 780, 850, 980 and 1300 nm respectively.

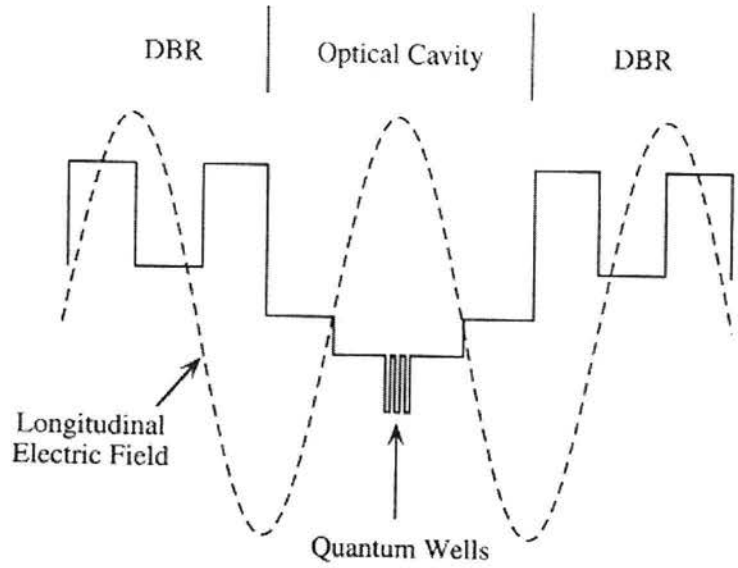

Figure 2.6 Refractive index profile and longitudinal electric field in the DBR and optical cavity within a VCSEL [4]

2.2.2 Fabrication techniques

The performance characteristics of VCSELs are strongly influenced by the epitaxial structure and fabrication processes that are employed. For example, for a particular VCSEL epitaxial structure, numerous devices can be fabricated which exhibit different performance characteristics by using at least four different fabrication techniques. The most generic parameters, which differentiate the performance of VCSELs fabricated by different techniques, are threshold current density, single mode/multimode behavior, thermal resistance and reliability. One of the important foci of VCSEL development has been towards reduced threshold current; therefore, processing technologies producing laser structures designed for enhanced transverse confinement have had significant impact. Figure 2.7 shows schematically the primary VCSEL structures that have been

demonstrated to provide transverse optical and/or electrical confinement: etched air post, ion-implanted, etched/regrown, and selectively oxidized VCSELs. These various laser structures require disparate fabrication technologies and exhibit differing electrical, optical, and thermal characteristics.

2.2.2.1 Etched air post VCSELs

The first demonstration of monolithic VCSEL diodes had etched air-post structures [4,5]. These are the simplest structures to fabricate and to confine electrical current in the transverse dimension. Different etching techniques were employed to remove epitaxial material around the laser cavity to construct air post structures.

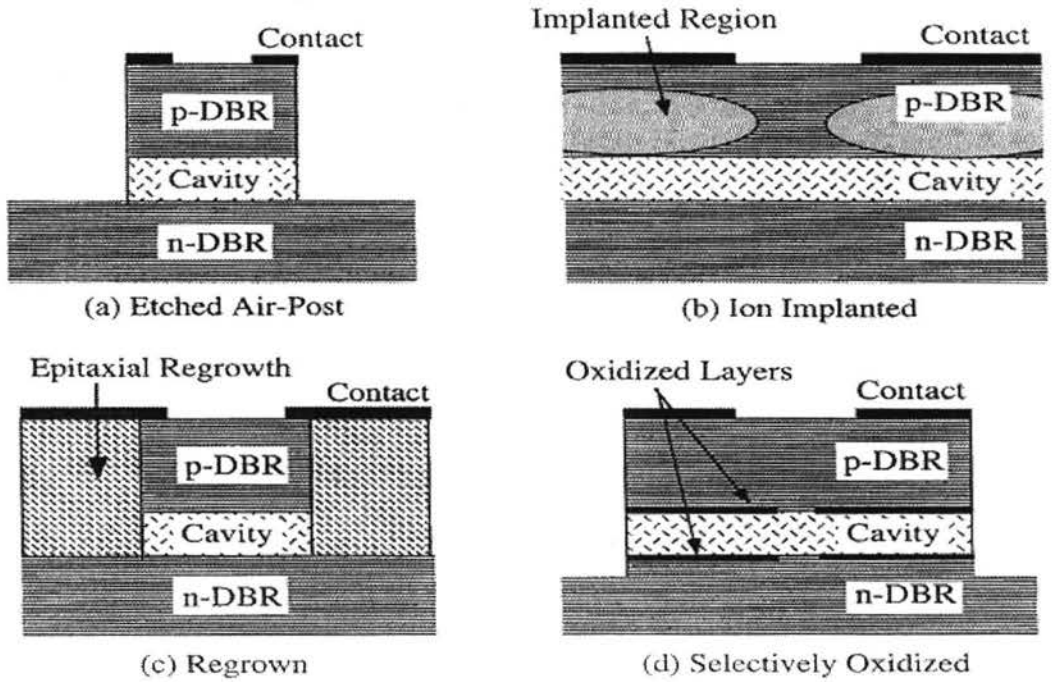

Figure 2.7 VCSEL device structures used for transverse optical and/or electrical confinement (a) etched air-post; (b) ion-implanted; (c) regrown and (d) selectively oxidized (Reproduced from [4])

Dry etching is particularly preferred over wet etching for most of the applications, as it results in a non-isotropic etching profile as opposed to large undercuts in isotropic wet etching. The air-post VCSEL structure influences several electrical and optical properties. First, the ability to define a pillar with a small diameter allows the fabrication of high-density ultra-low threshold current VCSELs. Secondly, as a consequence of strong index guiding present in air-post VCSELs, small cavity diameters are necessary to ensure a single transverse mode laser waveguide.

The electrical and the optical losses associated with air-post VCSEL structures are dependent upon the measure of etch depth. For example, loss in an air-post VCSEL that has been etched only into the top DBR mirror (shallow air-post) arises from diffraction caused by the longitudinal index variation and from current spreading away from the active region. On the other hand, losses in air-post VCSELs etched through the active region into the lower DBR mirror (deep air post) will suffer less from optical diffraction since the VCSEL is primarily surrounded by air, but will have a contribution from non-radiative recombination at the exposed sidewalls of the active region. For either etch depth, optical scattering from sidewall roughness will be significant as the cavity radius decreases. Lastly, due to absence of any heat sink material around the active region, an air-post VCSEL is subjected to an early output power rollover and lower modulation bandwidths. One means to increase the heat sinking is to encapsulate the air-post VCSELs with a material with higher thermal conductivity [4,6].

2.2.2.2 Regrown VCSELs

To achieve planar VCSEL structures, with efficient means of transverse electrical and optical confinement, was the next step in the development of VCSEL fabrication techniques. Regrown VCSELs are similar to the air-post VCSELs, except another processing step of regrowing semiconductor material around the laser cavity is added to the fabrication process. Regrowth around the laser cavity not only provides efficient transverse electrical and optical confinement, but also helps in passivation of the active region sidewall, and heat sinking. However the challenges, complexity and expense involved in the epitaxial regrowth on reactive high Al containing alloys used in VCSELs, are the major disadvantages of this fabrication technique.

2.2.2.3 Ion-implanted VCSELS

Ion implantation is another method to achieve electrical transverse confinement in a planar VCSEL topology. Implantation of ions into the top DBR mirror is used to render the material around the laser cavity nonconductive and thus to concentrate the injected current into the active medium as depicted in Figure 2.7(b). The ion implantation dose is chosen to sufficiently compensate the dopant impurities in the DBR, leading to regions of high resistivity. Various ion species have been employed (H+, O+, N+, F+), although proton implants are more common. The peak implant damage is usually designed to occur somewhat above the quantum wells to avoid excessive damage to the active region.

The damage from ion implantation provides only the transverse electrical confinement and no transverse optical confinement is manifest. Instead, an implanted VCSEL requires creation of a "thermal lens" at its center, which is thermally induced refractive index gradient that will support the lasing optical mode [4,7]. Hence the formation of the thermal lens determines how various transverse modes arise during VCSEL operation. As commonly observed for implanted VCSELs, the fundamental Gaussian mode arises initially at threshold, followed sequentially by higher order transverse optical modes with increasing injection current. Because the thermal lens aids the formation of the transverse optical mode, threshold currents of implanted VCSELs under pulsed and CW operation can vary significantly [4,8]. If the carriers are injected into the active region faster than the formation of the thermal lens, then the lasing threshold will be significantly higher due to greater diffraction loss in the cavity. The thermal characteristics of implanted VCSELs are relatively good, since their planar configuration provides good heat sinking. Thus in a nutshell, ion implanted VCSELs have the advantages of planar device geometry with enhanced heat sinking and excellent reliability. Their disadvantages include a lack of inherent optical confinement to support the lasing modes, which can lead to varying threshold currents and modulation limitations.

2.2.2.4 Selectively oxidized VCSELs

There is yet another way of providing transverse electrical and optical confinement in VCSEL diodes, and that is selective oxidation of buried layers. A VCSEL's layers are composed of AlGaAs alloys and exposing this alloy to temperatures from 350 to 500 deg C, converts them into a mechanically robust, chemically inert, insulating, and low

refractive index aluminum oxide [4]. The oxidation rate of this alloy depends upon the concentration of aluminum in the alloy, as it is the oxidized element. Wet oxidation of AlGaAs has been successfully employed in the fabrication of edge-emitting lasers [9] and has been applied to VCSEL fabrication also. The oxide layers within the selectively oxidized VCSELs effectively confine both electrons and photons and thus serve to define the transverse optical cavity.

Selectively oxidized monolithic VCSELs are fabricated by carefully designing the layers' compositions. In these VCSELs, one or more AlGaAs layers close to the active region are designed in such a way that their Al concentration is more than the other mirror layers. As a result, when the wafer is kept in the oxidizing environment, the lateral oxidation rate of these layers is faster than the other layers. The key idea here is to define an oxide aperture close to the active region of the laser diode, which not only provides electrical confinement, but also guides the photons generated by stimulated emission. Thus, for a given oxidation time and lateral extent of oxidation, variation of the oxide aperture area within a sample can be obtained using different mesa sizes.

Selectively oxidized VCSELs have numerous advantages over other gain guided and index guided counterparts, due to its enhanced electrical confinement. In conventional monolithic VCSELs, the DBRs are designed with special grading and doping profiles at the heterointerfaces to reduce their electrical resistance. However, by implantation or mesa etching, the low resistivity of these carefully engineered DBRs cannot be fully

exploited. In selectively oxidized VCSELs the current aperture is buried inside the top layers and the whole mirror stack can be used to conduct current into the device.

Selectively oxidized VCSELs are strongly index-guided, which profoundly influences the optical characteristics such as threshold current, transverse modes, and output beam stability. The refractive index of the buried oxide layer changes from 3.0 for the original AlGaAs layer to 1.6 for the oxidized layer [4], which induces a significant index difference between the laser cavity and the region surrounding the laser cavity. The index guiding in selectively oxidized VCSELs contributes to the reduced threshold current because of the reduced diffraction losses. Moreover, the reduced threshold current and voltage also reduces parasitic ohmic heating, leading to wider range of current operation and higher output power.

In spite of their superior performance, the reliability of selectively oxidized VCSELs is perhaps the most pertinent issue for VCSEL applications. The composition of the oxidized layer has been shown to impact the reliability of selectively oxidized VCSELs. Initially, some VCSELs employing oxidized AlGaAs layers exhibited rapid device degradation. The reliability issues of selective oxidized VCSELs are now understood thoroughly, and these devices have been available commercially for more than 5 years.

2.2.3 Novel sensing applications of VCSELs

2.2.3.1 Gas sensors

Apart from the most common applications in optical fiber communications, optical interconnects and smart pixel displays [4], VCSELs show promise for sensor applications also. For example, Zappe et al [10] demonstrated the use of VCSELs for optical detection of atmospheric oxygen in May 2000. They designed single mode 763nm wavelength VCSELs, with low noise and narrow optical linewidth. The wavelength spectrum of the laser is chosen in such a way that the fundamental absorption band of oxygen molecules overlaps with the tuning range of the VCSELs. Oxygen concentration is determined by using standard wavelength modulation spectroscopy and a special second-harmonic detection scheme with a l-m air path.

In a similar application reported by Cattaneo et al [11], a VCSEL was used to study the absorption spectrum of water vapor in the 940 nm region. Measurements were performed in ambient air at room temperature and in a hydrogen-oxygen flame over the temperature range of 1500-1800 K. The absorption spectra were well resolved, which demonstrated the feasibility of VCSEL based spectroscopic measurements of water vapor at room and high temperature in this spectral region.

2.2.3.2 Optical tweezers

VCSELs are also used for optical tweezer applications. In Dec 2002, Flynn et al [12] demonstrated the use of vertical cavity surface emitting lasers for optical trapping and active manipulation of biological cells and microspheres. It was experimentally verified

that the Laguerre-Gaussian laser mode output from VCSELs functions just as well as the traditional Gaussian fundamental laser mode for optically trapping biological cells and may be preferable, since the highest intensity of the Laguerre Gaussian mode is located at the outer ring of the optical aperture, allowing for the stronger optical confinement to be obtained for a lower total power. Using a 2 x 2 array of VCSELs, the simultaneous and independent transport of four human red blood cells was demonstrated indicating that much larger two-dimensional VCSEL arrays can be used as individually addressable optical tweezers in biological chips and systems.

2.3 External cavity VCSELs

One of the main motivations to include the topic of external cavity VCSELs in this thesis report is because the fluid cavity biosensor reported in this work is itself an external cavity VCSEL diode. Thus this topic will help the reader to develop a basic understanding of such types of devices. As the name suggests, the external cavity VCSELs have an external active or passive cavity, which provides optical feedback to the internal monolithic active cavity of the laser diode. So far, only passive external cavities have been reported to provide optical feedback to monolithic VCSELs, so this section restricts itself to the discussion of only passive external cavities. While the inclusion of an external passive cavity to a VCSEL diode complicates the resonator structure, it does have some special influence on the modal behavior of the laser diode. The next couple of paragraphs discuss the effects of external optical feedback to a VCSEL diode on the various characteristics of the laser beam. These are then followed by literature reviews of

some of the implementations of external cavity VCSELs and the challenges to construct such kinds of structures.

2.3.1 Motivation for external cavity VCSELS

Vertical cavity surface emitting lasers have been studied extensively over the past decade because of their useful characteristics such as a low threshold current, single longitudinal mode operation, circular output beam, and wafer-scale integrability. Because of these advantages, VCSELs are attractive as compact light sources for applications in optical communications and interconnects. One of the most important performance criteria for VCSELs in numerous applications is single mode behavior. A true single mode laser should emit a single longitudinal and transverse mode in only one determined polarization direction. While the longitudinal single mode operation is inherent to the short cavity design of VCSELs, transverse mode behavior depends strongly on layer structure and device size.

2.3.1.1 High single mode output power

It has been observed that proton implanted gain guided devices produce the largest single mode optical output when they are biased up to two times the threshold current. The other types of VCSEL structures, like air-post and selectively oxidized structure, do operate under single mode conditions, but only for very small device apertures due to strong index guiding. This restricts these devices to produce high levels of single mode output power. Unlike these devices, proton implanted devices exhibit a phenomenon called thermal lensing, due to which, only the fundamental order mode arises at the laser

threshold, and the other higher order transverse modes arise subsequently with an increase in injection current. This is because of the thermal index profile, which tends to promote the fundamental mode over other higher order modes. High single mode output powers of less than 5mW have been reported by many researches by using proton implanted devices. However certain applications like long haul fiber optic communications and diode pump lasers have single mode power requirements of hundreds of milliwatts. Unold et al and Mooradian et al from have demonstrated 10mW and 500mW of single mode output power respectively by adapting a similar technique, with two different methods [13]. This is explained in the next few paragraphs.

The higher order transverse modes from any gain-guided VCSEL device diffract at the gain region boundary and tend to diverge sooner than the lower order modes. If the cavity length is increased on one side of the active region, the diffraction losses suffered by these modes increases, and thus only the fundamental order mode propagates in the laser resonator. In other words, extending the cavity length enhances the diffraction losses inside the cavity and differentiates thresholds among the various transverse order modes. Thus with an increase in injection current, only the fundamental order mode gets stronger and the other modes do not, due to high diffraction losses, which results in a high power single mode operation. This technique is employed in external cavity VCSELs and long cavity monolithic VCSELs by Mooradian et al [13] and Unold et al [14] respectively, to achieve high power single mode operation.

Mooradian et al from Novalux Inc, have demonstrated a 980 nm bottom emitting proton-implanted device, putting out a 500mW single mode output with the help of an external cavity attached to it [13]. The schematic of the device structure is shown in Figure 2.8. The operation of the device is based on above explanation, and its structure is discussed as follows. The Novalux extended cavity surface emitting laser (NECSEL) uses a three mirror, coupled cavity design. Two of the mirrors are grown epitaxially on GaAs, similarly to conventional VCSELs

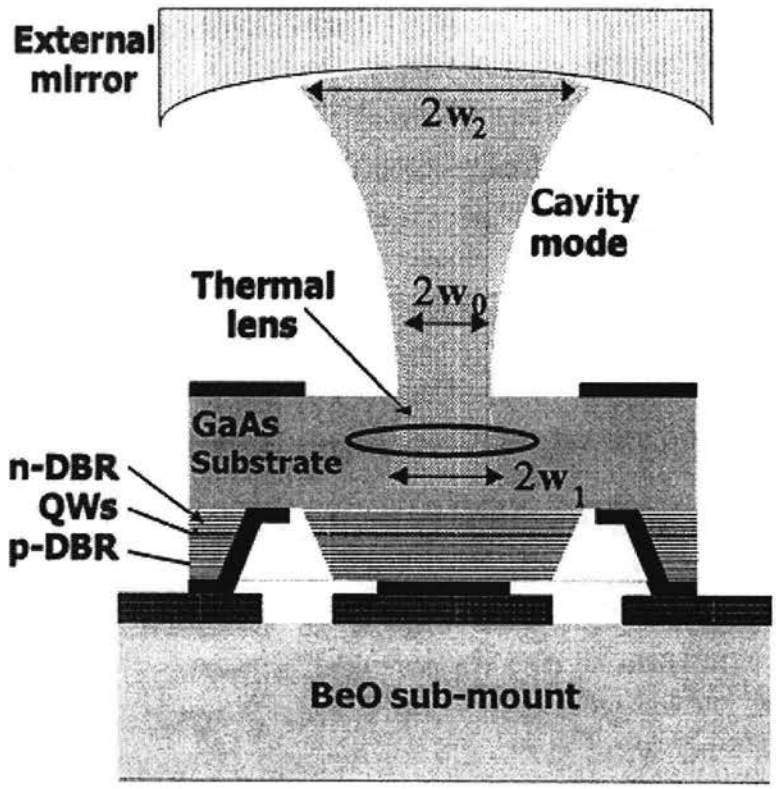

Figure 2.8 Novalux extended cavity surface emitting laser chip mounted on a BeO substrate mount and an external dielectric curved mirror completing the laser resonator (Reproduced from [15])

and the third mirror is a high reflective curved dielectric mirror placed external to the device. The proton implanted NECSEL chips are substrate emitting lasers with a highly reflective (~99%) top p-type distributed Bragg reflector (p-DBR) and an only partially reflective (~80%) bottom n-type DBR. The coupled cavity resonator is completed by an external dielectric mirror in front of the bottom n-DBR, as shown in the Figure 2.8. In this external cavity structured device, lasing occurs between the top p-DBR and the external dielectric mirror with multiple quantum wells providing the gain for lasing modes. The partial n-DBR basically helps in electrically injecting the diode and controlling the modal wavelength. It also reduces threshold gain by decreasing the amount of circulating power in the substrate and thus substrate loss. The external mirror can be adjusted to modulate the optical cavity length and thus a suitable cavity length to spatial mode diameter aspect ratio can be achieved. Thus, in these devices, the size of the active area, and therefore the available power, can be scaled with the size of the external cavity while maintaining fundamental mode oscillation. Further details about the NECSEL structure are presented Reference [13] or in Chapter 4 while discussing the NECSEL based fluidic cavity sensor.

2.3.1.2 Intracavity frequency doubling

Intracavity frequency conversion is not a novel technique to the world of lasers. Different solid-state and gas lasers have been extensively used to for successful generation of second or third harmonics. However due to monolithic nature of semiconductor diode lasers, the advantages of this technique could not be exploited with diode lasers. It was not until the proliferation of extended cavity diode lasers that researchers started to

realize the possibility of intracavity frequency multiplication in diode lasers. Mooradian et al from Novalux Inc. demonstrated 488nm coherent emission by intracavity frequency doubling of extended cavity surface emitting diode lasers. The device structure is similar to the one shown in Figure 2.6, except that a frequency doubling crystal is placed inside the external cavity. The Novalux extended cavity surface emitting laser diodes combines the beneficial characteristics of semiconductor and solid-state lasers. Similar to semiconductor laser diodes, they can be electrically pumped, utilize a high gain medium and can be mass manufactured. Like other VCSELs, they can be tested at the wafer level, have high efficiency over a wide temperature range, emit round beams, can be made into two dimensional arrays and are reliable. On the other hand, similarly to the solid-state lasers, the device's beam is controlled by an external cavity, which can incorporate frequency doubling non-linear crystals and still exhibit fundamental Gaussian mode operation.

NECSEL challenges for high single mode optical power:

Apart from some of the common issues involved in the fabrication of VCSEL diodes like thermal management, packaging and manufacturability, NECSELs face other critical challenges, which are unique to its device structure [13, 15]. They include: achieving uniform current density in the relatively large active region (~50 to 100μm) while maintaining lower optical loss and polarization control. The epitaxial portion of the diode is carefully designed and engineered to ensure low electrical and thermal resistances, low absorption and high reflectivity. Substrate doping is chosen to minimize carrier crowding in the gain region: a flat carrier profile gives efficient power extraction in a fundamental

spatial mode while keeping the optical absorption and electrical resistance low. Both, single sided and double sided chip designs provide sufficient current spreading to ensure a uniform current profile at the active region. The reflectivities of both the n-DBR and external mirror are carefully chosen depending upon the application. The presence of the n-DBR reduces the effective loss from absorption in the substrate and from any other intracavity elements, and controls the output wavelength. Its reflectivity is designed to provide sufficient circulating power in the external cavity for mode control. For high output power, the external mirror reflectivity is typically 70-90% while for intracavity frequency doubling, the same external mirror may approach 100% to maximize the intracavity circulating power.

NECSEL challenges for frequency doubling:

For intracavity frequency doubling, some other measures are carefully taken to ensure proper functionality of the device. The external output mirror is highly reflective at the lasing wavelength (976nm) and highly transmissive at 488nm to outcouple most of the blue light generated. The non-linear frequency doubling process is polarization sensitive, so some special polarization locking mechanisms are undertaken to ensure polarization stability. Further details on the various techniques used to construct Novalux extended cavity surface emitting lasers for frequency doubling applications can be found in reference [15].

2.4 Summary

This chapter provides background information on certain topics that are relevant to the subject matter discussed in this thesis report. This chapter will help the reader to develop an intuition about the subject discussed in this thesis, by providing a fairly good tutorial on the topics of photonic sensors, VCSELs and external cavity VCSELs.

References:

[1] Paras N. Prasad, "Introduction to Biophotonics" Chapter 9, page 311

[2] J. Topolancik, P. Bhattacharya, J. Sabarinathan and P. C. Yu, " Fluid detection with photonic crystal based multichannel waveguides", *Applied Physics Letters*, **82**, 1143-1145 (2003)

[3] Peter Domachuk, Hong C. Nguyen, and Benjamin J. Eggleton, "Tranvserse probed microfluidic switchable photonic crystal fiber devices", *IEEE Photonics Technology Letters*, **16**, 1900-1902 (2004)

[4] Carl Wilmsen, Henry Temkin and Larry Coldren, "Vertical Cavity Surface Emitting Lasers", Chapter 5, page 193

[5] J. L. Jewell, A. Sherer, S. L. McCall, Y. H. Lee, S. Walker, J. P. Harbison, and L. Florez, "Lwo threshold electrically pumped vertical cavity surface emitting lasers", *Electronic Letters"*, **25**, 1123-1124 (1989)

[6] K. D. Choquette, G. Hasnain, J. P. Mannaerts, J. D. Wynn, R. C. Wetzel, M. Hong, R.S. Freund and R. E. Leibenguth, "Vertical cavity surface emitting lasers fabricated by vaccum integrated processing", *IEEE Photonic Technology Letters*, **4**, 951-954 (1992)

[7] G. R. Hadley, K. L. Lear, M. E. Warren, K. D. Choquette, J. W. Scott, and S. W. Corzine, "Comprehensive numerical modeling of vertical cavity surface emitting lasers", *IEEE Journal of Quantum Electronics*, **32**, 607-616 (1996)

[8] K. L. Lear, R. P. Schneider, Jr., K. D. Choquette, and S. P. Kilcoyne, "Index guiding dependent effects in implant and oxide confined vertical cavity lasers", *IEEE Photonics Technology Letters,* **8**, 740-742 (1996)

[9] J. M. Dallesasse and N. Holonyak, Jr., "Native oxide stripe geometry AlxGa1-xAs-AlGaAs quantum well heterostructure lasers", *Applied Physics Letters*, **58**, 394-396 (1991)

[10] H. P. Zappe, M. Hess, R. Hovel, K. Gulden, H. P. Gauggel and F. M. di Sopra, "Narrow-linewidth vertical cavity surface emitting lasers for oxygen detection", *Applied Optics*, **39**, 2475-2479 (2000)

[11] H. Cattaneo, T. Laurila and R. Hernberg, "VCSEL based detection of water vapor near 940 nm", *Spectrochimica ActA Part A- Molecular and biomolecular spectroscopy*, **60**, 3269-3275 (2004)

[12] R. A. Flynn, A. L. Birkbeck, M. Gross and M Ozkan, "Parallel transport of biological cells using individually addressable VCSEL arrays as optical tweezers", *Sensors and Actuators B-Chemical,* **87**, 239-243 (2002)

[13] Eva M. Strzelecka, John G. McInerney, Aram Moorandian, Alan Lewis, Andrei V. Shchegrov, Dicky Lee, Jason P. Watson, Keith W. Kennedy, Glen P. Carey, Hailong Zhou, Wonill Ha, Brad D. Cantos, William R. Hitchens, David L. Heald, Vincent V. Doan, Kevin L. Lear, "High power, high brighness 980 nm lasers based on the extended cavity surface emitting lasers concept", *Proceedings of SPIE*, Vol. **4993**

[14] H. J. Unold, S. W. Z. Mahmoud, R. Jager, M. Kicherer, M. C. Riedl, and K. J. Ebeling, "Improving single mode VCSEL performance by introducing a long monolithic cavity", *IEEE Photonics Technology Letters*, **12**, 939-941 (2000)

[15] A. V. Shchegrov, D. Lee, J. P. Watson, A. Umbrasas, E. M. Strzelecka, M. K. Liebman, C. A. Amsden, A. Lewis, V. V. Doan, B. D. Moran, J. G. McInerney, A. Mooradian, "488 nm coherent emission by intracavity frequency doubling of extended cavity surface emitting lasers", *Procedings of SPIE,* Vol. **4994**, page 197-205, June 2003

Chapter 3

Literature Review and Previous Work Done At CSU

INTRODUCTION

In the years 1996 to 2003, Dr. P.L. Gourley from Sandia National Labs, published papers on biocavity lasers and their potential applications for determination of biological cell morphology by using intracavity spectroscopy [1-4]. These lasers are semiconductor devices based on VCSEL technology and they require optical pumping for their operation, which increases the cost and complexity of such systems, compared to directly injected diode lasers. Inspired by the ultimate goal of Gourley's research, and with the motivation to reduce the complexity and cost of such laser systems, some research initiatives were taken in the Electrical and Computer Engineering Department at Colorado State University as a part of a DARPA funded B.O.S.S. Optocenter. In the years 2000 to 2002, Tao Yu, a Master's candidate in the Department of Electrical and Computer Engineering, worked on fabrication of prototype biocavity lasers based on electrically injected VCSELs as opposed to optically pumped ones reported by Gourley. Two other students at Colorado State University, Hua (Linda) Shao (PhD candidate) and Dhiraj Kumar (myself) continued Tao's work from 2002 and pursued two different approaches to construct photonic devices for sensing biological cells. In this chapter, I summarize relevant papers published by Gourley and the work reported by Tao Yu in his thesis. I also discuss Linda's research work on passive Fabry Perot interferometer based microfluidic cavity biosensor and review some of her experimental results.

3.1 Optical pumped VCSEL based biosensor from Sandia National Labs

A typical laser used in biophotonics applications is used to irradiate external cells or tissues, e.g. for diagnosis by cytometery and fluorescence imaging and spectroscopy. In contrast, the biocavity laser reported by Dr. Gourley, [1] uses a cavity formed between a AlGaAs/GaAs surface emitting laser and an external dielectric mirror to enclose a single cell which acts as an internal waveguide and promotes lasing. This section is divided into three parts. The first part describes the structure of Gourley's biocavity lasers which is based on VCSEL technology, the second part discusses the basic theory of the biocavity laser, and the third part summarizes the results obtained by the group at Sandia National Laboratories (SNL).

3.1.1 Biocavity laser structure

The key idea behind constructing the biocavity laser device is to integrate a microfluidic channel within the cavity of a laser diode. In conventional monolithic vertical cavity surface emitting lasers, there is probably no way to integrate a microfluidic channel to the laser cavity, such that it becomes an integral part of the laser resonator. The only way to construct such kind of a device is to fabricate a half laser, integrate a microfluidic channel to the half laser and then complete the resonator by using an external mirror. Gourley's biocavity laser is constructed in a similar way. A half VCSEL is grown on a GaAs substrate, and consists of an epitaxial growth of a distributed Bragg reflector (DBR) followed by a multiple quantum well gain region near the surface of the wafer. An external dielectric mirror is then positioned just above this half VCSEL, with the thin intervening region serving as a microfluidic sample area. The VCSEL's bottom DBR

and external dielectric mirror form the laser resonator; with the quantum well gain region and a fluidic sample cavity being inside the resonator. This laser is then photopumped and lasing spots are observed in the regions containing cells, and the cells can be distinguished by their emission spectra [1]. Figure 3.1 shows the cross-sectional schematic diagram of Gourley's biocavity laser.

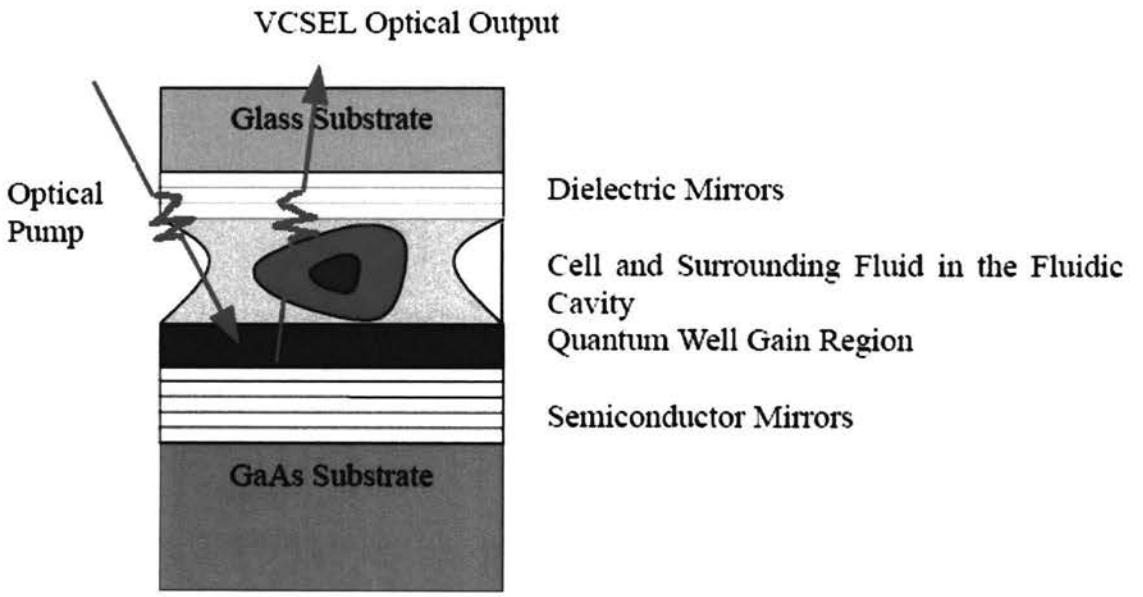

Figure 3.1 Cross-sectional schematic diagram of Dr. P. L. Gourley's biocavity laser (Reproduced from [1, 5])

3.1.2 Physics of biocavity laser

The physics of a biocavity laser is not very different than any other laser resonator. In fact, the basic principle of a laser operation remains the same for all lasers. It is the integrated microfluidic cavity of the biocavity laser that differentiates it from other lasers.

When a liquid flows though the laser microcavity, optical resonance occurs when the roundtrip light path through the entire cavity including the fluid is an integral multiple of light wavelengths. These resonance conditions appear as sharp peaks in the emission spectrum of the laser and correspond to the longitudinal modes of the laser cavity. The spacing between the modes depends strongly upon the optical cavity length of the resonator, which is further dependent upon the refractive index and thickness of the fluid media inside the laser cavity. Thus, when a cell comprising a bimolecular concentration with refractive index greater than the fluid is placed in the laser cavity, the resonance peaks are shifted to longer wavelengths and can be precisely measured by a spectrometer. By knowing the specific refractive index increment inside the fluid cavity, or the relative change in the optical cavity length, the average bimolecular concentration can be directly inferred from the spectral shift of the peaks. Since many molecules are present, and each contributes to the refractive index, the measurement represents an average bimolecular concentration within the cell.

Apart from the spectral shifts in the longitudinal modes, a biological cell also induces modulation of the transverse modes of the laser. The transverse modes of a laser are stationary solutions of the wave equation for light propagation transverse to the laser cavity. These modes are reinforced when a cell is placed inside the laser cavity, because of the higher refractive index of the cells with respect to the surrounding medium. The spacing of these modes is strongly dependent upon the cell shape, size, and its biological composition. Thus, in a biocavity laser, a cell becomes an intrinsic component of the laser and renders information about itself by guiding the light waves to a coherent state

and furnishing a unique transverse mode pattern on the wavelength spectrum of the laser. The next few paragraphs discuss the results reported by Dr.Gourley for biocavity lasers, which includes the laser wavelength spectrum for different types of biological cells in the laser cavity.

3.1.3 Experimental results

In reference [2], Dr. Gourley reports proof of concept testing of the biocavity laser by putting different sized polystyrene microspheres inside the laser cavity. It was observed that the microspheres acts like small lenses and provide lateral confinement for the light within the cavity. This further results in lowering of the threshold condition for lasing. The laser was found to operate under multimode conditions for higher input pump powers, and this was when the different spectral patterns were observed for different sized polystyrene spheres in the laser cavity.

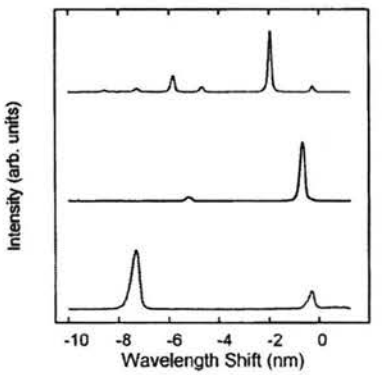

Figure 3.2 Multimode spectra obtained with femtosecond pumping for 6 μm (bottom curve), 10 μm (middle curve) and 22 μm (top curve) diameter spheres. Wavelength shift is measured from 845nm. (Reproduced from [2])

The author has also done theoretical calculations to determine the mode spacing for different sized spheres, which matches with the experimental data. Figure 3.2 shows transverse order modes of the biocavity laser for 3 different sized spheres in the laser cavity.

In Reference [3], Dr. Gourley and his co-authors suggested the use of biocavity lasers for quick and accurate detection of cancerous cells in a tissue. In this paper, the authors evaluated tumor cells using biocavity lasers, by quantifying their growth kinetics. The results showed that only a few hundred cells are required to detect abnormal or cancerous growth. This ability to detect cancer in such a minute tissue sample could be of significant value in resecting a tumor margin or grading highly localized tumor malignancy.

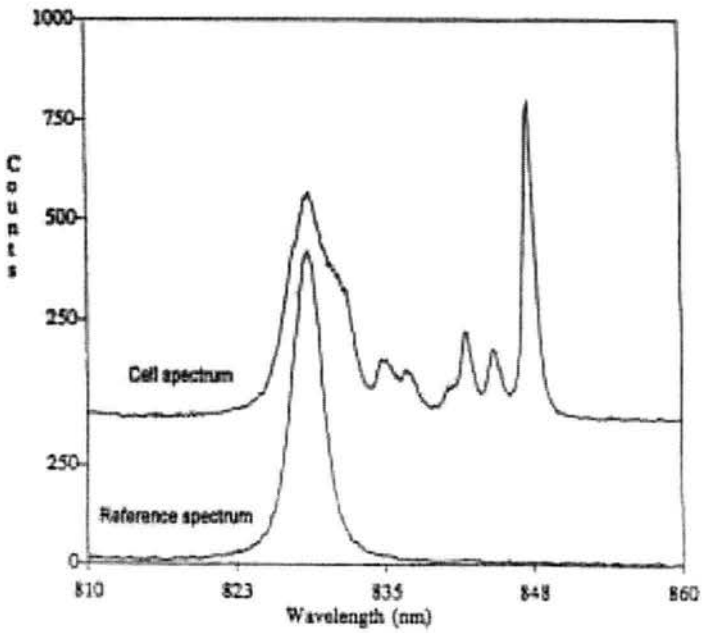

Figure 3.3 Wavelength spectrum of microcavity emission containing only blood plasma (lower trace) and red blood cell in plasma (upper trace) at room temperature. The dominant peat at 848 nm is shifted 19.3nm from the bare fluid mode at 829 nm. This shift is proportional to the concentration of hemoglobin in blood. (Reproduced from [5])

In another publication [4], Dr.Gourley has shown wavelength spectra of different types of blood cells (Figure 3.3) and compared the results with theoretical calculations on mode spacing. Various physical and optical phenomena due to a biological cell in a laser cavity are discussed, and different analytical methods are proposed to calculate the transverse order mode frequencies. In a nutshell, the biocavity lasers are presented as platforms for determining biological cell morphology, using the novel intracavity spectroscopy technique. Various lasers, including a red high power diode laser is used to optically pump the biocavity laser [8]. The biocavity laser work suffers from a major drawback in that it was not electrically pumped. This results in a system requirement of an expensive external high-power pump laser. Also in some cases, where biological agents are localized and cannot be taken to the laboratory, the biocaviy laser system suffers from the inherent disability to be carried to such places, because of its size and complexity. Thus there is a need to realize a device, which is as accurate as a biocavity laser but is less complicated, less expensive and more portable for rapid cell characterization in the field. Such a sensor should not require optical pumping but rather be electrically injected by possibly using a 9-volt (or less) battery. To realize such kind of a sensor, Tom Yu and some other members, under the guidance of Dr. Kevin Lear and Dr. Carl Wilmsen, at

Colorado State University, worked on an electrically injected version of the biocavity laser. The next two sections discuss the details of the research work done to achieve this kind of sensor device.

3.2 Work done at CSU by Tom Yu

Motivated by the research work reported by Dr.Gourley, Dr. Kevin Lear and Dr. Carl Wilmsen at Colorado State University wrote a proposal to fabricate a prototype electrically injected version of biocavity lasers. This work was started by a master's student, Tom (Tao) Yu, in 2000. This section summarizes the various accomplishments made by Tom and his fellow group members, in fabricating and testing the electrically injected vertical cavity surface emitting laser based microfluidic biosensor. The major accomplishments as reported by Tom in his thesis report [5] are as follows:

- Design of a structure for the novel electrically injected VCSEL based microfluidic cavity biosensor
- Design of a photomask for custom VCSELs
- Device fabrication-process flow
- Successful integration of microfluidic channels to VCSELs
- Demonstration of proof of concept using DI water as biofluid.

All the above points are described in detail below.

3.2.1 Device structure of novel electrically injected VCSEL based intracavity microfluidic biosensor

The device structure of a novel electrically injected VCSEL based intracavity microfluidic cavity biosensor consisted of a VCSEL diode, a microfluidic channel defined by photoresist, an external dielectric mirror and a micro-capillary tube for fluid delivery to the sensor. Figure 3.4 shows the cross sectional view of the novel biosensor. The basic structure of the biosensor is similar to that of biocavity laser reported by Dr. Gourley, except that the novel biosensor is electrically driven and it does not require optical pumping.

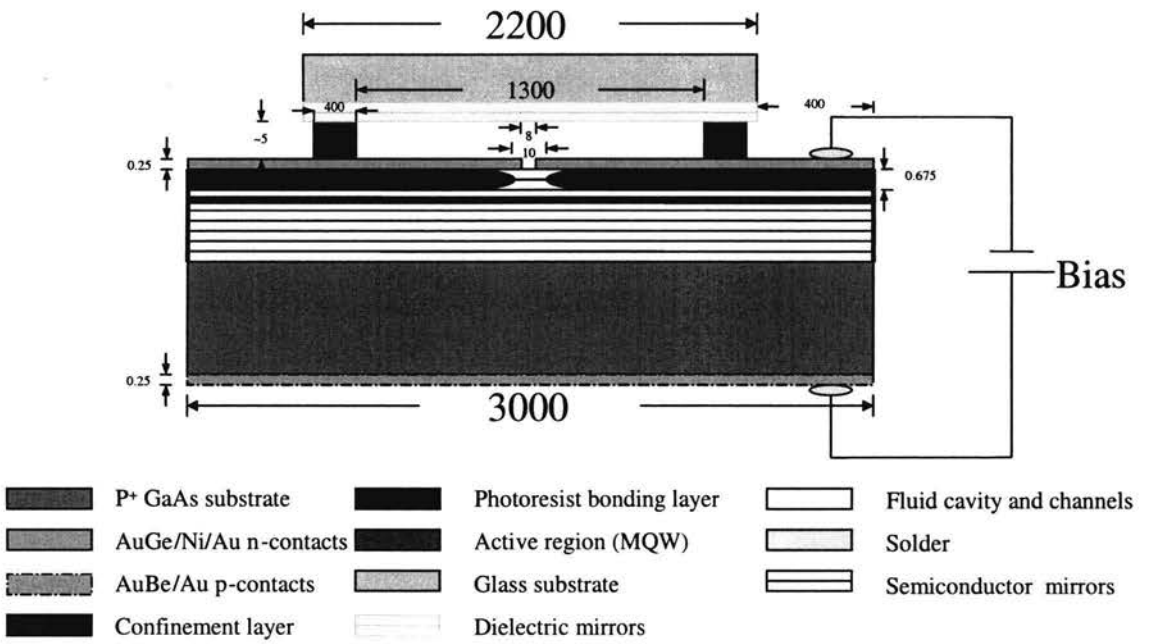

Figure 3.4 Cross-sectional view of the novel electrically pumped VCSEL based intracavity microfluidic biosensor. (All dimensions are in microns) (Reproduced from [5])

Before getting into the details of fabrication processes and testing of the novel biosensor, it is important to consider the differences between the VCSEL devices used in the two different sensors, and the effects on biosensing sensitivity.

3.2.1.1 Gourley's VCSEL vs Yu's eletrically injected "half VCSEL"

A conventional VCSEL wafer consists of a quantum well gain region with highly reflective semiconductor DBR mirrors on each side with all layers grown on a semiconductor substrate by MBE or MOVPE, as discussed in Chapter 2. The multilayer DBR not only provides reflectors to the laser resonator, but also conducts electrical current to the diode's gain region. In Gourley's biocavity laser, a half VCSEL chip is used, which does not have a monolithic DBR on one side of the gain region. As a result, electrical current cannot easily be distributed across the gain region. On the other hand, it has the advantage of having a single laser cavity formed between the external dielectric mirror and bottom DBR. The microfluidic cavity is a part of the laser cavity, and thus 100 percent of the light generated inside the gain region circulates within the microfluidic cavity in Gourley's design. This results in maximum interaction of laser light with the biofluids, and renders high sensitivity of the biosensor to fluid refractive index. Direct modulation of the resonator optical length is possible with this device, resulting in a linear relationship between the longitudinal mode shift and fluid refractive index. However the optical losses are expected to be large, since all the light generated in the laser cavity must pass through the fluid. For example, the absorption coefficient of hemoglobin, which is a major component of red blood cell, is ~ 4 cm^{-1} at 850 nm [5, 7]. Thus these devices exhibit high threshold optical pump conditions. On the other hand,

the electrically injected "half VCSEL" used by Tom Yu in the novel biosensor design, is actually more than a "half VCSEL". That is, it has a complete bottom DBR grown on a GaAs substrate, multiple quantum well gain region, and a partial top DBR, so that electrical connections can be made to the diode. Unlike other DBRs in conventional VCSELs, this partial DBR consists of only 5 pairs of $Al_xGa_{1-x}As$ alloys and is only about 60 % reflective (see Figure 3.5) at the lasing wavelength (850nm) [5,7]. In this biosensor design, the fluid cavity is defined between the top DBR and an external mirror, and thus the fluid does not become an integral part of the laser cavity. In this design, since there is reduced interaction between the light generated in the gain region and the biofluid, it incurs less optical loss and thus exhibits lower threshold conditions, thereby improving the VCSEL's performance. The disadvantage of this approach is that the wavelength does not shift linearly and rapidly as it would with change in index in Dr. Gourley's biocavity laser. These VCSEL wafers used by Tom Yu were grown at Sandia National Labs and were provided to CSU by the courtesy of Dr. Kent Geib.

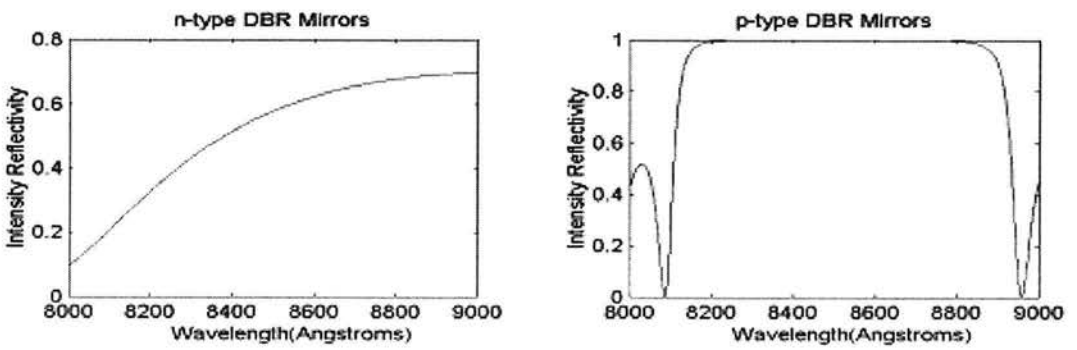

Figure 3.5 Reflectivity of the partial top (n-type) and bottom (p-type) DBR mirrors of the custom designed electrically pumped VCSEL (Reproduced from [5]).

3.2.1.2 Microfluidic channel and external mirror

Unlike Gourley's biocavity laser where there is little control over the thickness of the microfluidic cavity in the laser resonator, Tom's novel biosensor design used 5 μm thick photoresist defined microfluidic channels, to carry fluid to the laser cavity. By controlling the photoresist spinning speed, microfluidic channels of desired thickness can be defined. Photoresist, being insoluble in various aqueous solvents, can be used to define channels for different biofluids. The fabrication steps for microfluidic channel definition are described in the next section.

The external dielectric mirror used in Tom's biosensor design was a custom designed thin coating with 10 pairs of SiO_2/Si_3N_4 quarter wavelength layers deposited on a thin pyrex cover glass. The mirror was designed by Dr. Stewart A. Feld at Cielo Communications to have a high reflectivity of >99% at 850nm. Figure 3.6 shows the reflectivity plot of the external dielectric mirror.

3.2.2 Fabrication steps

The fabrication of Yu's electrically injected VCSEL based intracavity fluidic biosensor required the resolution of four important issues:

- Fabrication of half VCSELs
- Construction of uniform fluidic cavity
- Integration of capillary tube for fluid delivery
- Assembling the whole biosensor system

All the above points are discussed in detail below.

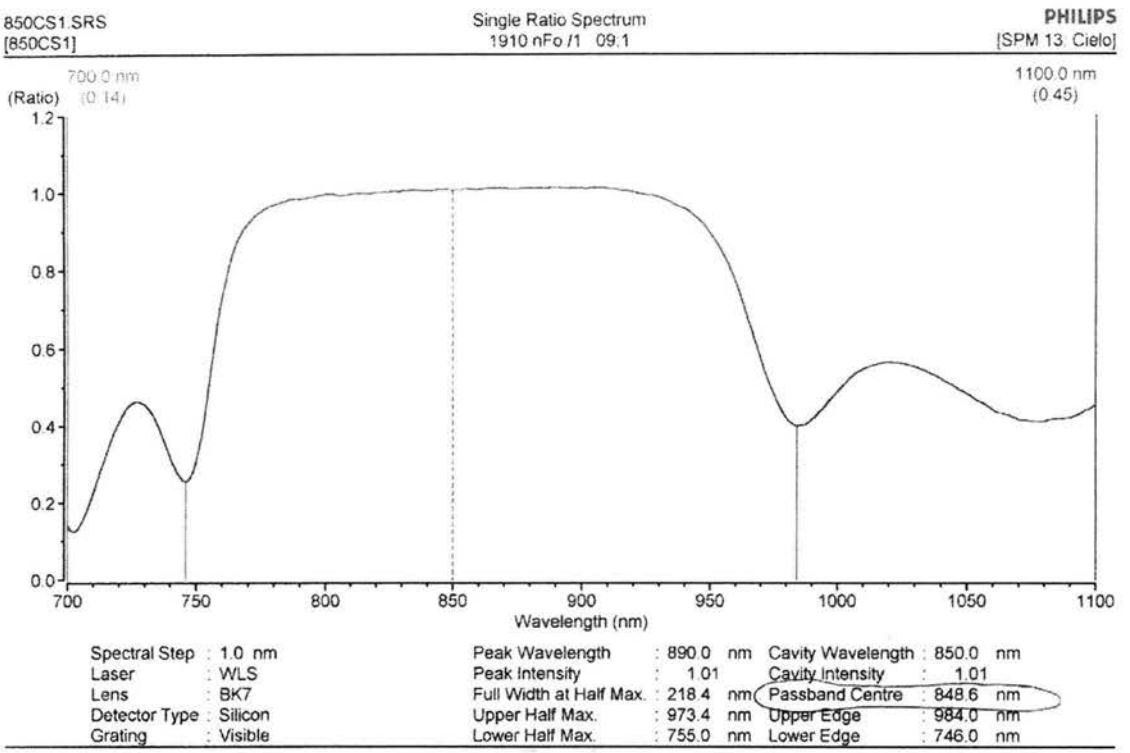

Figure 3.6 Intensity reflectivity of the external dielectric mirror fabricated at the Cielo Communications [5]

3.2.2.1 Fabrication of half VCSELs-Ion implantation

The epitaxial structure of the customized half VCSEL was already discussed earlier in this text. Although the epi material was grown at SNL, and generously donated to CSU for this research work, the devices were fabricated at the semiconductor cleanroom facility of CSU. Ion-implantation was used to achieve current confinement in these devices, and the associated photomasks were also designed for that. The main reason for the choice for this particular fabrication technique is the planarity of the devices, which is helpful in definition of microfluidic channels. Since the top DBR is very thin (~1-2μm for 5 pairs), the ion implantation dose and energy was carefully chosen, such that the

active region was not destroyed. The details about the implant can be found from Tom's thesis report [5].

3.2.2.2 Construction of uniform fluidic cavity- photoresist defined fluidic cavity and capillary integration

As already mentioned in the previous section, the fluidic channels were constructed using photoresist. There are three main reasons for choosing photoresist material for fluidic channel definition. Firstly, the process is very simple as compared to other methods such as glass etching and molding. Photoresist can be easily coated on the VCSEL chip or on dielectric mirror using a standard photoresist spinner and can be patterned to define any size and shape of fluidic channel. Secondly, a very uniform photoresist coating can be achieved by spinning it at higher speeds, and accordingly a desired thickness of the fluidic channel can be obtained. Thirdly, it is an inert material, and does not react with several aqueous solutions under normal conditions.

Dark field photomasks were designed to pattern photoresist on ion-implanted VCSEL chips. The details and dimensions of photomask features can be found in Yu's thesis report [5]. The photomask design has special features to define boundaries for a capillary tube that was integrated to the fluidic channel. With the help of these features, a micro capillary tube was placed into the biosensor system after it is sealed.

3.2.2.3 VCSEL bonding and cavity sealing

So far, the electrically injected VCSEL device was fabricated, and photoresist spacers were patterned on the VCSEL chip to define fluidic channels. Now, in order that the biosensor system should function properly, the external dielectric mirror should be assembled to the above system in such a way that a stable resonator is formed. Also, it should stick uniformly to the photoresist spacers so that a sealed cavity is constructed between the VCSEL chip and dielectric mirror. This was achieved by carefully placing the dielectric mirror on the top of photoresist spacers, patterned on the VCSEL chip, and heating the structure on a 90 deg °C hot plate. During this cycle, small magnets were placed against both sides of the assembled structure to provide magnetic bonding force while heating. The heating cycle lasts for 40 minutes, during which the photoresist softens and bonds to the dielectric mirror due to the applied pressure. Figure 3.7 shows the schematic of magnetic VCSEL bonding. After the VCSEL was bonded and fluid cavity was sealed, it was ready to accept fluids of different refractive indices and DC testing was performed on the device.

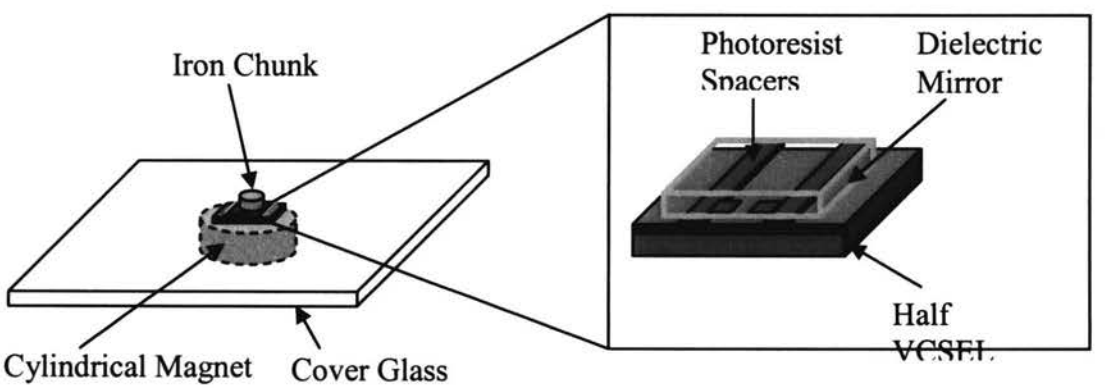

Figure 3.7 Schematic of magnetic VCSEL bonding [5]

In order to prevent shorting of the top and bottom electrical contacts of the VCSEL device, some surface passivation steps were processed on the biosensor system, the details of which can be found in Yu's thesis report [5].

3.2.3 Biosensor testing

3.2.3.1 Electrical Characteristics

The biosensor system was tested for electrical and optical characteristics under different conditions. The DC L-I-V characteristics are shown in Figure 3.8, which shows that the system acts like an LED (light emitting diode). When the VCSEL device alone was tested, it should show characteristics of an LED because the top mirror is not reflective enough to circulate enough power in the resonator to stimulate lasing action. However, when an external high reflective dielectric mirror is attached to the VCSEL diode, such as in the biosensor design, it should provide sufficient optical feedback to increase the circulating optical power, and instigate the lasing action. Tom has addressed this issue in his thesis report and he believes that something went wrong with the annealing of top metal contacts that degraded the VCSEL performance.

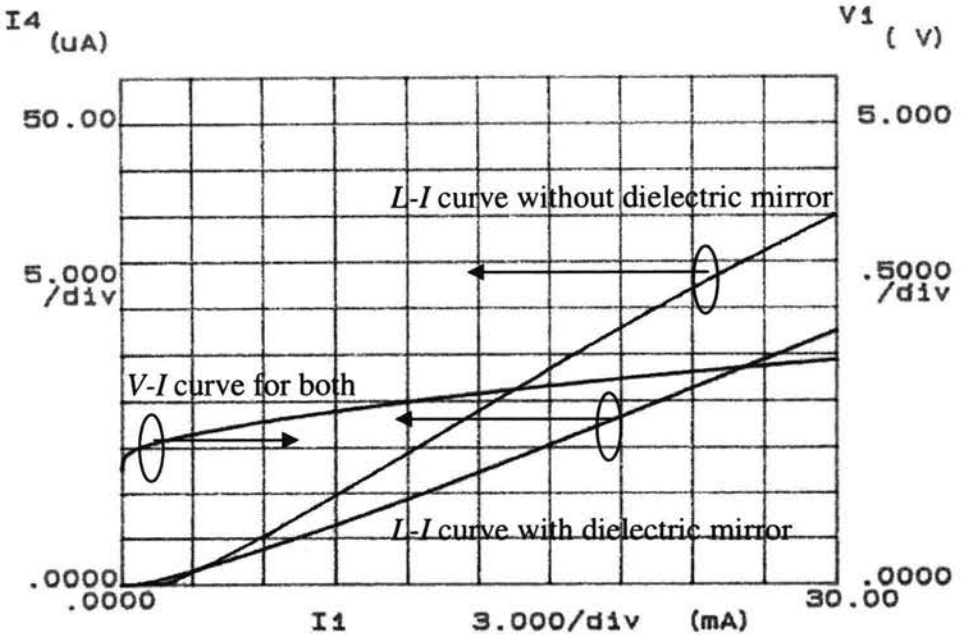

Figure 3.8 L-I-V characteristics of VCSEL diode, with and without external dielectric mirror [5]

3.2.3.2 Optical Characteristics

The wavelength spectra of the 850 nm VCSEL based microfluidic intracavity biosensor were measured for two different refractive indices of the fluidic cavity. In one case, there was no fluid inside the fluidic cavity, which corresponds to a refractive index of 1 (for air), and on the other case, deionized water was put in the fluidic cavity with a corresponding index value is 1.33. It was observed that although the device was not lasing, the fundamental mode shifted by 3.2 nm with an index change of 0.33. Figure 3.9 shows wavelength spectra of the biosensor system for the two values of refractive indices inside the fluidic cavity.

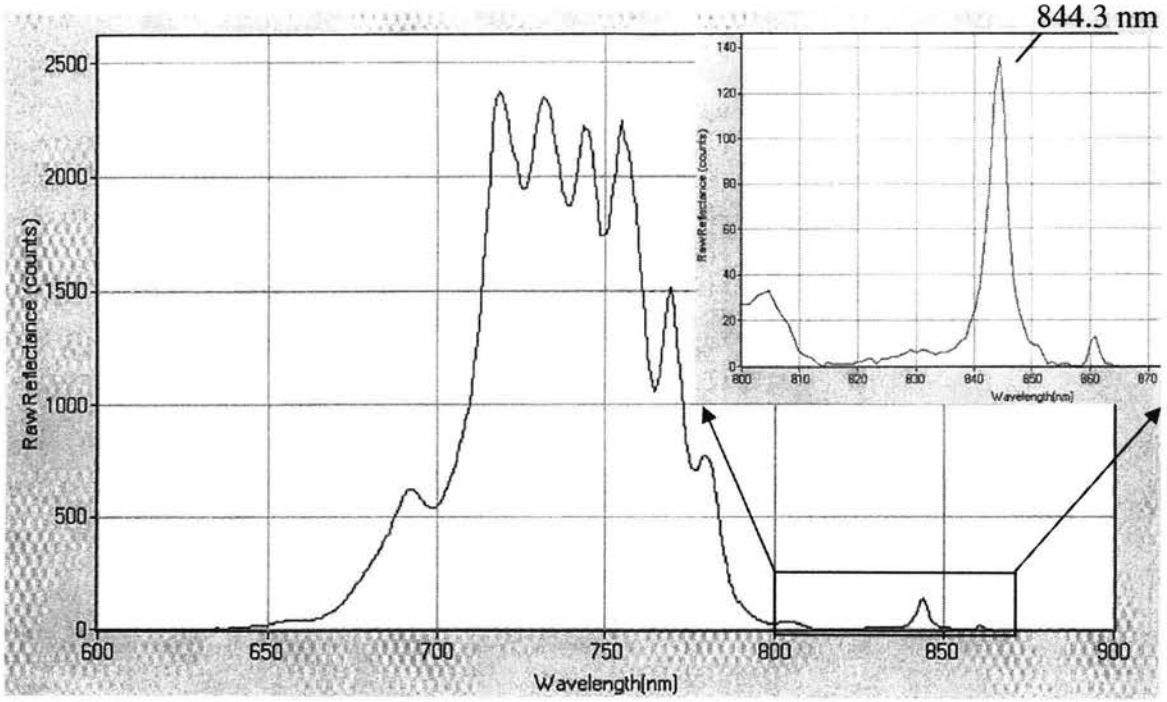

(a)

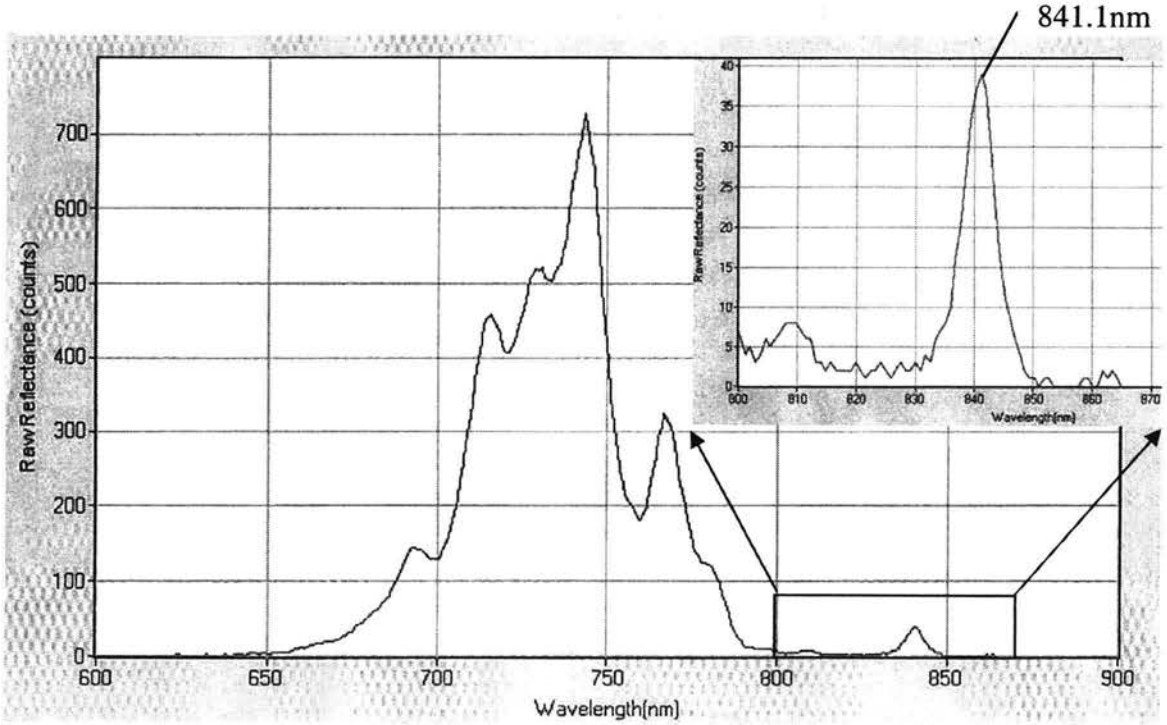

(b)

Figure 3.9 Wavelength spectra of the electrically pumped vertical cavity surface emitting laser based intracavtiy microfluidic biosensor: (a) spectrum for the empty

cavity biosensor with air (n=1) inside the fluidic cavity, (b) spectrum for the biosensor with DI water (n=1.33) inside the fluidic cavity. Wavelength shifting is 3.2 nm. [5]

3.3 Passive cavity based microfluidic biosensor

The two-biosensor systems discussed so far used active photonic devices (VCSELs), which are integral parts of the respective biosensor systems. This section discusses a similar biosensor system which does not consist of any active photonic device directly integrated to the sensor. Such a type of sensor system has several advantages over active photonic biosensor devices, and these include a simple device structure and complete electrical isolation. There are other advantages that are discussed further in this section. Research work on passive cavity based microfluidic biosensor started in Fall 2002 by a PhD candidate, Hua (Linda) Shao under the guidance of Dr. Kevin Lear at Colorado State University. This work is still in progress and the following text briefly describes the results achieved so far in the characterization of single cells. This section is divided into three parts, the first part describes the physics and operation of the passive cavity biosensor system, the second part discuss the associated challenges in fabrication of this system, and the third presents the experimental results achieved with this system. The author acknowledges the useful information provided by Linda Shao to be a part of this thesis report.

3.3.1 Physics of Fabry Perot Interferometer based microfluidic passive cavity biosensor

In this biosensor system, a Fabry Perot Interferometer is constructed between two glass pieces coated with highly reflective metal mirrors. One of the two glass pieces has etched microfluidic channels, while the other piece is plane (see Figure 3.10). Special thermo-compressive bonding techniques [6] are used to bond the two mirrors, resulting in formation of a Fabry Perot (FP) cavity in the etched region. An external high power light emitting diode illuminates the Fabry Perot interferometer and transmission spectrum of the system is analyzed by a high-resolution optical spectrometer, for different biological elements inside the FP cavity. The external light source excites the longitudinal and transverse order modes of the FP cavity, which are modulated by the different refractive index profiles and shapes of the biological cells placed in the FP cavity.

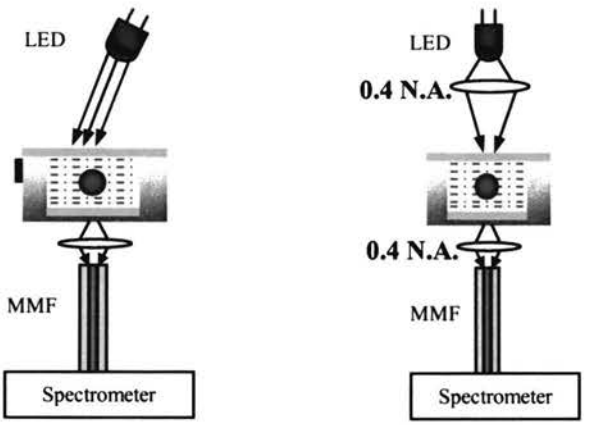

(a) (b)

Figure 3.10 Schematic diagrams of passive Fabry Perot interferometer based microfluidic cavity biosensor with (a) off axis illumination and (b) on axis illumination configurations. (Courtesy of Linda Shao)

Thus the system acts like a sensor by producing unique transmission spectra for different cells in the FP cavity. Figure 3.10 shows the schematic diagrams of the Fabry Perot interferometer based microfluidic cavity biosensor systems with two different configurations of illuminating system.

3.3.2 Fabrication of Fabry Perot Interferometer

The key steps to construct a FP interferometer are to etch microfluidic channels on a glass substrate, deposit gold on it for high reflective coating inside the channels, and then bond it with another glass superstate with coated gold, such that the high reflective gold mirrors and the etched cavity constitute the Fabry Perot Interferometer (FPI). It is important to bond the two glass pieces firmly so that the FPI is sealed and the mirrors inside the FPI are strictly parallel to each other. This is achieved in two steps, which are

- Microfluidic channel definition by glass etching
- Gold to gold thermo-compressive bonding for cavity sealing

A general wet etching technique is used to etch microfluidic channels on a pyrex glass substrate. An etching mask of chromium, gold and photoresist is used to protect the un-etched glass, as it helped in reducing the number of pinholes and improved etch profile [6]. The sequence of steps used for defining microfluidic channels is as follows:

1. Deposit 100 nm of chromium followed by 150 nm of gold on a piranha cleaned pyrex glass sample
2. Spin coat Shipley's1818 positive photoresist on the sample and pattern it with the microfluidic channels using a dark field photomask.

3. Etch gold in the region of microfluidic channels by using PR as etch mask, and aqua regia as gold etchant.
4. Etch chromium in the same region by using PR as etch mask and HCl as chromium etchant
5. Etch 10-15 nm glass in the same region by using chromium-gold-PR as etch mask and diluted HF as glass etchant.
6. Rinse photoresist by acetone
7. Deposit 100 nm of gold on the sample to result in 100 nm of gold coating inside the microfluidic channels and 250 nm in the field.

After fabrication of microfluidic channels on the substrate mirror, the superstate mirror is fabricated. The superstate is similar to the substrate, except it has no microfluidic channels, and can be fabricated by following all above the steps, except step 5. The important task is to assemble and seal the structure, which is done by gold-to-gold thermo-compressive bonding. In this technique, the substrate and superstate are held together firmly by clamps, and the assembly is heated under vacuum conditions at 350 deg C for X minutes [6]. During this process, the gold regions on the sample bond and results in a sealed Fabry Perot cavity at the regions of microfluidic channels. Various tests were done to check the parallelism of the FP structure at different points of the interferometer and it was found that this technique resulted in uniformly bonded, completely sealed and highly parallel FP mirrors [6].

3.3.3 Experimental results

As already mentioned, an external broadband LED light source illuminates the FP cavity from the top via a customized microscope system. The focusing optics used in the microscope system render the illuminated spot size from a back-lighted optical fiber to be 5 to 10 μm in diameter. This enables probing individual cells placed in the FP cavity. The transmitted light from the cells is collected by an optical fiber at the other side of the interferometer, which runs into a high-resolution spectrometer. The transmission spectra of various sizes of polystyrene spheres, red blood cells, yeast and E-coli cells have been measured and some of them are shown in Figure 3.11.

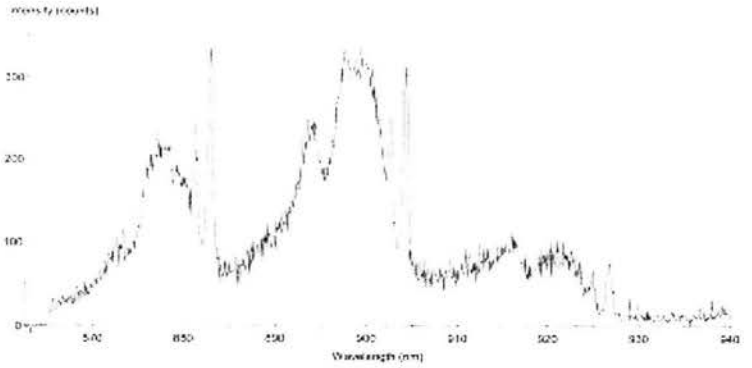

Figure 3.11 (a) Transmission spectrum of a single 5 μm diameter polystyrene sphere with uniform refractive index of 1.59 submerged in DI water under off-axis excitation.

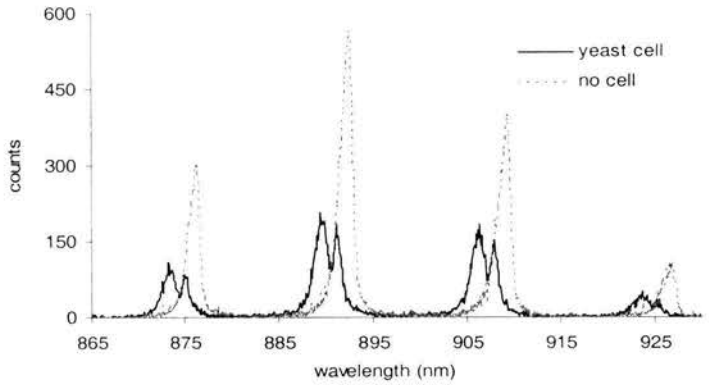

Fig. 3.11 (b) Transmission spectrum of a single yeast cell

Both off-axis and on-axis schemes are used to illuminate the FP interferometer (Figure 3.10). It is observed that in some cases, off axis illumination is better in terms of higher order mode excitation as compared to the on-axis excitation. Continuing efforts are being made to thoroughly understand the physics of different modes of excitation.

Apart from the fabrication of passive FPI based microfluidic cavity biosensor, Linda has also been involved in constructing mathematical models of spherical cells inside FP cavities and finding solutions for the transverse order modes in the wavelength spectrum. FDTD, Fullwave, bi-directional BPM and many other numerical methods have been used to solve for the transverse mode frequencies for different sized and refractive index profile micro-spheres inside the Fabry Perot cavity. Experimental results showed that they are in close agreement with the theoretical modeling.

3.4 Summary

To summarize, this chapter discusses some relevant publications of Dr. Gourley on his work on biocavity lasers. It covers a detailed description of the design structure and operation of the biosensor system reported in his papers. It also presents some of the key experimental results on wavelength spectra of different biological cells. A biocavity laser requires external optical pumping to excite lasing modes through the biological cells placed inside its fluidic cavity. The optical pumping is provided by an external laser which makes such kind of a sensor system non- portable and expensive. In order to overcome this drawback, research work on electrically pumped fluidic cavity VCSELs was initiated at the Electrical Engineering Department in CSU. This chapter also presented a detailed summary of the research work done at Colorado State University by Tom Yu and Linda Shao. It discussed the device structure and the experimental results of the novel electrically pumped VCSEL based sensor system. Linda's passive FPI based microfluidic cavity biosensor is introduced in the last part of the chapter. The special gold-to-gold thermo-compressive bonding technique is discussed, and the latest results on transverse order modes of yeast cells are presented.

References:

[1] P.L. Gourley and A. E. McDonald, "Semiconductor microlasers with intracavity microfluidics for biomedical application", *Proc. SPIE* 2978, pp.186-196 (1997).

[2] K.E. Meissner, P.L.Gourley, T.M.Brennan, B.E.Hammons, and A.E.McDonald, "Intracavity spectroscopy in vertical cavity surface emitting lasers for micro-optical mechanical systems", *Applied Physics Letters*, 69, pp 1517-1519 (1996)

[3] P. L. Gourley, *et al.*, "Detecting cancer quickly and accurately", *Proc. SPIE* 3912, pp.2-10 (2000).

[4] P. L. Gourley, "Biocavity laser for high-speed cell and tumor biology", *Journal of applied physics D*, 36 pp R228-R239 (2003)

[5] Tao (Tom) Yu, "Fabrication and characterization of electrically pumped VCSEL based interacavity fluidic biosensor" *Master's of science in electrical and computer engineering, Thesis report*, Colorado State University (2002)

[6] H. Shao, D. Kumar, S. Feld, and K. L. Lear, "Fabrication of a Fabry-Perot cavity in a microfluidic channel using thermocompressive gold bonding of glass substrates", to appear in *J. of Microelectro-mechanical Systems.*

[7] T.Yu, T.Ao, C. W. Wilmsen and K. L. Lear "Electrically pumped fluidic cavity (EPFC) VCSEL for the detection of biological agents", *Proc. SPIE 4994*, pg 206-215, San Jose, 2003

[8] Private communication between Dr. Gourley and Dr. Lear

Chapter 4

Vertical cavity surface emitting laser based fluidic cavity biosensors: device structures

INTRODUCTION

Laser based microfluidic devices, especially ones in which a microfluidic channel is an integral part of the laser cavity, such as fluidic intracavity laser diodes (FILDs), are very attractive for biomedical diagnostics applications. As already discussed in detail in Chapter 3, Gourley et al [1] have integrated a half VCSEL chip to an external mirror with etched microfluidic channels and characterized the resulting mode spectra for different normal and abnormal blood cells introduced in the external fluidic cavity. They used an external solid-state laser to optically pump the VCSEL, which increases the size and cost of such a sensor. Tom Yu, at Colorado State University, realized an electrically injected fluid cavity VCSEL that could lead to a simplified and less expensive lab-on-a-chip biosensor system. Although the design structure proposed by Tom and other members at CSU is very attractive, the group could not fabricate a functional biosensor system and thus their concept remained unproved. More details on Dr. Gourley's biocavity laser and Tom Yu's work are covered in Chapter 3 of this thesis report. The research work reported in this thesis report, not only proves the concept of electrically pumped VCSEL based fluidic cavity biosensor, but also extends it to two different biosensor structures, employing top and bottom emitting electrically pumped VCSELs. The ultimate goal is to use laser spectra to recognize different biological cells and quantify them. This thesis report presents preliminary results on modulation of laser spectra by using 10μm

diameter polystyrene spheres inside the laser cavity. This report also demonstrates dependence of laser threshold and slope efficiency on fluid refractive index. This chapter presents the novel device structures and discusses techniques for their fabrication. Experimental results on modulation of electrical and optical characteristics of biosensor systems are discussed in Chapter 5.

4.1 BOTTOM EMITTING VCSEL BASED BIOSENSOR (Device Structure I)

The basic idea behind constructing the biosensor device is to integrate a microfluidic channel within the cavity of the laser so that the bioanalyte affects most of the laser properties and thus provides a sensing mechanism. In Gourley's approach, a half VCSEL was grown on a GaAs substrate, which had a distributed Bragg reflector (DBR) followed by quantum well gain region near the surface of the wafer. This half VCSEL was then positioned just above a conventional dielectric mirror with the thin intervening region serving as a microfluidic sample area (see Figure 4.1 (a)). The VCSEL's bottom DBR and external dielectric mirror form the laser resonator; with the quantum well gain region and a fluidic sample cavity being inside the resonator.

The bottom emitting VCSEL based biosensor system (Figure 4.1 (c)) discussed here consists of a bottom emitting extended cavity VCSEL [2], photoresist defined microfluidic channels and an external dielectric mirror. To some extent, this device structure is similar to the one reported by Tom Yu [3,4] (Figure 4.1 (b)), except that a bottom emitting device is chosen in our system, instead of a top emitting one. The

extended cavity VCSEL chips were generously donated by Novalux Inc. of Sunnyvale California, and are patented as Novalux extended cavity surface emitting laser (NECSEL) diodes [2]. The details about the NECSEL structure, its characteristics, and other components of the biosensor system are discussed in the next few paragraphs. This is then followed by a complete description of biosensor fabrication and its operation.

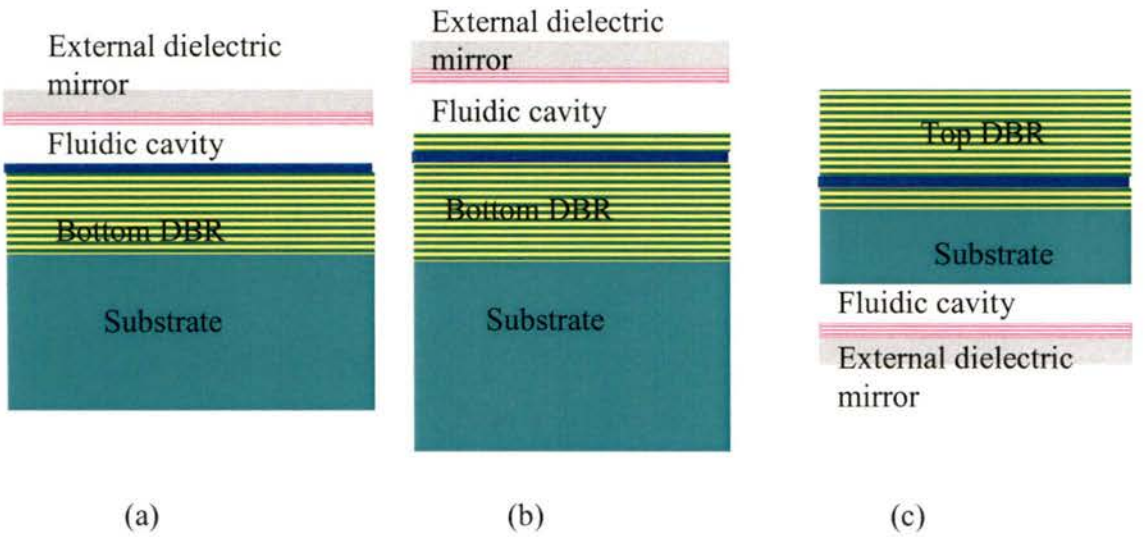

Figure 4.1 Schematic cross sectional diagrams of (a) Gourley's biocavity laser, (b) Tom Yu's electrically pumped top emitting VCSEL based sensor and (c) NECSEL based bottom emitting FILD sensor

4.1.1 NECSEL structure

NECSEL diodes are already discussed in Section 2.3 of Chapter 2 of this thesis report, in the context of external cavity VCSELS. These devices are designed for high single mode output power and intracavity frequency doubling [2,5] but are not limited to these applications. The special design features of these devices allow them to be used in

conjunction with external cavities, which are non-monolithic and constitutes the platform for special applications like intracavity spectroscopy of biological cells and fluids. Figure 4.2 shows the cross section schematic of a NECSEL diode mounted on a beryllium oxide heat sink and coupled to an external cavity with the help of an external mirror.

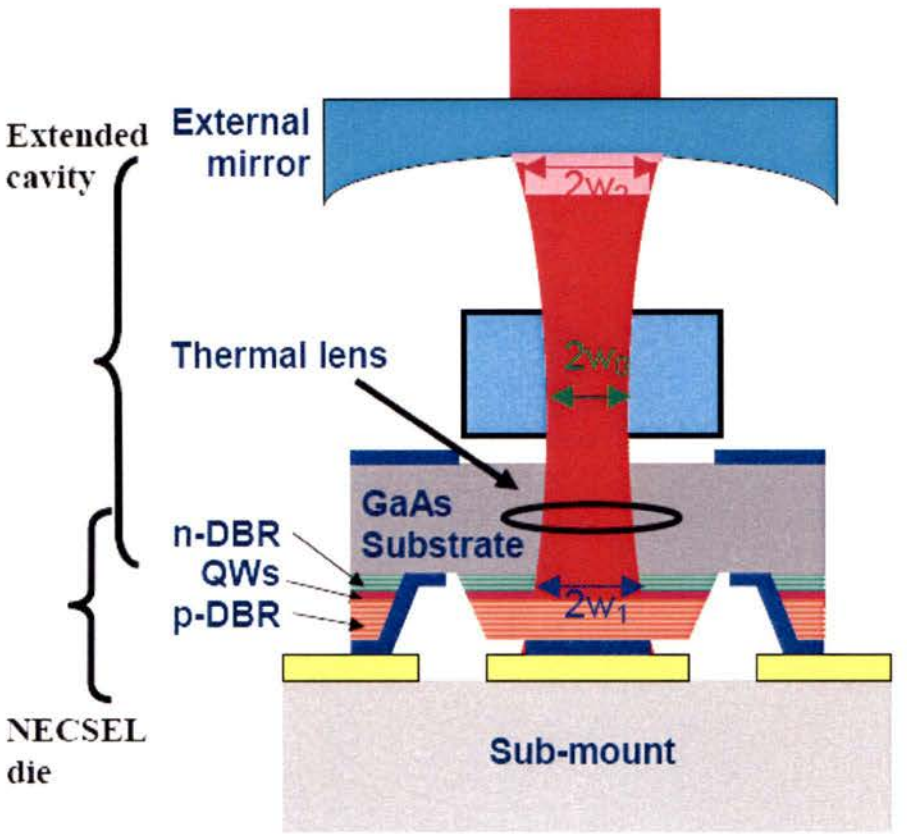

Figure 4.2 Cross sectional schematic of a NECSEL diode mounted on a beryllium oxide heat sink and coupled to an external cavity with the help of an external mirror (Reproduced from reference [2])

The NECSEL platform is designed for a 3-mirror coupled cavity resonator system, as shown in Figure 4.2. Two of the mirrors are epitaxially grown on a GaAs substrate, just

like in other conventional VCSELs. The third mirror is the non-monolithic external dielectric mirror, which extends the laser cavity to allow the biological fluid interaction with laser light. These NECSEL chips are substrate emitting with a highly reflective (~99.9%) AlGaAs p-doped (top) distributed Bragg reflector (DBR), and a partially reflective (~80%) AlGaAs n-doped (bottom) DBR [2]. The desired reflectivity of the monolithic DBRs is obtained by controlling the number of epitaxially grown DBR periods in each mirror. The SEM microphotographs (Figure 4.3) of the NECSEL device show 33 pairs of top DBR layers and 10 pairs of bottom DBR layers.

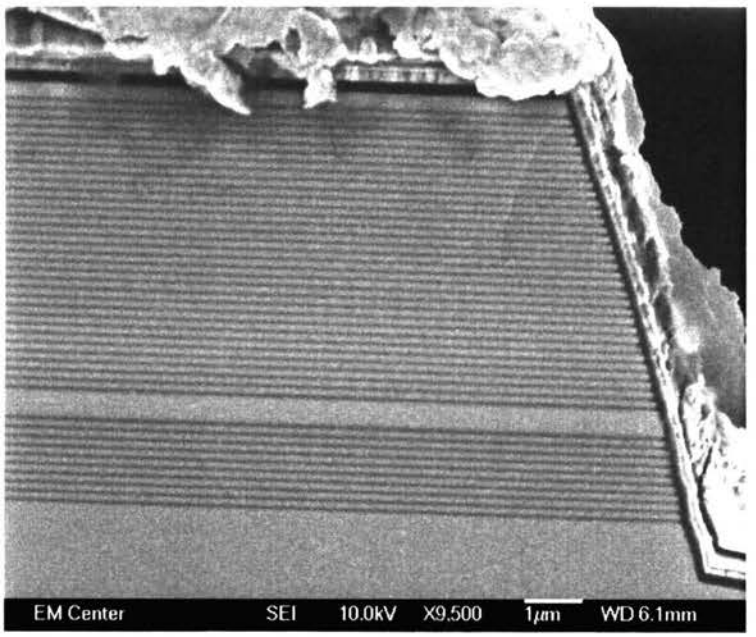

Figure 4.3 SEM microphotograph of the NECSEL chip showing 33 pairs of top DBR and 10 pairs of bottom DBR layers

The gain region of a NECSEL diode consists of clusters of strained and compensated InGaAs quantum wells, to provide a lasing wavelength of around 980nm [2]. Since these

devices are bottom emitting, and are used for extended cavity applications, their substrates are thinned, polished and AR coated after the epitaxial growth. The thickness of a NECSEL chip is approximately 80μm as opposed to standard ~600μm substrate thickness of conventional VCSELs. Thinning of NECSEL substrates reduces substrate absorption and allows higher optical power to circulate in the external cavity. This further increases the strength of optical field interaction with fluids in the extended cavity region. Ion-implantation is used to define 100μm diameter current apertures in these devices and a special step-coverage technique is used to define both metal contacts on the topside of the chip (See Figure 4.4). With this technique, dummy structures are etched on the epitaxial side, and are step covered to define metal contacts to the substrate. The top contacts are defined by etching mesas with a diameter slightly bigger than that of the current apertures.

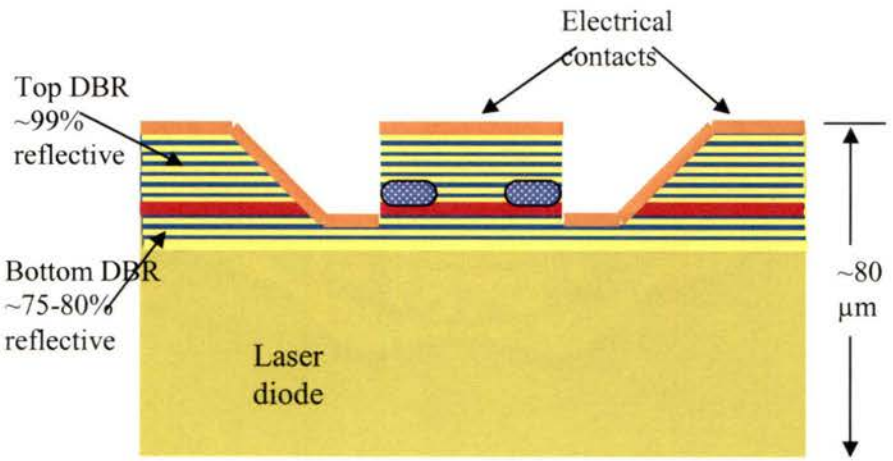

Figure 4.4 Cross-sectional schematic diagram of the NECSEL diode

A side benefit of placing both metal electrodes on the top of the laser is electrical isolation from the external cavity, since there is no direct contact of the fluid analyte with the electrodes. Owing to the special epitaxial structure, the NECSEL diodes exhibit electrical and optical characteristics that are slightly different than those of conventional VCSELs. These are shown in detail in Chapter 5, and discussed briefly in this chapter at the end of Section 4.1.

4.1.2 External dielectric mirror

The external dielectric mirror is a narrowband, high reflectivity (~99%) dielectric mirror coating on a flat polished BK7 substrate. The mirrors were custom designed at Argus International Inc., and exhibit high reflectance for a wavelength range of 950nm to 1120nm. Figure 4.5 shows a transmission plot of the mirror coatings, provided by Argus International Inc. An important feature of these mirrors is their high transmissivity in the visible wavelength spectrum, which makes them nearly transparent to a human eye or visible wavelength camera. This feature not only helps in aligning the laser chip over the microfluidic channel (as explained in Section 4.1.3) but also in analyzing the flow of fluid inside the microfluidic channels with the help of a digital camera. This is further explained in Chapter 5.

4.1.3 Microfluidic channels

The microfluidic channels are defined by using photoresist spacers, similar to the technique used by Tom in his MS thesis [3]. Photoresists are generally used as temporary masks for patterning micro or macro features on a substrate. However in the sensor

design reported here, it is used as a structural element, essentially a spin-on gasket, to define microfluidic channels and seal them against the laser chip and external dielectric mirror.

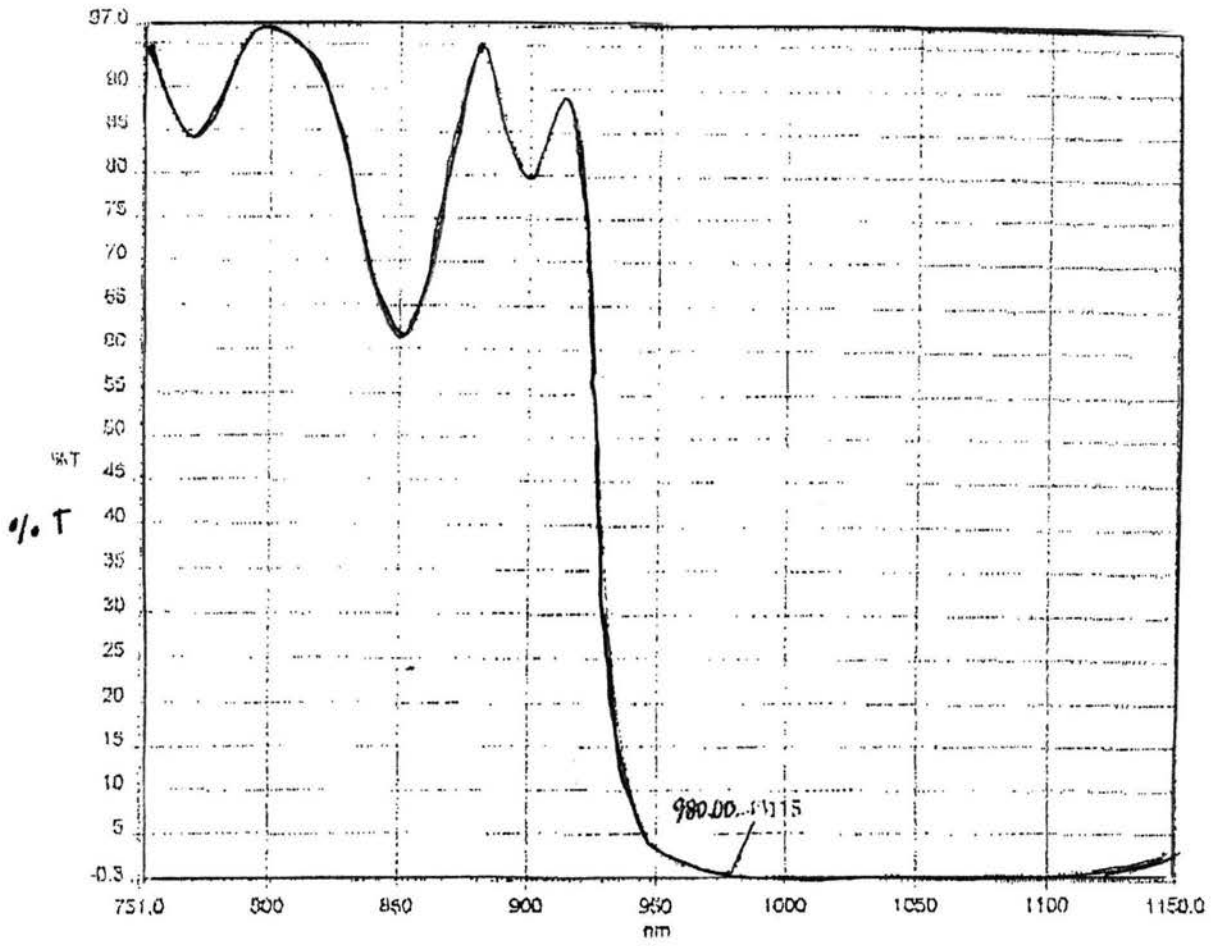

Figure 4.5 Percentage transmission plot of the dielectric mirror coating on a BK7 substrate

An important benefit of using photoresist for channel definition during experiments is that it can be easily washed away by acetone and re-patterned with or without a newer design on the same substrate. Different photomask designs were made to pattern

photoresist on the external dielectric mirror to define microfluidic channels. Figure 4.6 shows the design of a typical dark-field photomask used for patterning the photoresist channels. It consists of "straight line" features of widths ranging from 50μm to 110μm to define widths of microfluidic channels. The circular features on the mask provide areas where fluids can be dispensed into the microfluidic channels.

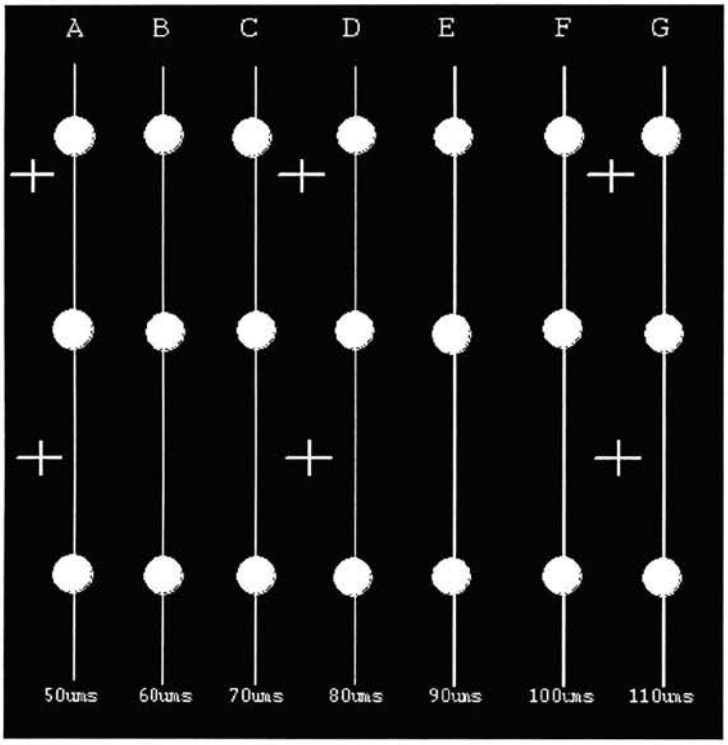

Figure 4.6 Photomask design for patterning microfluidic channels on photoresist

The photomasks are designed by using Macromedia's Freehand software and are printed on plastic transparency sheets via the CSU printing services at the old Fort Collins high school building. The photomask files are converted into eps (enhanced post script) formats and are printed on transparencies with a print resolution of 1200 dpi. The

photomask can also be designed using software like LASI and AutoCAD, and subsequently converting the drawing files into eps format. The LASI software specifically provides methods to covert drawing files into eps format.

4.1.4 Device fabrication and operation

Since the NECSEL diodes are already fabricated and provided to us by Novalux, the only processing steps required to construct the biosensor system are (i) microfluidic channel definition and (ii) device alignment and cavity sealing. These are described next.

4.1.4.1 Microfluidic channel definition

Shipley's SJR 5440 positive photoresist is used to define microfluidic channels on the external dielectric mirror. Figure 4.7 [6] shows the thickness vs. spin speed for three different photoresists, including SJR 5440, which was used to define the channel, for a spin duration of 30 seconds. Thus, a fluidic channel thickness of about 6-7 μm is obtained for a single spin at 1500 rpm.

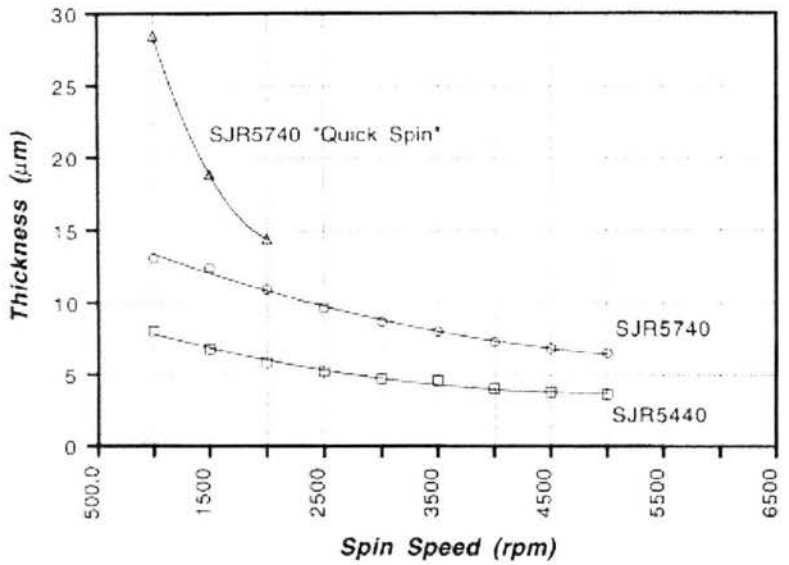

Figure 4.7 Thicknesses vs. spin speed plots of Shipley's photoresists [6]

For thicker fluidic channels, multiple spins of photoresist are done at variable speeds with intermediate post baking and edge bead removal steps. For example, to achieve a photoresist thickness of 10μm, the SJR5440 photoresist is first spun on a piece of dielectric mirror at a speed of 3000 rpm for 30 seconds, to achieve an approximate 5μm thickness. After that the sample is post baked at 120 °C for 3 minutes (as suggested by the manufacturer) to harden the resist [6]. This is followed by removal of edge beads, which is an important task to ensure a uniform layer of photoresist in the next spin. The edge beads can be removed by using a razor blade or a cotton swab with acetone. The details on edge bead removal can be found in reference [7]. After post baking, it is important to let the sample cool down to room temperature, before spinning more photoresist on it. If it is not allowed to cool down and more photoresist is poured on it for a second round of spinning, it might result in a non-uniform layer. A non-uniform photoresist layer is not desirable because it can result in a tilted resonator configuration,

which can further jeopardize the biosensor's functionality. That is why special care is required while doing multiple spins of photoresist to get thicker fluidic channels. After careful removal of edge beads and cooling of the baked resist, photoresist is spun for the second time on the sample, at the same speed of 2000 rpm for 30 seconds, to add another 5μm to the total thickness. After another step of post baking and edge bead removal, the sample is ready for patterning. The external mirrors for FILD sensors were typically spun twice, first at 3000 rpm and next at 2000 rpm, with photoresist to achieve an approximate thickness of 10 μm.

The sample is next exposed with UV radiation at 410nm using the photomask in the Karl Suss mask aligner at an exposure intensity of $10mW/cm^2$ for four minutes. The exposure time actually depends upon the thickness of the photoresist, and accordingly the developing time is also affected. Developer 453 is used to develop the exposed photoresist. For a 10μm thick photoresist exposed at the above-mentioned intensity for 4 minutes, it takes about 3 to 3.5 minutes to completely develop the pattern. It is important that the pattern is completely developed and no residual resist is left inside the fluidic channel, because, a thin layer of residual resist might increase the optical losses inside the external cavity, and result in modulation of the laser characteristics. Figure 4.8 shows a camera picture of a piece of dielectric mirror with patterned photoresist defining a microfluidic channel.

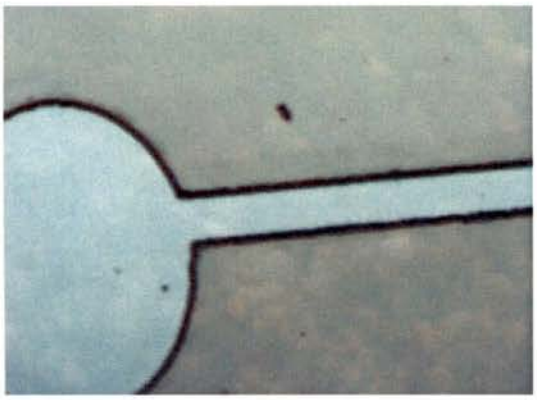

Figure 4.8 Photograph of a piece of a dielectric mirror with photoresist defined microfluidic channel

4.1.4.2 Cavity sealing and VCSEL bonding

The cavity sealing and VCSEL bonding processes are closely associated to each other in the sense that when a VCSEL chip is bonded to a fluidic channel patterned on dielectric mirror, it results in a sealed cavity between the chip and the mirror. Unlike in Gourley's biocavity laser, where the biocavity is not sealed, our structure comprises a sealed external cavity of known dimensions. The sealing of the external cavity is of significant importance in terms of the laser mode stability. Also it keeps the external cavity length constant. Thus the modulation of optical and electrical properties of the fluidic intracaviy laser diode (FILD), due to flow of a biofluid can be totally attributed to the change in refractive index.

The biosensor system is constructed by attaching the bottom emitting NECSEL diode above an external dielectric mirror with intervening photoresist spacers. Before attaching the laser diode, the external dielectric mirror is coated with an 8 to 12 um-thick layer of

positive photoresist (Shipley's AZ 5440) patterned with 100 μm wide fluidic channels and reservoirs (photomask shown in Figure 4.6). A laser diode is attached to a fluidic channel by simply placing it above patterned photoresist and heating it for 20 seconds at 125 C. At this temperature, the photoresist softens and reflows. In contrast to Tom Yu's approach of constructing a sealed fluidic cavity [3], no magnets were used to put force on laser diodes against fluidic channels. After 20 seconds, the assembly is allowed to cool down. The photoresist hardens and results in a closed fluidic cavity formed between the dielectric mirror and the NECSEL diode. This closed fluidic channel allows fluids and other biological samples through the reservoirs to the cavity of the laser. Figure 4.9 shows a photograph of a FILD sensor structure.

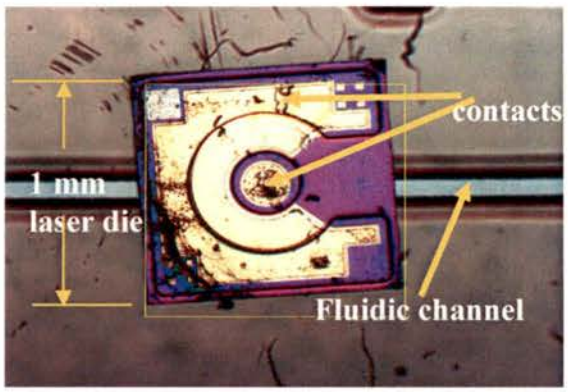

Figure 4.9 Photograph of a NECSEL based FILD sensor

4.1.5 Biosensor operation

In order to understand the physics of biosensor operation, it is important to first identify the special features of the NECSEL diode. As mentioned earlier, a NECSEL diode is specially designed to be used for extended cavity applications. The three most significant

features of a NECSEL diode, which make it appropriate for extended cavity applications are discussed below.

- Since the bottom DBR is partial and less reflective (~80%), it results in a large fraction of optical power coupled to the external cavity. Thus there is greater interaction of laser light with the bioanalyte in the external cavity.
- Both the electrical contacts of the NECSEL diode are on the topside, so that the external cavity can be constructed at the bottom (substrate) side of the diode. This provides electrical isolation to the external cavity, which is beneficial especially for biosensor applications.
- The substrate of the diode is thinned, polished and AR coated, which results in low optical absorption in the external cavity and prevents back reflection at the substrate-external cavity interface.

The operation of the biosensor system is explained as follows: The NECSEL diode is electrically pumped and lasing action occurs between the top DBR and external dielectric mirror, with the gain region, bottom DBR and fluidic channel being inside the resonator. The result is a coupled cavity resonator, where ~20-30% of the light generated inside the NECSEL diode's gain region is coupled into the external cavity. This happens because the output coupler of the NECSEL diode (bottom DBR) has a relatively low reflectivity, and thus high transmissivity. The purpose of the bottom DBR is to provide enough reflectivity to the diode so that the modal wavelength is controlled and enough optical power is generated to withstand the losses inside the external cavity. Also, it enables the system to be electrically pumped as discussed in detail in Section 2.3.1.1.

The optical power coupled to the external cavity is reflected back from the external mirror to the laser diode. When the external cavity is perturbed with a change in refractive index, it modulates the optical feedback to the laser diode from the external cavity. This results in further modulation of the system's threshold condition and output efficiency. If the system's characteristics are calibrated with respect to the change in external cavity index, it can be used to sense index values of various biofluids.

The experimental results showing modulation of threshold current density and slope efficiency of the laser diode with change in fluid index are discussed in Chapter 5. Apart from the modulation of laser's output characteristics, a wavelength shift of ~1nm was also exhibited by a FILD sensor with a change in fluid index from 1 to1.33. The wavelength spectra measurements on the FILD sensor are also presented in Chapter 5. A FILD sensor has an external cavity length of about ~85μm, and the fluidic cavity constitute a very small portion of it (~10μm). Due to long resonator length, the longitudinal modes of a FILD sensor are closely spaced and due to which mode hopping occurs when fluidic cavity perturbation. Wavelength shift due to mode hopping is not a linear phenomenon and thus leads to non-linear dependence on fluid index. This subject of short fluidic cavity with respect to total external cavity length is discussed in more detail in Sections 5.2.4.2 and 5.3.1 of Chapter 5 and also in Appendix B. A possible way to overcome this problem is to reduce the total optical cavity length, which can be done by using top emitting VCSEL diodes for the biosensor system. But at the same time, it is important that the top emitting VCSEL should also have the properties of coupling a

large amount of optical power to the external cavity, just like in a NECSEL diode. In the next section of this chapter, another structure of a biosensor system is discussed, which employs a top emitting VCSEL instead of a bottom emitting one. Unfortunately the existing VCSEL diode in the new structure did not have the similar special features of coupling large optical power into external cavity. However, the top emitting VCSEL biosensor system was still constructed as a proof of concept and tested for fluids inside the fluidic cavity. This was done with the intention of understanding various challenges associated with fabrication processes, and requirements for testing electrical and optical characteristics. Thus, if some top emitting VCSELs with the above-mentioned special properties are fabricated in future, the processing techniques described next can be applied.

4.2 TOP EMITTING VCSEL BASED BIOSENSOR (Device structure II)

The physics of the top emitting VCSEL sensor system is the same as that of the bottom emitting VCSEL based biosensor system. The only difference in this system is that the top mirror couples light to the external cavity, instead of the bottom one. The main advantage of using this kind of a sensor system over the previous one is the reduced total cavity length with same length of the fluid cavity. Thus the fluidic cavity constitutes a greater portion of the total cavity length and a greater mode shift will be registered in the wavelength spectra due to change in refractive index. Figure 4.10 compares cross-sectional schematic diagrams of the bottom emitting and the top emitting VCSEL based sensors. It can be seen in the figure that the fluidic cavity constitute most of the external cavity in top emitting VCSEL sensor design, as compared to that in the bottom emitting

VCSEL design. In the following paragraphs, the key components of the top emitting VCSEL based fluidic cavity biosensor system are discussed, which include the top emitting 850 nm Emcore VCSEL array, a gold coated mirror, and microfluidic channels on glass. The fabrication processes and the system operation are discussed in the subsequent paragraphs. Section 5.3.1 and Appendix B discusses the relative amount of wavelength shifts in the top emitting and bottom emitting VCSEL based sensors.

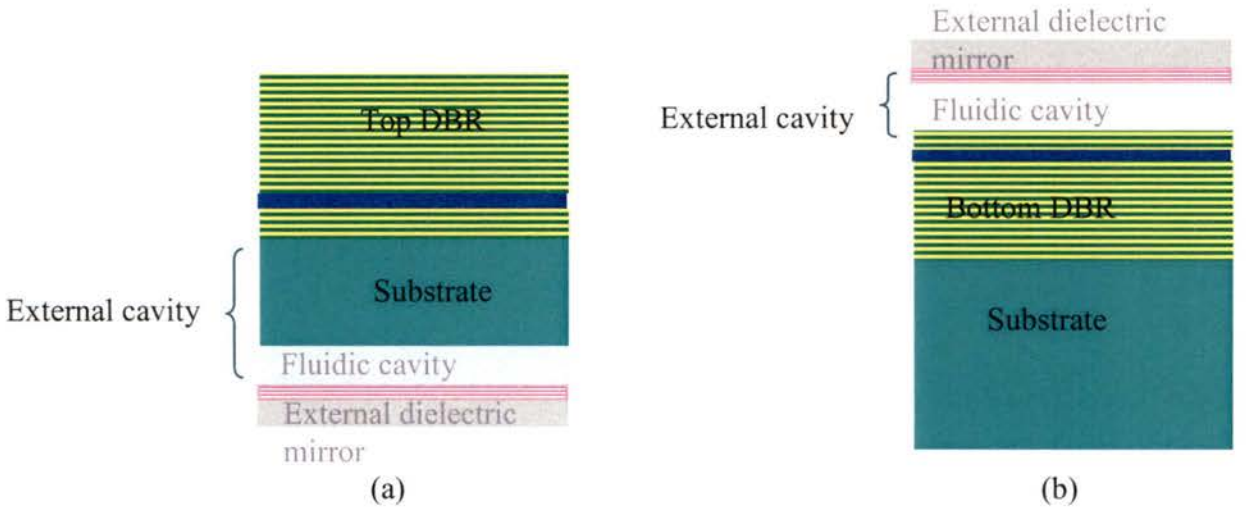

Figure 4.10 Cross-sectional schematic of (a) bottom emitting VCSEL based sensor and (b) top emitting VCSEL based sensor

4.2.1 EMCORE VCSEL array

The top emitting VCSEL used in this biosensor system comes in arrays of 12 laser diodes, which are provided to our research group by Emcore Corporation. An array contains twelve identical top emitting 850 nm VCSEL diodes, with ~10-12 μm diameter ion-implanted current apertures. Current is supplied to the diode through a top ring-contact and a bottom substrate contact. The top contacts are extended to 100μm diameter gold pads for individual VCSELs while the substrate contact is common for all of them.

The epitaxial structure consists of AlGaAs/GaAs p and n doped semiconductor DBRs and multiple quantum wells of GaAs grown on a n-type GaAs substrate. Figures 4.11(a) and (b) shows SEM pictures of such an array and individual VCSEL respectively.

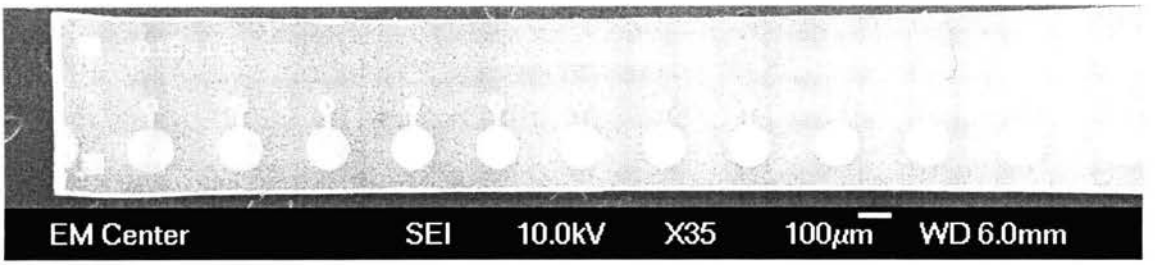

(a)

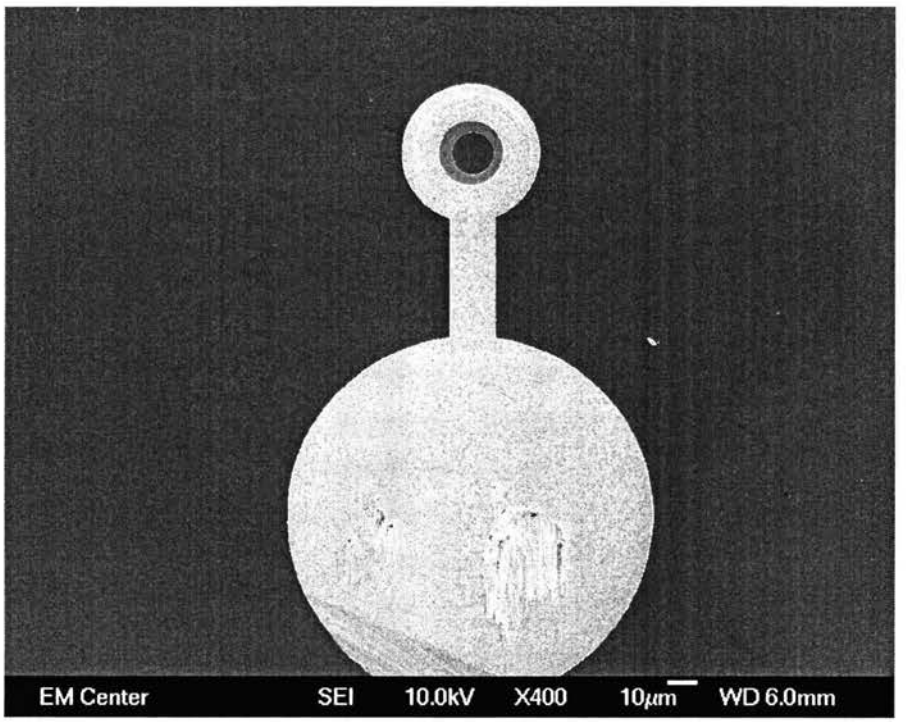

(b)

Figure 4.11 SEM pictures of (a) Emcore top emitting VCSEL array and (b) individual VCSEL

These VCSELs are full lasers and are not intended for extended cavity applications. They were used to construct the top-emitting VCSEL based biosensor system because an ideal VCSEL for such an application was not available but will have the same physical geometry as this one, and thus the fabrication steps devised in constructing this system can be reused for the ideal one. An ideal top emitting VCSEL for this application will have similar epitaxial structure for the bottom DBR and gain region, similarly defined bottom and top electrical contacts, but a different epitaxial structure of the top DBR. The top DBR, which is also the output coupler, needs to couple most of the optical power generated inside the gain region to the external cavity. This can be achieved by decreasing the number of mirror pairs, so that it becomes partial and less reflective. A layer of a transparent insulating material like silicon nitride can be coated over the electrodes, to provide electrical isolation to the external cavity. Lastly, only single devices instead of arrays are needed for individual systems.

4.2.2 External mirror with etched microfluidic channels

It is important to fully understand the requirements of the external mirror in this system, before its design is introduced in this section. Since there are no photoresist defined microfluidic channels in this system, there are more restrictions on the external mirror design in terms of external cavity definition and cavity sealing. All these special requirements on the external mirror design are discussed below.

1. In the top emitting VCSEL based biosensor system, the output coupler to the external cavity is the top DBR of the laser diode. Thus the topside of the VCSEL diode has to be in direct contact with the microfluidic cavity. The top (epitaxial)

side also has an electrical contact to the laser diode, which necessitates the laser diode to be flip-chip bonded to the external mirror. Thus the external mirror needs to have metal pad with extended electrical traces for the laser diode to be soldered on it.

2. In this biosensor system, photoresist is not used to define microfluidic channels. Instead, the channels are fabricated on glass substrate, by wet etching of glass. Since the laser's aperture is aligned with a microfluidic channel, the channel must have high reflective coatings inside.
3. Unlike in the FILD sensor and Yu's structure, photoresist cannot be used for microfluidic channel definition in the top emitting VCSEL based sensor system. The main reason for that is the necessity of having metal pads on the external mirror to provide solder contacts for the VCSEL. Since it is difficult to pattern gold pads on photoresist coated glass substrate, photoresist gasket would not be an appropriate choice to define micofluidic channel for this sensor system.

Considering the above three requirements, two possible designs of an external mirror can be realized. The first design will have dielectric mirror coatings, while the other will utilize metal deposition on glass for mirror coatings. In the first design, microfluidic channels are first etched on a glass substrate. This is done by using a photoresist-Au-Cr etch mask, as discussed in Section 3.3 of Chapter 3. It is then followed by removal of field metal by using gold and chrome etchants. Then the substrate may be ion beam sputtered or subjected to PECVD or e-beam deposition for dielectric mirror coatings on it.

This is followed by another mask alignment step where metal is patterned for solder contacts. Although this design requires numerous stages of mask alignment and metal deposition, it will yield an ideal dielectric mirror for the biosensor system. However, the external mirror used in the actual system fabricated here utilized the second design, in which metal coatings were used to provide optical feedback, as well as to conduct electric current to laser device. In this design, gold metal was deposited inside the etched microfluidic channels, and chrome and gold were patterned on the field to provide pads for solder contacts. The fabrication steps are discussed in the next section.

4.2.3 Device fabrication

The main processing steps include fabrication of an external metal mirror and flip chip bonding of the VCSEL diode to the external mirror.

4.2.3.1 External mirror fabrication

The external mirror consists of gold metal coatings inside the microfluidic channels to provide optical feedback to the VCSEL diode. It also consists of patterns of deposited metals (chrome and gold) to provide solder pads and extended electrical paths for flip chip bonding. The processing steps are discussed below:

1. A pyrex glass substrate is cleaned by using piranha solution (H_2SO_4: H2O2 = 3:1)
2. 100 nm of chrome followed by 150 nm of gold is deposited on it.
3. Microfluidic channels are patterned on it using photoresist using a photomask shown in Figure 4.6.

4. Gold and chrome are etched inside the microfluidic channels by using aqua-regia and diluted HCl as gold and chrome etchants respectively.
5. Glass is etched to define microfluidic channels, by immersing the sample in 49 % HF solution. A general etching rate of 7~8 microns per minute is observed with buffered HF solution.
6. 100 nm of gold is deposited uniformly over the sample, to get 100 nm of gold inside the microfluidic channels and 250 nm on the field.

Up to this stage, the processing steps are same as those described in Section 3.3.2 of Chapter 3. Further steps are described as follows:

7. Using a different photomask, negative photoresist is patterned on the sample, such that metal coatings inside the microfluidic channels are protected by the photoresist. Although there were no special photomasks designed to pattern metal pads for solder contacts, a similar microfluidic channel photomask pattern was used to pattern photoresist, except wider channel patterns are used over narrow etched channels. This results in protection of some metal coatings outside the etched channels. MA 490 negative photoresist is used for this purpose, the processing details of which are discussed in reference [7]. Figure 4.12 shows a process flow illustration for fabrication of the external mirror.

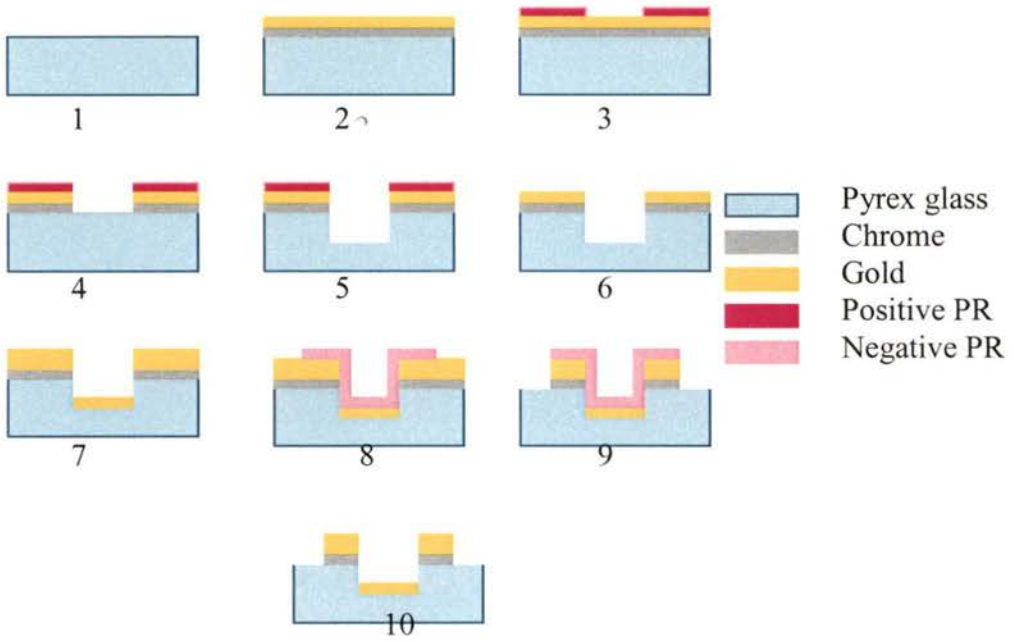

Figure 4.12 Process flow illustration for fabrication of the external mirror used for the top emitting VCSEL based microfluidic biosensor

8. By using gold and chrome etchants, the metals on the field are etched, leaving gold coatings inside the microfluidic channels and within 100 microns outside the channel. See Figure 4.12.

4.2.3.2 Flip chip bonding and VCSEL soldering

Flip chip bonding is a process of solder bonding, in which a laser chip (or any other device chip) is "flipped" or turned upside down, and soldered onto a metal pad or an electrical path by using some kind of solder metal bumps or thin coatings. In the process of flip chip bonding discussed here, indium metal is used in the form of small solder bumps. For this purpose, a wire bonder apparatus is temporarily converted into a flip chip

bonder. A wire bonder apparatus consists of a capillary tube, held by a heated collet. This capillary tube is used to carry the bonding wire used in the system. In the modified version of wire bonder, the capillary tube is replaced by a fine 10μm diameter tungsten probe tip. Figure 4.13 shows a photograph of the modified wire bonder apparatus.

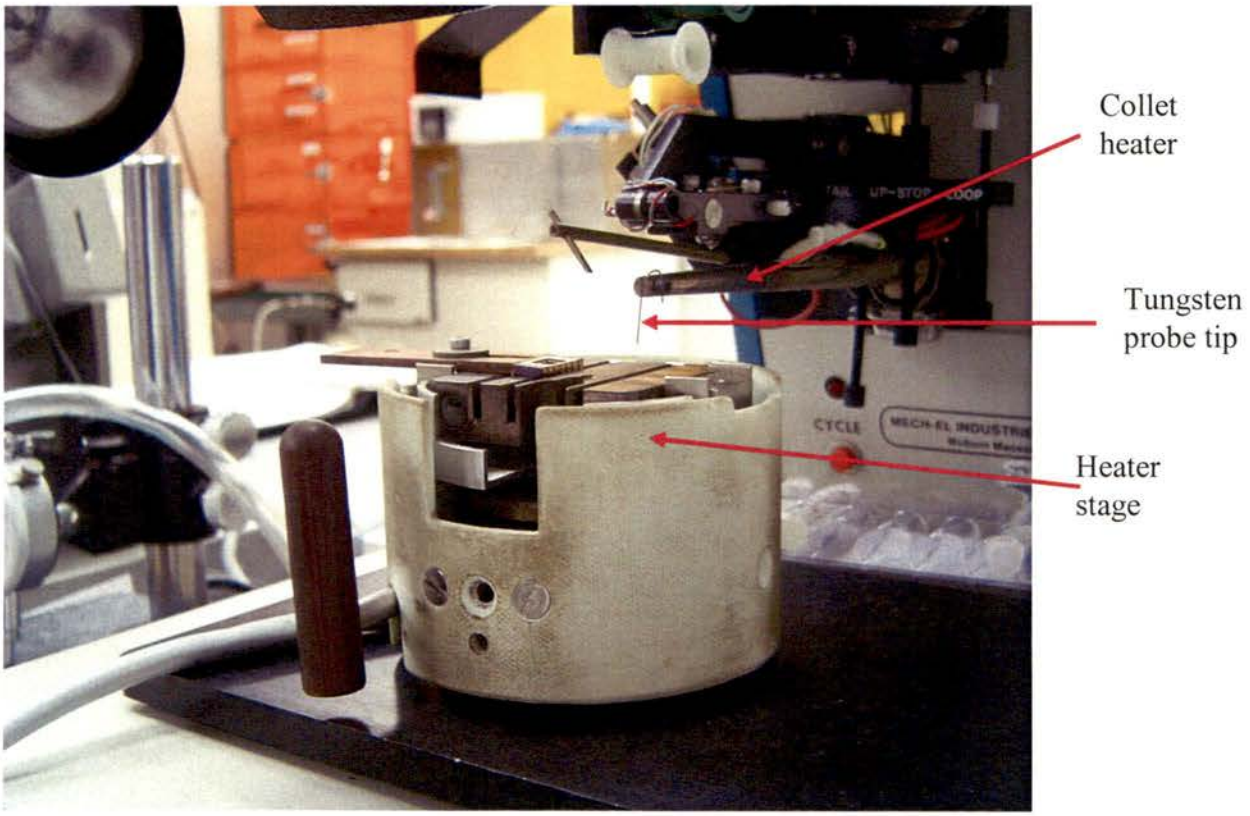

Figure 4.13 Photograph of the modified wire bonder apparatus used for flip-chip bonding

The processing steps for flip chip bonding are discussed as follows:

Indium extraction for solder metal: The first step is to extract a very small amount of indium metal for soldering 100μm diameter VCSEL metal pad on external mirror. This

is done by heating a small chunk of indium metal placed on a glass slide, on the hot plate at a temperature of 250°C. At this temperature, the indium metal is in molten state, and a tungsten probe tip is lowered to touch the molten metal. The probe tip being at room temperature solidifies the molten metal at the contact point of the 10μm diameter tip. The probe tip is raised back to its original position, and a very small quantity of the solidified indium metal sticks to it, thereby extracting a very small amount of solder metal.

Solder bump on VCSEL pad: The second step is to make a solder bump on the metal pad of the VCSEL's top contact. This is achieved by heating the VCSEL chip at 250 °C on hot plate, and lowering the probe tip such that the tiny indium bump makes contact with the metal pad of the laser chip. The indium metal on the probe tip melts and sticks to the metal pad, when brought in contact with the VCSEL chip. Thus a small quantity of solder bump is placed on the VCSEL chip.

VCSEL alignment over external mirror: The third and the most important step is to align the laser's aperture with a microfluidic channel. Apart from aperture's alignment with the microfluidic channel, it is also important to establish a solder bond between the metal coatings outside the channel and the laser's metal pad. This is achieved by first flipping the laser chip, and attaching its substrate side to the probe tip using crystal bond epoxy. This is followed by lowering of the flipped laser chip towards the external mirror. When the laser chip gets close to the external mirror, its reflection can be seen on the external mirror, and thus the chip is aligned to the mirror. The epoxy is melted and the VCSEL chip is released from the probe tip by raising the temperature of the collet heater

above the melting point of the epoxy. The VCSEL chip is pressed against the external mirror and placed on a hot plate at 250°C, so that the solder bump melts and spreads uniformly to form a uniform and thin layer solder bond. A uniform layer of solder bond is important to ensure parallelism between the external mirror and the laser's aperture. Figure 4.14 shows a camera picture of a VCSEL chip aligned over a fluidic channel and soldered to the field metal.

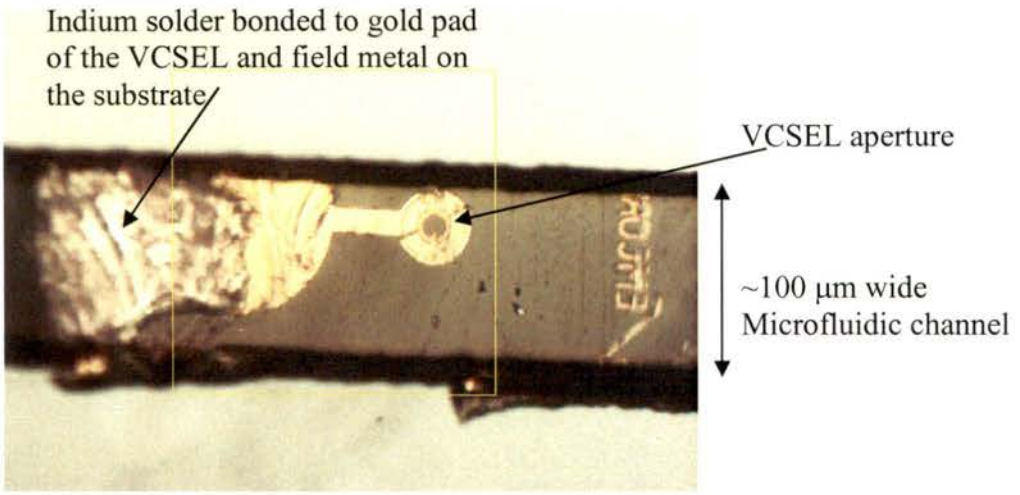

Figure 4.14 Camera picture of a top emitting VCSEL aligned over a glass etched microfluidic channel and soldered to the field metal on the glass substrate.

Support for solder bond: Since the solder area is very small as compared to that of whole VCSEL array chip, it is important to support the chip such that there is not excessive mechanical strain on the solder bond. This is achieved by gluing the rest of the area of the VCSEL array chip to the mirror by a non-conductive epoxy (like crystal bond) after the laser chip is soldered.

4.3 Summary

This chapter provides complete information on the device structure and fabrication steps of the NECSEL based microfluidic cavity biosensor system. It discusses the special microfluidic cavity sealing technique by post-baking patterned photoresist untill it reflows. In the interest of increasing the sensitivity of the biosensor system on wavelength spectrum, a new design of another VCSEL based fluidic sensor system is proposed. The sensor system consists of a top emitting VCSEL and glass etched microfluidic channels. The device structure of the new design is explained and fabrication steps are discussed.

References:

[1] P.L. Gourley and A. E. McDonald, "Semiconductor microlasers with intracavity microfluidics for biomedical application", *Proc. SPIE* 2978, pp.186-196 (1997).

[2] Eva M. Strzelecka, John G. McInerney, Aram Moorandian, Alan Lewis, Andrei V. Shchegrov, Dicky Lee, Jason P. Watson, Keith W. Kennedy, Glen P. Carey, Hailong Zhou, Wonill Ha, Brad D. Cantos, William R. Hitchens, David L. Heald, Vincent V. Doan, Kevin L. Lear, "High power, high brighness 980 nm lasers based on the extended cavity surface emitting lasers concept", *Proceedings of SPIE*, Vol. 4993

[3] Tao Yu, "Fabrication and characterization of electrically pumped VCSEL based intracavity fluidic biosensor", *Masters of Science in Electrical Engineering, Thesis*

report, Colorado State University, 2002

[4] T.Yu, T.Ao, C. W. Wilmsen and K. L. Lear "Electrically pumped fluidic cavity (EFPC) VCSEL for the detection of biological agents", *Proc. SPIE 4994,* pg 206-215, San Jose, 2003

[5] A. V. Shchegrov, D. Lee, J. P. Watson, A. Umbrasas, E. M. Strzelecka, M. K. Liebman, C. A. Amsden, A. Lewis, V. V. Doan, B. D. Moran, J. G. McInerney, A. Mooradian, "488 nm coherent emission by intracavity frequency doubling of extended cavity surface emitting lasers", *Procedings of SPIE,* Vol. 4994, page 197-205, June 2003

[6] Shipley SRJ photoresist specification sheet, http://bifano.bu.edu/tgbifano/Web/EK130/PDF/sjr5000flyer.pdf

[7] Ahmad Al Omari, "Fabrication and characterization of high-speed oxide confined vertical cavity surface emitting lasers" *Masters of Science in Electrical and Computer Engineering, Thesis report"* Colorado State University, Aug 2002

Chapter 5

Testing and characterization of NECSEL based fluidic cavity biosensor

INTRODUCTION

This chapter describes experiments that prove the concept of electrically pumped vertical cavity surface emitting laser based microfluidic biosensor by presenting the experimental data on measured characteristics of the biosensor devices. It begins with the discussion of the experimental setup used for testing and characterization of biosensor devices. It briefly addresses the testing requirements and presents the construction of the customized experimental setup for sensors testing. Next, experimental data on measured electrical and optical characteristics of the biosensor devices discussed in Chapter 4 is presented. It also includes far field beam profile measurements of a FILD sensor system with different fluidic cavity conditions.

5.1 Experimental setup

The biosensor structures discussed in Chapter 4 have some similarities, which motivates the requirement of a common experimental setup for their testing. Both the systems emit light in the vertical, downward direction and have their electrical contacts on the topside of their respective structures. In the bottom emitting VCSEL based biosensor system, the diode itself has both electrical contacts on the topside. In the top emitting VCSEL based biosensor system, the laser diode array is flipped and soldered to an external mirror with metal coatings on the mirror's top. The VCSEL's substrate contact (negative contact) faces upwards while the epitaxial contact, which faces downwards, is soldered onto the

topside of external mirror, thereby extending the laser diode's epitaxial side contact to the top surface of the external mirror. This resulted in both the electrical contacts of the laser device facing upwards. In this way, the two device structures are similar to each other in terms of direction of light emission and geometric locations of electrical contacts. Thus a common experimental setup is built for biosensor testing and characterization. Figures 5.1 (a) and (b) show the cross sectional schematic of both the sensor systems. It can be seen from these figures that they share common electrical contact geometry.

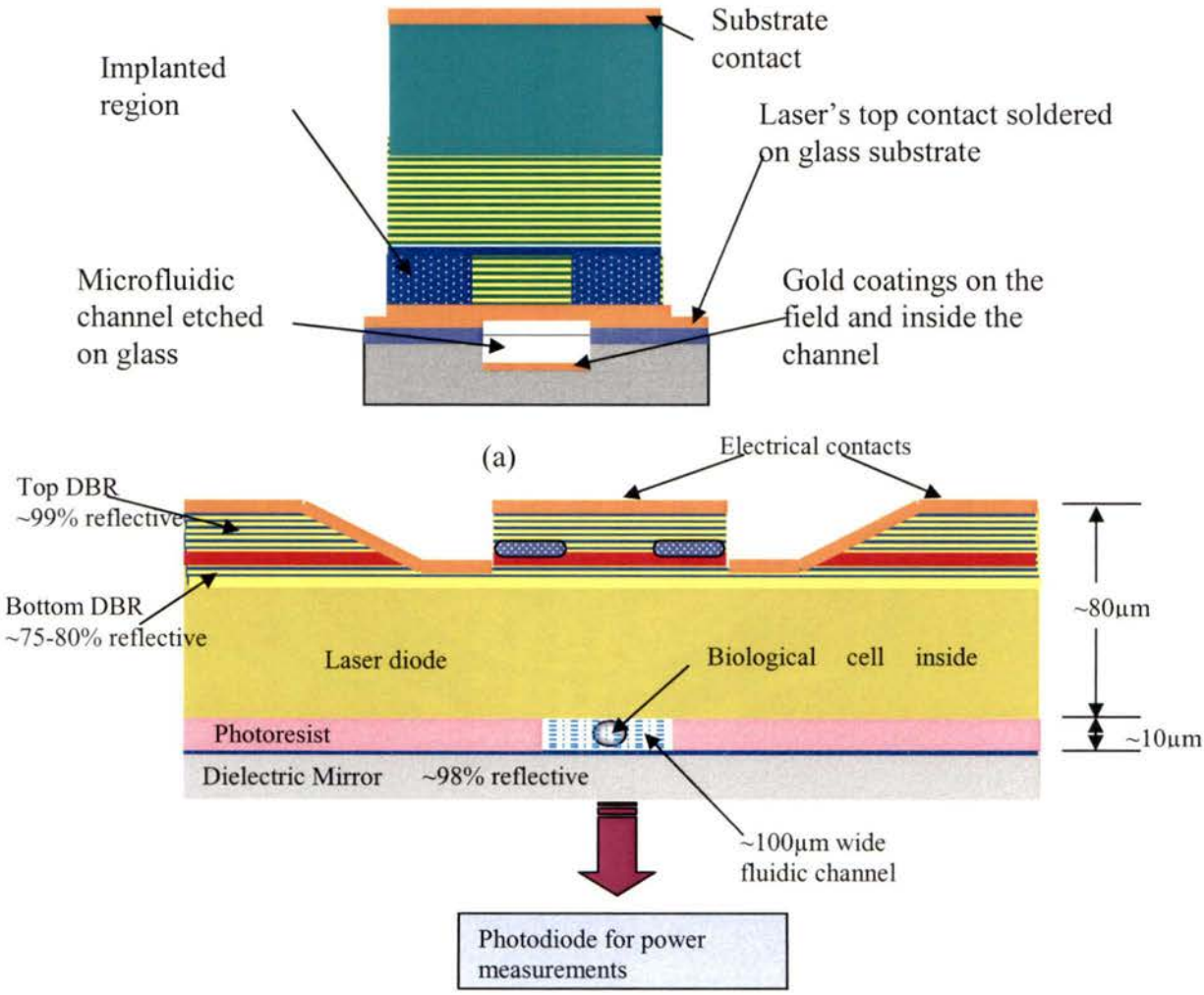

Figure 5.1 Cross sectional schematic of (a) top emitting VCSEL based sensor and (b) FILD sensor showing the electrical contact geometry of both sensor systems face vertically upwards

5.1.1 Design and construction

It is important to understand the testing requirements of the biosensor systems before the construction and associated capabilities of the experimental setup are described in this section. These requirements are discussed as follows:

1. **L-I-V testing:** Both the biosensor device structures comprise electrically pumped VCSELs, thus it is important to measure L-I-V (output light power-injection current-voltage drop across the diode) characteristics of these devices.
2. **Wavelength spectrum** of a laser device is another critical characteristic, which needs to be monitored during biosensing applications, particularly since wavelength changes provide the sensing mechanism. This requires focusing and coupling of laser light into an optical fiber, which runs into an optical spectrum analyzer.
3. **Imaging flow of fluid inside laser cavity:** There is a need to image the microfluidic flow inside the laser cavity, as it enables the experimenter to verify if a fluid or biological cell is inside the cavity.

Upon considering the above requirements, a customized experimental setup was constructed, which can facilitate all the above testing experiments. It consists of a long distance Navitar magnifying tube with a zoom lens of up to 5X magnification. The

magnifying tube is oriented vertically and is held by a post with a micrometer, which can translate the tube in the z-direction. (See Figures 5.2(a) and (b)) The magnifying tube focuses on the electrical contacts of the biosensor system, and the long working distance provides room

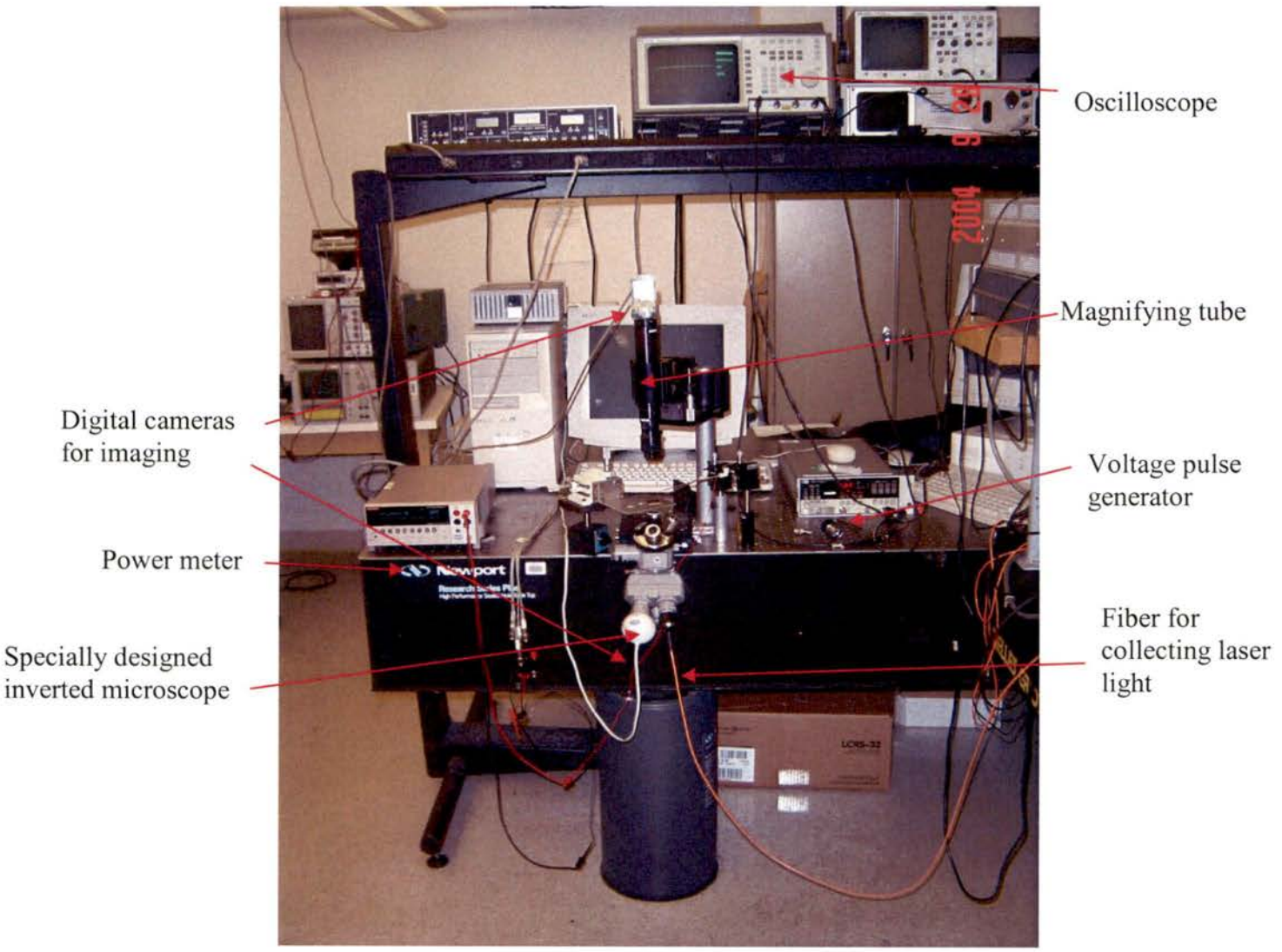

Figure 5.2(a) Photograph of the experimental setup

for probe tips to be placed on the contacts for DC or pulsed measurements. An external white light source is used to illuminate the sample, since the particular magnifying tube available doesn't support coaxial illumination. A digital web-camera is mounted on the top of the magnifying tube, which is connected to a computer to monitor probe alignment over the electrical contacts. Two probes with 10μm diameter tips are mounted on separate X-Y-Z probe tip manipulators and are connected to DC or pulsed electrical supply to provide appropriate electrical current to the devices (see Figure 5.1(b)).

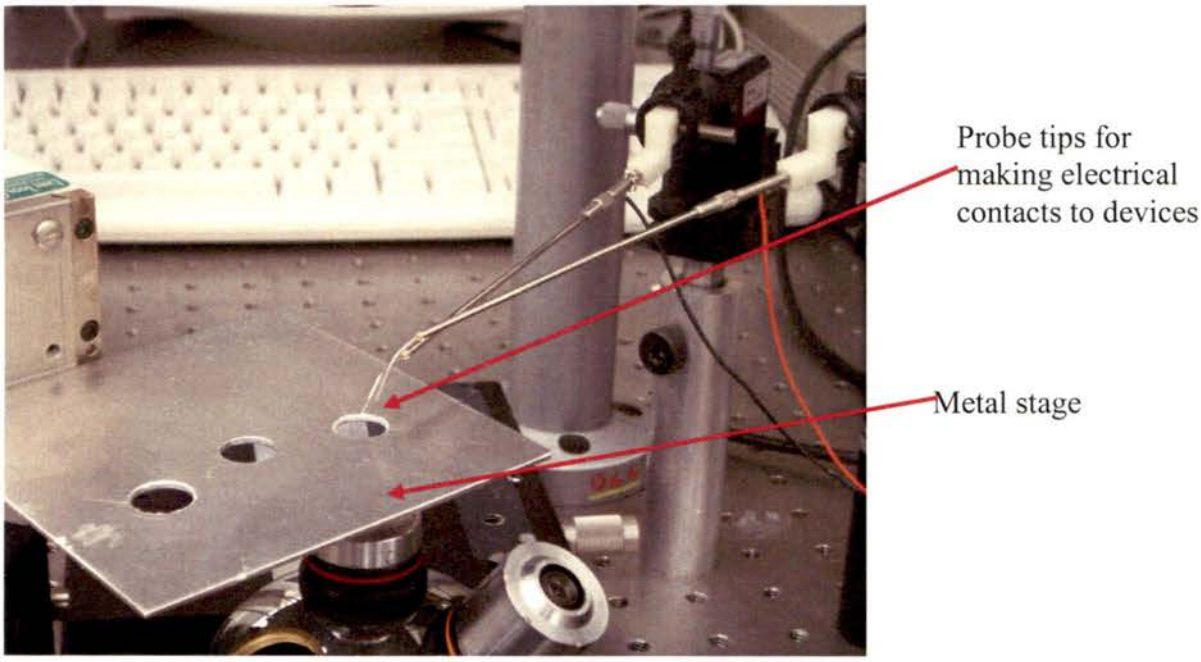

Figure 5.1 (b) Close up view of the probe tips and the metal stage

The biosensor device sits on a metal stage mounted on another X-Y-Z translator. Holes are drilled though the stage, and the laser devices are aligned over the holes so that light emitted from them passes though the holes into the optics of the inverted microscope. The inverted microscope is just like any other laboratory microscope with short working distance objective lenses, except it has an inverted geometry in the system. The

microscope is mounted on an X-Y translation stage, and its objectives lenses focus on the backside of the biosensor device. It has a coaxial illuminating white light source and a sliding prism, which switches light between a camera port and the two eyepiece ports. Since the microscope is inverted, it is difficult for a human to get access to the eyepieces and look at the backside of biosensor device. Thus another digital web-camera is mounted at one of the two eyepiece ports of the microscope, to image the backside of the biosensor device. The use of a camera also prevents unsafe direct viewing of the laser output. The other eyepiece port is mounted with a fiber adapter, and a fiber patch chord is connected at this end. A photo-detector for output power measurements is mounted in the normal camera port of the inverted microscope.

5.1.2 Functionality

The inverted microscope needs to be aligned with the magnifying tube before the setup can be used efficiently. The setup has the capability to concurrently focus on the two sides of a laser chip and collect the emitted light into an optical fiber or divert it to a photo-detector for power measurements. The system's working distance is first set up so that the top and bottom surfaces of the biosensor chip are on the focal planes of the magnifying tube and inverted microscope respectively. The next task is to align the line of sight of both the magnifying systems. This is achieved by backlighting the optical fiber optic attached to one of the eyepiece ports by an external white light source. With just a bare glass plate on the stage, a bright spot is formed on the backside of the plate. This bright spot is moved in the X-Y plane by using the X-Y translator mounted with inverted microscope, such that it appears on the preview screen of the camera attached to the

magnifying tube. At this point, the magnification of the magnifying tube is gradually increased with continuous X-Y translation of the inverted microscope so that the bright spot comes to the center of the camera view. At this stage, the lines of sight of both the magnifying systems are perfectly aligned with each other and the system is ready for testing experiments.

5.2 Experimental data on bottom emitting VCSEL (NECSEL) based biosensor systems

The bottom emitting VCSEL based microfluidic cavity biosensor system comprises an electrically pumped VCSEL diode. All the experimental data measured on the biosensor system are closely associated with the characteristics of the electrically pumped VCSEL diode. This section starts with presentation of DC measurements on the NECSEL diode. It is interesting to begin with observed effects on the device characteristics due to optical feedback from an external mirror. This is followed by pulsed measurements on the NECSEL based sensor system, i.e. the laser diode coupled to an external cavity. Next, observations of the output characteristics of the sensor system being modulated by the change in refractive index inside the fluid cavity are presented. This is further illustrated by a sequence of movie frames showing near field camera images of the fluid cavity inside the laser resonator. Finally, spectral and the beam profile measurements are presented.

5.2.1 DC measurements on NECSEL diode

While the coupled cavity resonator measurements are critical to prove the concept of electrically pumped VCSEL based biosensor system, it is of significant importance to analyze the laser diode's characteristics also. Since it is an important component of the sensor system, its L-I-V characteristics are measured under CW operation.

An HP 4145 semiconductor parameter analyzer is used to measure the continuous wave L-I-V characteristics of a NECSEL device with and without the external mirror. A silicon photodiode, PDB-C618 from Photonic Detectors Inc., with a responsivity of ~ 0.65 A/W at 980nm is used to covert the optical output power from the laser diode into photocurrent. The plots are shown in Figure 5.2. It can be seen from the above plots that lasing does not occur in the absence of external optical feedback to the laser diode. Because of the low reflectivity of the bottom DBR, not enough circulating power is developed inside the resonator to instigate stimulated emission. However, when an external mirror is used to provide optical feedback to the laser diode, it results in a decrease in mirror losses, and gain inside the resonator becomes sufficient to prompt stimulated emission at 43 mA of input current. The external mirror is a dielectric mirror, supplied by Argus International, highly reflecting at 980 nm, is placed in direct contact with the laser diode. This is an important result, as it proves that the laser diode exhibits lasing under extended cavity applications.

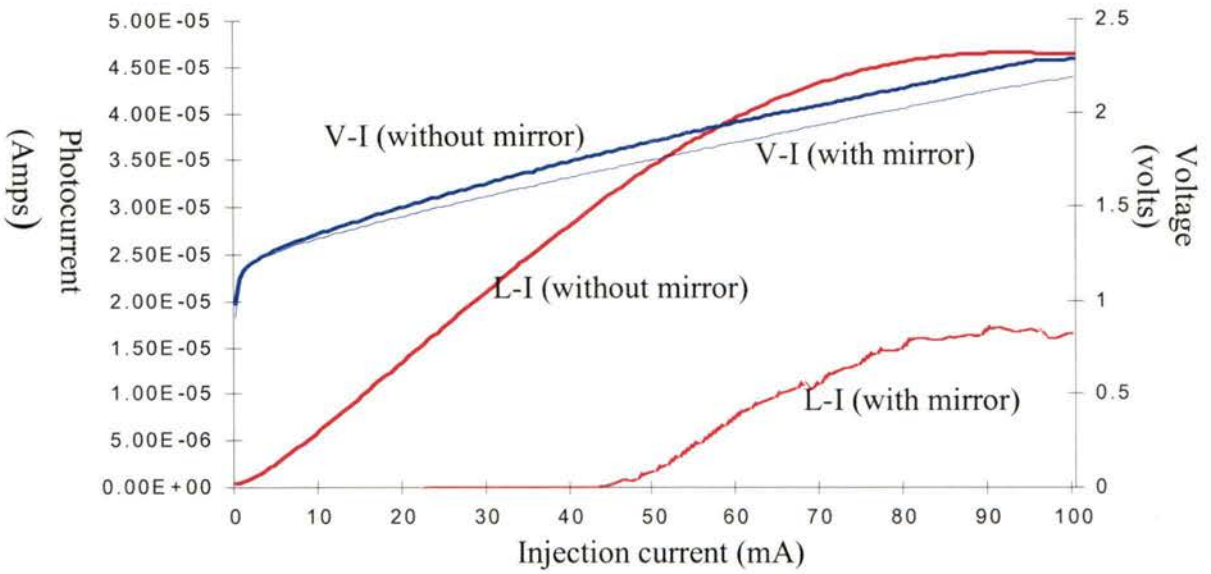

Figure 5.3 DC L-I-V characteristics of NECSEL diode with and without external mirror

As can be seen from the laser diode's LI characteristics (Figure 5.3), the optical feedback from the external dielectric mirror decreases the optical output power from the laser diode. Even though the mirror causes lasing and thus an increased circulating optical power, little of that power is transmitted through the mirror. Another important result, which can be inferred from the NECSEL's non-linear L-I plot with the external mirror, is that there is a thermal rollover at ~90mA of input current. The input power values also suggest an enormous amount of power dissipation inside the laser diode, thereby inducing thermal effects. Since it is an ion-implanted device, thermal lensing can also occur at these input power levels, which can affect the beam properties. For biosensor applications involving fluids flowing inside the laser cavity, there is a possibility of heat exchange between the laser diode and fluid inside the laser cavity. In fact, there was an

incident when boiling of water was observed inside the fluidic cavity under CW operation of the FILD sensor. In such cases, the thermal conditions are not constant for different fluids inside the laser cavity, as the fluids might have different thermal conductivity or they might flow at different rates. Thus in order that the biosensor system has similar thermal operating conditions for different fluids, the biosensor device is electrically pulsed at low duty cycles. Under these conditions, the input power level is low enough to induce negligible thermal effects. The next section discusses more on thermal effects, and presents pulsed measurements on the NECSEL based biosensor system.

5.2.2 Pulsed measurements on the FILD sensor

From Figure 5.2, it can be seen that the laser reaches threshold at a DC input power level of about 80mW. Although it is a large aperture device (100μm), an input power level of 80mW or more is still large enough to induce significant thermal effects. Moreover, the thermal effects continuously increase with input current. The main thermal effects are thermal roll over and thermal lensing.

Thermal rollover in a laser diode is a phenomenon induced by changes in gain and cavity modes of the laser diode with an increase in temperature. In small cavity lasers, like VCSELs, the longitudinal modes are spaced far apart, such that only one mode overlaps with the gain region's linewidth. Due to a large difference between the rate of longitudinal mode shift with temperature and the rate of gain spectrum's shift, the overlap between one of the longitudinal modes and gain spectrum changes with increasing

temperature. As a longitudinal mode misaligns with the gain spectrum, the output power decreases and thus thermal rollover can be explained. If the laser diode is electrically pulsed, then there is a negligible longitudinal mode shift, and thus the diode doesn't reach an early thermal rollover condition. Another heat-induced phenomenon is thermal lensing effect, which is already explained in Section 2.3.1.1.

For biosensor applications, it is critical that the thermal operating conditions are the same for different biological fluids inside the laser cavity. Thus the NECSEL based biosensor system is pulsed with short current pulses of less than 1μs at duty cycles of ~<1%. Under these conditions, the input power levels are too low to induce temperature changes. This is further discussed in the next chapter, when the thermal resistance measurements for different fluid inside the laser cavity are presented.

5.2.2.1 Pulsed L-I measurement setup

In an ideal pulsed measurement setup for laser diode based sensor systems, a current source is required with variable pulse widths and duty cycles. However, because such a system is expensive and due to ready availability of a voltage pulse generator, an experimental setup was constructed, which utilizes a voltage pulse generator and other equipment to generate known current pulses to pulse the laser diode. The block diagram of such as system is shown in Figure 5.4. It consists of an HP 8116A voltage pulse generator, an HP 5451B oscilloscope, and a Keithley 2400 source/power meter.

The voltage pulse generator generates known voltage pulses across a series circuit, which consists of a known resistance and laser diode. The oscilloscope measures the voltage drop across the known resistance to determine the current through the circuit.

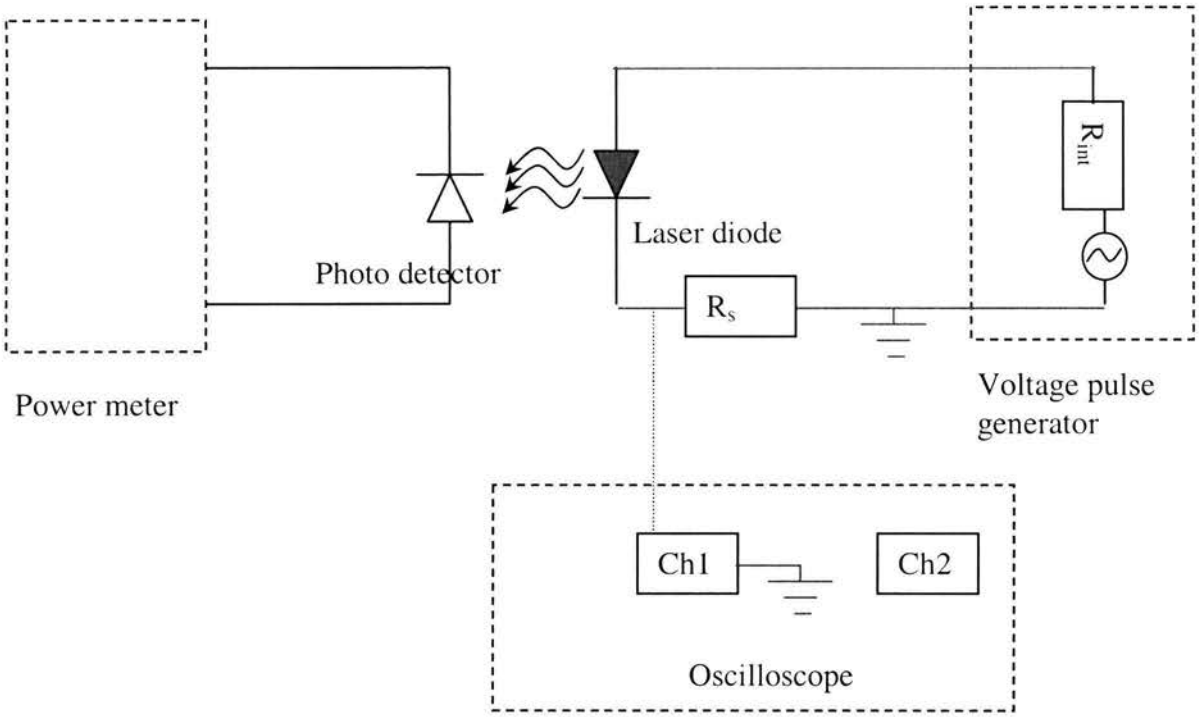

Figure 5.4 Schematic diagram of the pulsed measurement setup

The power meter measures the average photocurrent generated by a photodiode, and thus the optical power generated during a pulse can be estimated by dividing by the duty cycle. The value of the series resistance was chosen in such a way that the total resistance of the laser diode circuit matched the output impedance of the voltage pulse generator (50Ω). An impedance mismatch would induce back reflections in the circuit, which further results in ringing or oscillations in the electrical pulse. Since different laser

diodes may exhibit different forward resistances, an approximate value of series resistance of 28.5 Ω was chosen for all measurements to minimize back reflections as much as possible. A Labview program was written to control the pulsed L-I characteristic measurements. The program has the special capabilities to retrieve data from the oscilloscope, discard the oscillating part of the electrical pulse due to back reflections, and average over stable data points to determine the voltage across the current viewing resistor. The program also communicates with the power meter and voltage pulse generator to sequentially measure the average photocurrent and increase the pulse voltage signal across the series circuit, respectively. The program details and the block diagram are discussed in greater detail in Appendix A.

5.2.2.2 Pulsed L-I characteristics

Figure 5.5 shows some of the pulsed L-I measurements with different fluids inside the fluidic cavity of the biosensor system and at different duty cycles. It can be seen here that the plots are quite linear and do not saturate at high currents because the thermal effects are negligible. The trend of the measurements shows that slope efficiency and threshold current of the coupled cavity laser resonator increases and decreases respectively with an increase in refractive index of the fluid inside the fluidic cavity for three different NECSEL samples. Other trends were also observed and will be discussed in Section 5.2.6. Two different fluids, water and diffusion pump oil, along with air inside the fluidic cavity, constitute three data points for the measurements. The refractive index of air is 1, water 1.33, and that of diffusion pump oil is approximately 1.35. It is observed that when

a low index fluid is replaced by a high index one inside a laser cavity, the laser's slope efficiency increases and threshold current decreases.

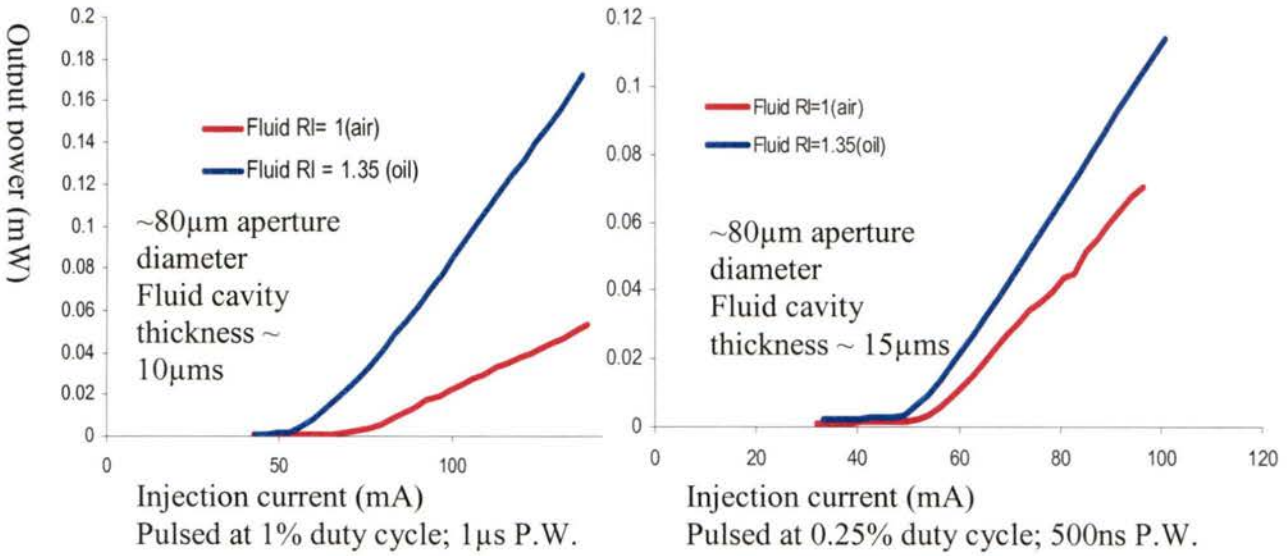

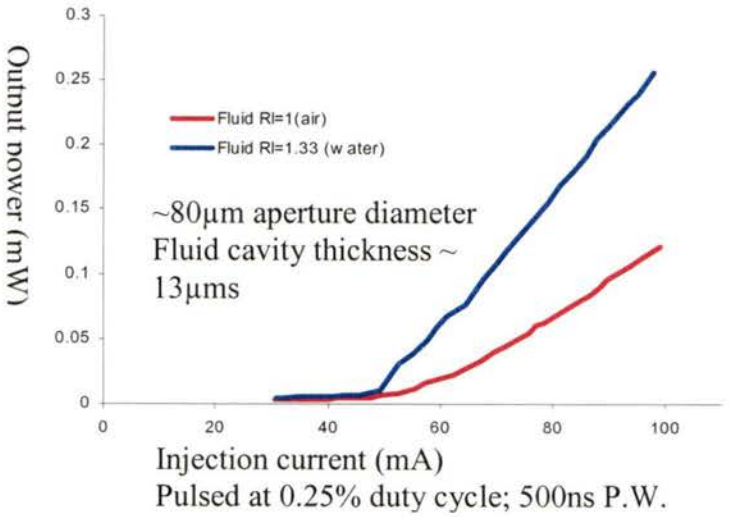

Figure 5.5 Pulsed L-I-V characteristics of NECSEL based biosensor system for different fluids inside the laser cavity and different duty cycles

The three different FILD sensor systems constructed from three different NECSEL diodes, shown in Figure 5.5 share a common trend of an increase in slope efficiency and decrease in threshold current with an increase in fluid index. However, the degree of modulation is not consistent in all the sensor systems. Other trends of experimental data exhibited by FILD sensor systems with different NECSEL diodes are presented in Section 5.2.6.

Different theoretical explanations are put forward in order to explain the different trends of the experimental results. It is desired to construct a mathematical model based on the theoretical explanations in order to determine which one best explains the experimental data. The model would either quantitatively determine the refractive index of a fluid, based on the biosensor's L-I characteristics, or estimate the laser's threshold and/or slope efficiency for a particular fluid index inside the laser cavity. The details of these phenomena are presented in the next chapter.

5.2.3 Movie frames of near field camera image of fluid cavity

As already discussed in this chapter, there are two digital CCD cameras integrated to the experimental setup to capture images of the top and bottom side of the biosensor system. Figure 5.6 shows a sequence of four frames of a movie, which was recorded by one of the two cameras. The frames show the bottom view of the biosensor device, and the camera is focused at the NECSEL's aperture through the dielectric mirror. A microfluidic channel runs across the NECSEL's aperture to carry different analyte fluids to the laser

cavity. The dark circular region in these pictures is the aperture and the bright spot on it represents laser emission.

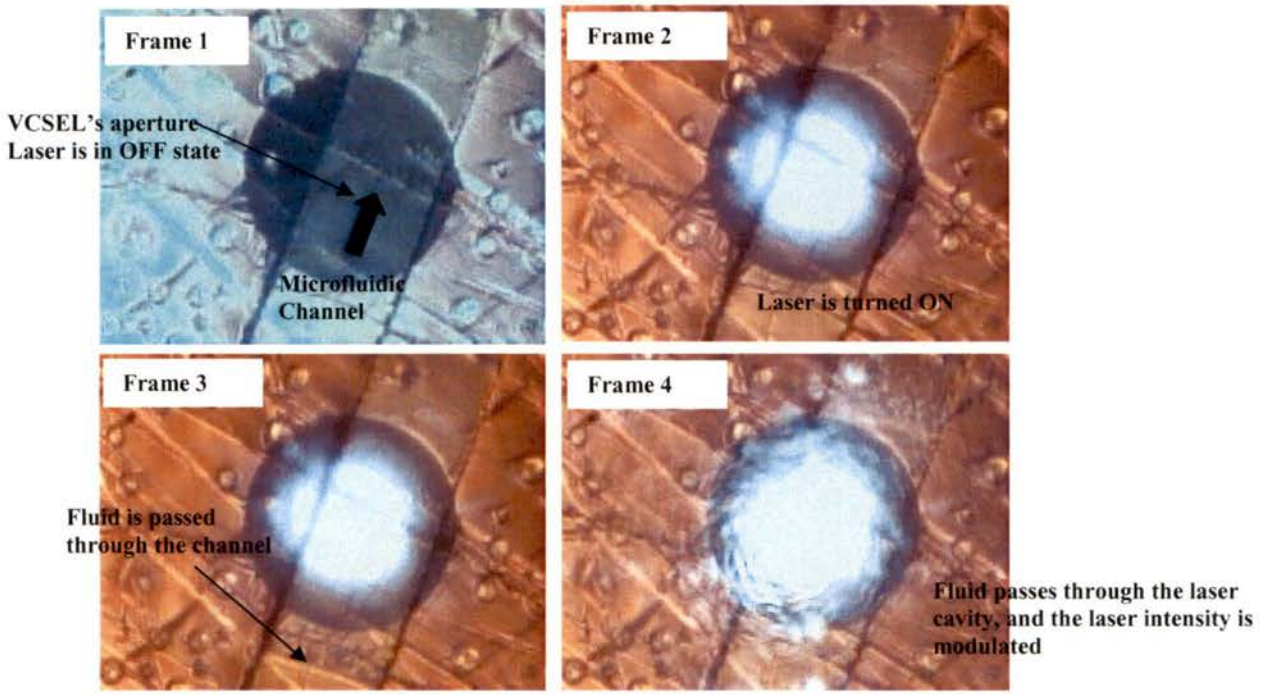

Figure 5.6 Sequence of movie frames showing modulation of laser intensity due to flow of water inside the laser cavity

The sequence of frames shows that laser is initially off (Frame 1), then it is turned on with air inside the fluidic channel (Frame 2), then a fluid with higher refractive index is inserted inside the channel (Frame 3) and lastly the fluid passes through the laser cavity and the light intensity is modulated (Frame 4). The sequence of these near field images supports the trend of experimental results as discussed in the previous section.

5.2.4 Spectral measurements

Apart from the lasing wavelength of a laser resonator, a wavelength spectrum can also provide useful information about

- Transverse confinement of a laser beam (single mode/multimode behavior)
- Thermal resistance of a laser (for semiconductor diodes)

Both the above factors are of significant importance for laser based biosensor operation, and thus need to be addressed in greater detail. While the discussion of transverse confinement does help in developing an understanding about biosensor functionality, the thermal resistance measurement results suggest that the biosensor is operated under nearly constant thermal conditions for biosensing. It is for this reason, that the discussion of the latter topic is postponed until next chapter.

5.2.4.1 Transverse confinement of laser beam

An optical field diffracts while propagating back and forth between the mirrors of an optical resonator. Due to the finite transverse dimension of resonator mirrors, the field clips at their edges and undergoes distortion of its transverse amplitude and phase profile in each round trip within the resonator cavity. It turns out that for any stable resonator configuration, employing either finite diameter planar or curved end mirrors, there is a discrete set of transverse amplitude and phase patterns for the circulating optical field in the cavity, which reproduce themselves in form, after one round trip. These self-reproducing transverse field patterns represent the characteristic set of transverse spatial

modes of that particular resonator. The transverse confinement of a laser beam is closely associated with the number of propagating higher order modes. For example, in a planar resonator, only the lowest order mode propagates, as there are large diffraction losses for higher order modes, as compared to a confocal resonator [1]. Thus depending upon the resonator structure, the propagating modes are transversely confined.

These modes not only differ in their transverse amplitude and phase profile, but may also oscillate at different frequencies inside the resonator. The higher order mode frequencies can oscillate at frequencies higher or lower than the lowest order mode frequency, again depending upon the resonator configuration. For example, Figure 5.7 shows transverse mode frequencies in near planar, confocal and near concentric resonator configurations. The details about the three resonator configurations and the physics associated with the position of higher order transverse modes relative to the lowest order mode are given in reference [1].

The transverse confinement of a laser beam is governed not only by the size and shape of end mirrors, but the intervening gain region inside a laser resonator also plays an important role in the definition of transverse modes. In fact, any physical medium that can induce a phase change and/or amplitude change of the optical field inside the resonator can modulate the transverse confinement by increasing or decreasing the number of transverse propagating modes or modulating their relative amplitudes. Thus if a self sustained laser resonator is perturbed by introduction of a microsphere or a lens like particle, which has a certain shape and refractive index profile, the transverse

confinement of the laser beam gets modulated and registered by the laser beam's wavelength spectrum and cross sectional beam profile.

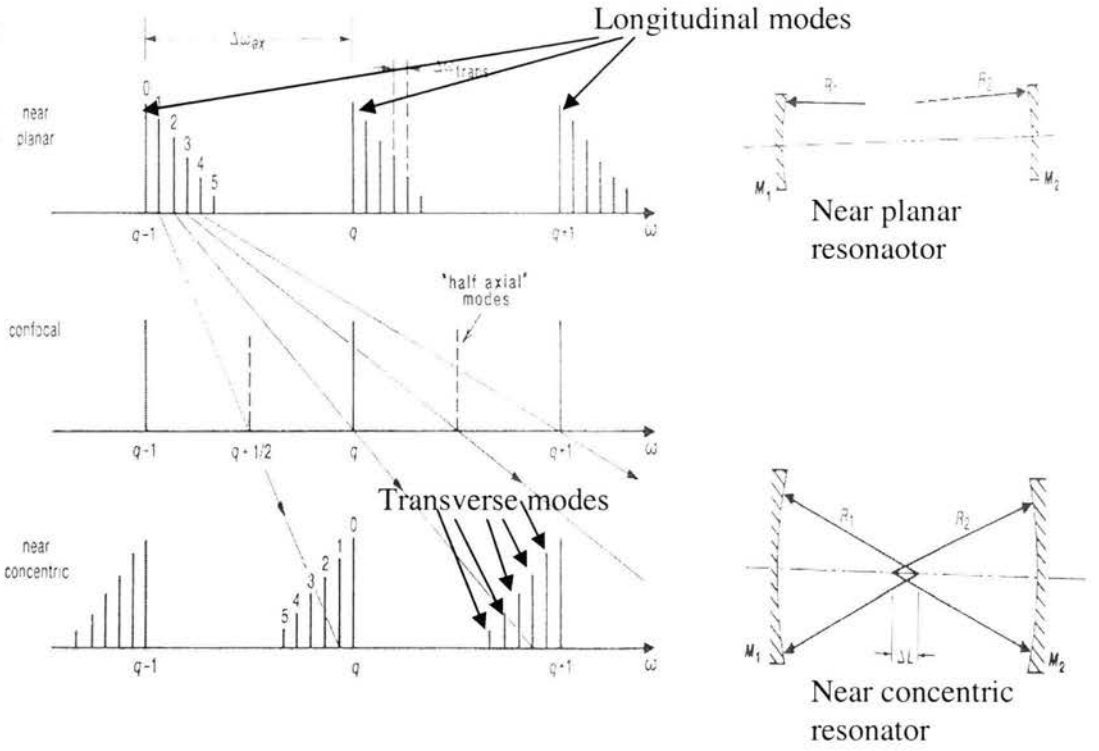

Figure 5.7 Transverse mode frequencies of a Gaussian beam in near planar, confocal and near concentric resonator configurations (Reproduced from Reference [1])

The functionality of Dr.Gourley's biocavity laser is based on transverse confinement of laser beam by different biological cells, and hence different mode patterns on the wavelength spectrum of the laser. Different biological cells have unique refractive index

and geometric profiles, which allows them to uniquely modulate the transverse confinement of the laser, and thus register a distinctive mode pattern on the wavelength spectrum of the laser. Figure 5.7 (reproduced from Figure 3.3) shows one of his several transverse mode results on cell spectroscopy.

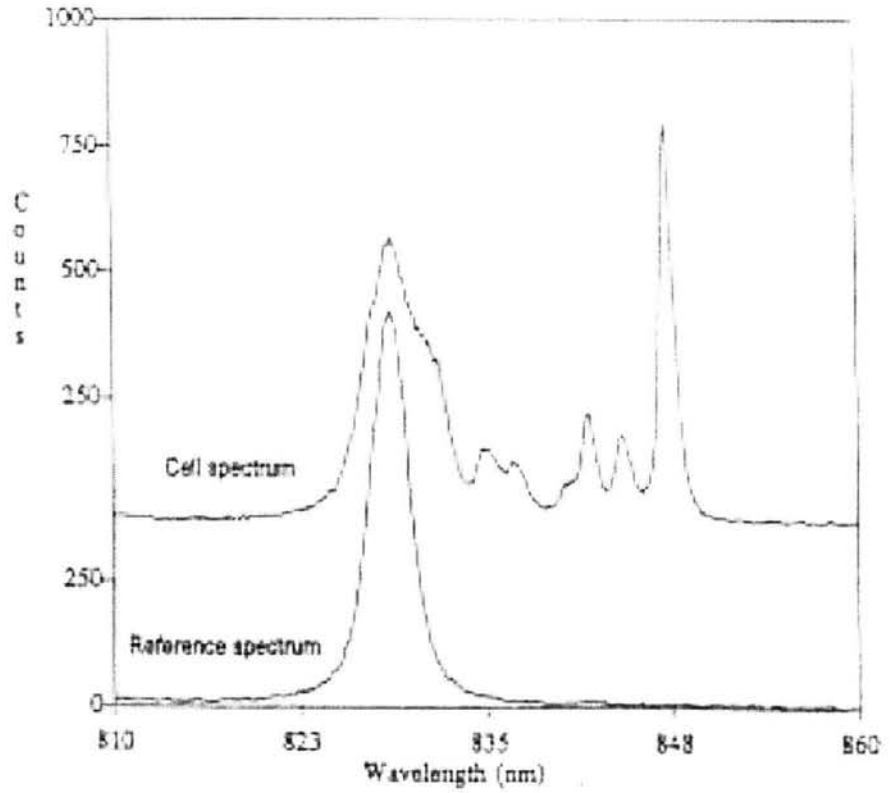

Figure 5.8 Wavelength spectrum biocavity laser with and without a blood cell inside the laser cavity (Reproduced from Reference [2])

In this work, the NECSEL based fluidic cavity biosensor is also subjected to fluidic cavity perturbation by different fluids and polystyrene microsphreres. Figure 5.8 (a) shows the modulation in wavelength spectrum due to change in bulk refractive index

from 1 to 1.33 (air to water), and Figure 5.8 (b), due to introduction of a 10μm polystyrene microsphere in the laser cavity.

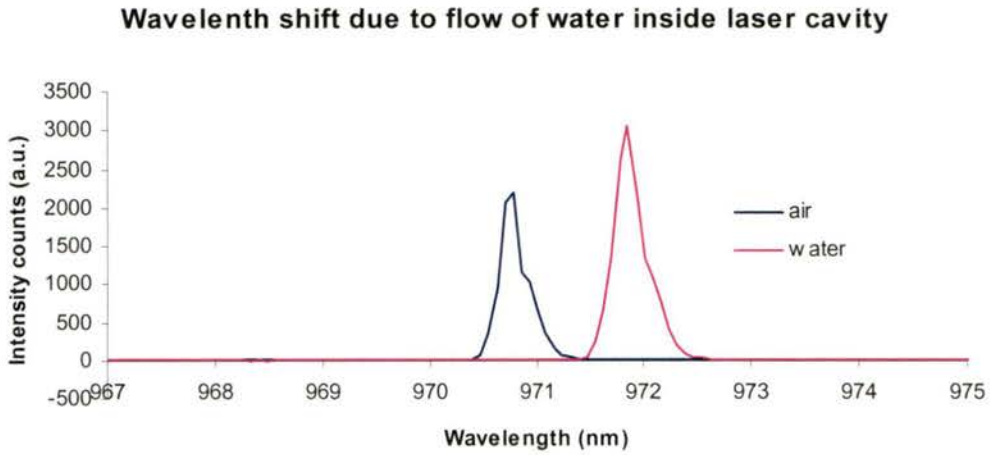

(a)

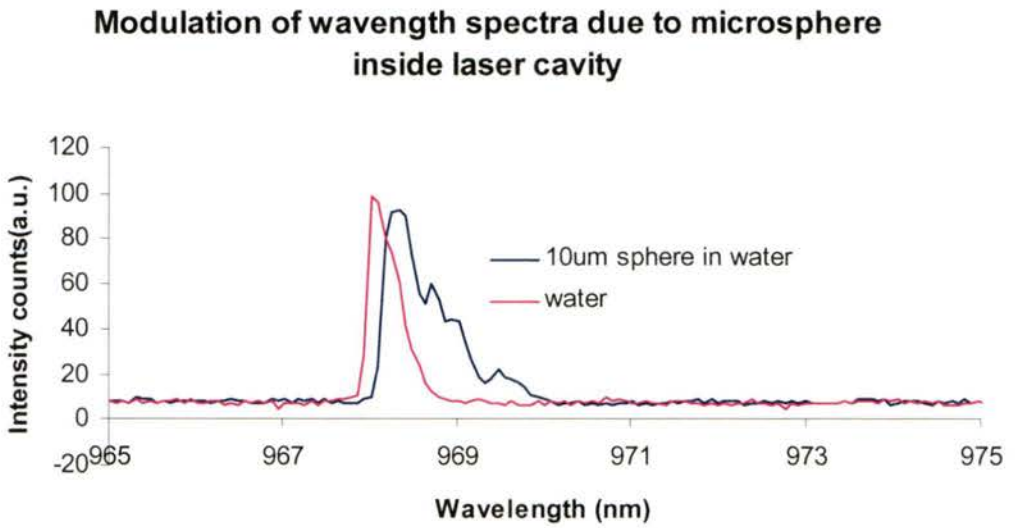

(b)

Figure 5.8 Modulation of wavelength spectrum of NECSEL based fluidic cavity biosensor system by (a) flowing water and (b) flowing a 10μm polystyrene sphere immersed in water into the laser cavity of the sensor.

It can be seen from the above figures that a change in fluid index of the bulk fluidic cavity only induces a wavelength shift of the lowest order mode, while a polystyrene sphere with spherical geometry induces transverse confinement of three higher order modes at longer wavelengths relative to the lowest order mode. There might be some other higher order modes transversely confined, but due to the limited resolution (~0.2-0.3nm) of the spectrometer, they are not resolved. It can also be observed that the relative mode spacings are very small as compared to those in Gourley's results in Figure 5.7. This is because of the different resonator structures having different optical lengths of the resonator cavity in the two biosensor systems. Thus it is of utmost importance that a resonator structure is chosen which is highly sensitive to the modulation of transverse order modes by such perturbations. The next section discusses mode shifts due to changes in fluid index of the fluidic cavity and presents a comparison between the experimentally measured and calculated values.

5.2.4.2 Wavelength shift analysis

The FILD sensor is a coupled cavity resonator, and thus the spacing between longitudinal modes and their dependence on fluid index, are different from those of a simple two mirror resonator. This section presents theoretical explanations to the mode shift analysis of a FILD sensor presented in detail in Appendix B.

In order to determine the modal solutions of a laser resonator, the round trip phase equation must be considered. The wavelengths, at which the round trip phase of a resonator is an integral multiple of 2π, are modal solutions of that resonator. While,

determining the round trip phase equation of a simple two-mirror resonator is fairly easy, it becomes slightly complicated in a coupled cavity resonator. The round trip phase of a two-mirror resonator can be written as

$$k_0\, 2\, n\, L + \theta_1 + \theta_2 = 2\, m\, \pi$$

where k_0 is the wave-vector, n is the refractive index and L is the length of the laser resonator, and m is an integer associated with the mode number. In the above equation, θ_1 are θ_2 are the phase changes due to reflections from the laser mirrors, which are generally very small quantities and can be neglected as compared to the phase change in the laser cavity. On the other hand, in a coupled cavity resonator like a FILD sensor, the reflection from one cavity to the other depends upon the wave-vector k_0. Thus it important that the phase change due to reflection from the coupled cavity must be considered in the round trip phase equation. The round trip phase equation of a coupled cavity resonator can be written as

$$k_0\, 2\, n\, L + \theta_1\, (k_0) + \theta_2 = 2\, m\, \pi$$

The above equation is similar to the phase equation of a two-mirror resonator, except that the phase change $\theta_1\, (k_0)$ from a mirror, (which is also the coupled cavity) is a function of wave-vector, and thus cannot be neglected. This dependence of the round trip phase on wave-vector is explained in detail in Appendix B, where it is observed that a fluid index change from 1 to 1.33 (air to water) in a FILD sensor would induce a longitudinal mode shift of ~10 nm. However, due to finite line-width of the laser diode, (~3 nm) the resonator exhibits mode hopping instead of a single mode shift. Mode hopping is a phenomenon in which a particular mode misaligns and another mode aligns with the gain spectrum of a laser, and shows up on the wavelength spectrum. This can be verified from

Figure 5.8(a), where a spectral shift of ~1nm is observed due to change in fluid index from 1 to 1.33. From the above explanations and the calculations presented in Appendix B, it can be said that the observed ~1nm wavelength shift is due to mode hopping within the linewidth of the laser diode.

The main differentiating factor between Gourley's biocavity laser and the NECSEL based fluidic cavity biosensor is the ratio between fluidic cavity length and total optical cavity length of the laser resonator. The fluidic cavity constitutes a relatively small portion of the total optical cavity length in the FILD sensor as compared to the biocavity laser system. As a result, the same amount of fluidic cavity perturbation induces larger modulation of beam diffraction in a biocavity laser than in the NECSEL based sensor system. It is for this reason, that construction of a top emitting VCSEL based fluidic cavity biosensor system is also discussed in this thesis report. The construction and fabrication details of top emitting VCSEL based fluidic cavity biosensor system are discussed in Chapter 4. Some of the L-I measurements on the top emitting VCSEL based sensor system are presented in Section 5.3. Section 5.3.1 presents calculations of longitudinal mode shifts for the top emitting VCSEL based sensor system.

5.2.5 Beam profile measurements

Far field laser beam profiles of the NECSEL based fluidic cavity sensor were measured by using a Spiricon beam profiling system (model number LBA-7) using an analog CCD camera (SP 980M). Spiricon's partial donation to our research group in the purchase of

the beam profiling system and the analog CCD camera is greatly appreciated. The beam profile measurements were performed on two different sensor systems with both and air and water inside the fluidic cavity. These measurements do not intend to show biosensor functionality, but they do present a comparison between laser beam profiles with air or water inside the fluidic cavity. Figures 5.9 (a) and (b) show laser beam profiles for a NECSEL sensor system with air and water inside the fluidic cavity respectively.

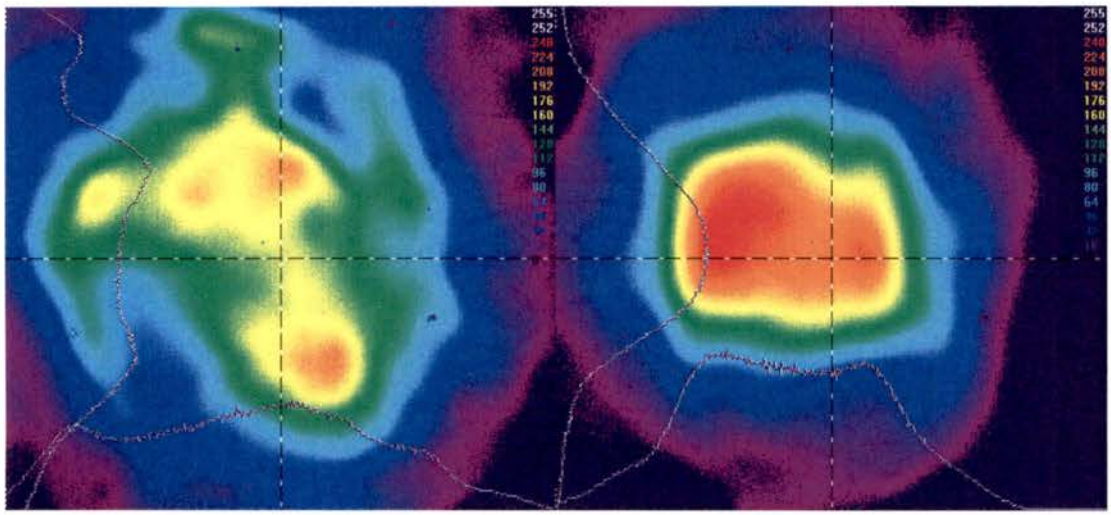

(a) (b)

Figure 5.9 Far field laser beam profiles with (a) air inside the fluidic cavity and (b) water inside the fluidic cavity

It can be seen from the above Figures 5.9(a) and (b), the beam profile of the sensor system looks more like a single mode with water inside the fluidic cavity than with air. It will be discussed in Chapter 6 that an increase in fluidic cavity refractive index improves the beam overlap with the gain region of the laser diode. This in turn decreases the diffraction losses for the fundamental order mode and hence the laser tends to exhibit more single mode behavior.

5.2.6 Other trends of experimental data

Most of the FILD sensor systems constructed by different NECSEL diodes exhibited a similar trend of increase in slope efficiency and decrease in threshold current with increase in fluid index of the fluidic cavity. However, there were some other trends that were exhibited by some sensor systems. It is unclear that if these trends are specific to only certain NECSEL diodes or to any uncontrollable parameter associated with the fabrication of a FILD sensor. This uncontrollable parameter could be an undesirable tilt of the NECSEL diode with respect to the external mirror, or it could be scatter loss due to photoresist particles on the surfaces of the external mirror and NECSEL diodes. There is however an observation of the far field beam profiles with a particular trend of increase in threshold current with increase in fluid index. Figures 5.10 (a) and (b) show the L-I plots and far field beam profiles respectively, of a FILD sensor system exhibiting an increase in threshold current with increasing fluid index.

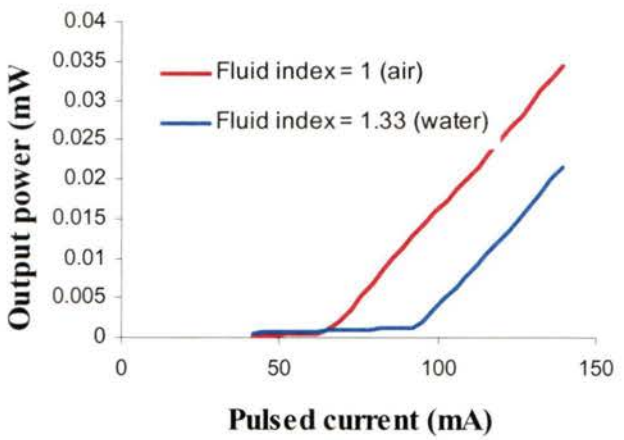

(a)

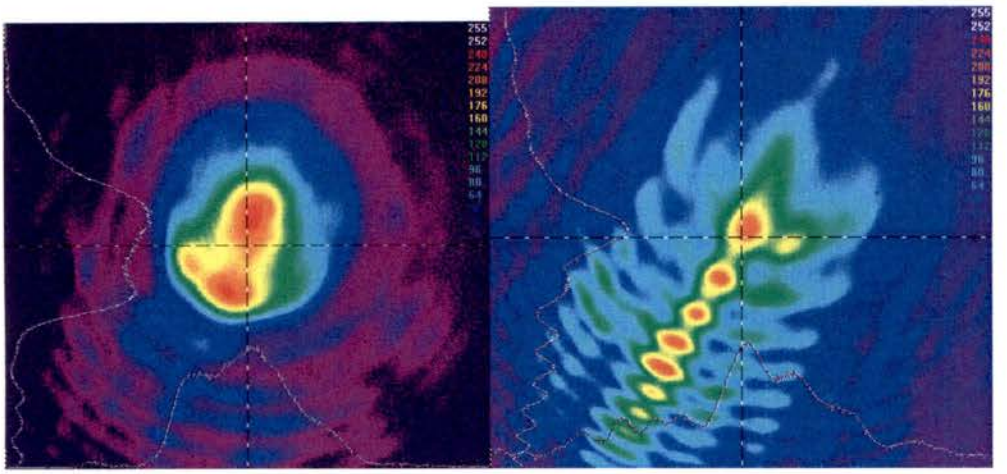

-air inside the fluidic cavity -water inside the fluidic cavity

(b)

Figure 5.10 (a) L-I plots of a FILD sensor system exhibiting an increase in threshold current with increasing fluid refractive index. (b) Far field beam profiles of the associated FILD sensor with air and water inside the fluidic cavity

It can be seen from the Figure 5.10 (b) that the beam profiles of the specific FILD sensor are off-center. The comparison between the two beam profiles suggests that the beam distortion is higher when water is inside the fluidic cavity, and this might account for the increased threshold current exhibited by the FILD sensor system. Due to the skewed nature of the beam profiles, it is assumed that there could be a minute tilt of the NECSEL diode with respect to the external mirror during fabrication of the fluidic cavity. There hasn't been any measurement performed to determine the degree of any possible tilt. The same NECSEL diode was later used to construct another FILD sensor, and the latter L-I measurements are shown in the Figure 5.11.

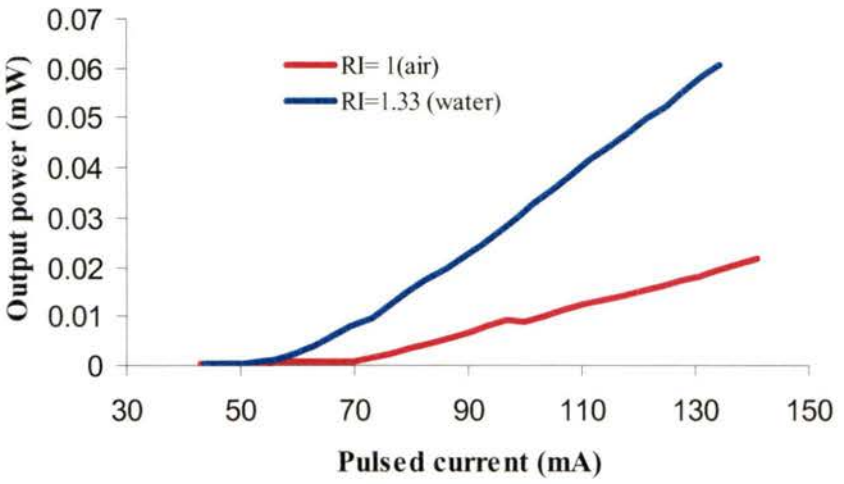

Figure 5.11 L-I plots of a FILD sensor exhibited by the same NECSEL diode which when used in the another sensor, showed a different trend of measurements

From Figure 5.11, it can be said that the trend of an increase in threshold current due to increase in fluid index and off-centered beam profiles are not specific to the NECSEL diode.

Table 5.1 presents numeric values of the threshold currents and slope efficiencies under different fluidic conditions, exhibited by 23 FILD sensor systems constructed from 9 different NECSEL diodes. The table also lists pulse widths, duty cycles, and mentions if the measured far field beam profiles are centered or oblique. RMS surface roughness was measured on only some of the NECSEL substrates and those are also included in the Table 5.1.

Table 5.1 Experimental data on threshold current and slope efficiencies of various FILD sensors constructed by different NECSEL diodes.

NECSEL #	Date measured	FILD Sensor #	Threshold current (mA)			Slope efficiency (mW/A)			Beam profile	Pulse width	Duty cycle	Surface roughness (nm)
			air	water	oil	air	water	oil		(micro second)	(%)	
1	4/28/2004	1	66		50	0.8		1.04		1	1	
	4/13/2004	2	78	68	68	0.65	0.87	0.87		1	10	
	4/12/2004	3	88	75		0.5	0.6			1	1	
2	4/17/2004	4	66.3	55		0.63	1.3		centered	1	1	
	4/21/2004	5	62.5	60		0.74	0.83			1	1	
	5/9/2004	6	66	58	58	1.05	1.19	1.2		1	1	
3	4/14/2004	7	67	89		0.27	0.22		oblique	1	0.1	
	4/21/2004	8	68	62		0.35	0.87		centered	1	0.1	
4	4/14/2004	9	80	68		0.66	0.66			1	0.1	
	4/22/2004	10	58		54	0.79		0.85		1	10	
5	5/9/2004	11	58.6	54.4	58.6	0.52	0.99	1.61		1	1	
6	10/16/2004	12	52	52		1.1	1.3			1	0.1	12.26
	10/26/2004	13	56		63	1.07		1.32		1	10	12.26
	10/30/2004	14	67	63.3		0.7	0.9			0.5	0.25	12.26
	5/26/2005	15	76		97	0.27		0.32		1	0.1	12.26
7	10/16/2004	16	45	58		0.8	1.45			1	0.1	10.4
	10/30/2004	17	45	50		1.43	3.3			0.5	0.25	10.4
	5/26/2005	18	52	60		0.9	1.3			1	0.1	10.4
8	5/26/2005	19	82	95	107	0.4	1	0.74		1	0.1	6
	5/28/2005	20	50		65	0.45		0.55		1	0.1	6
9	5/28/2005	21	82		120	0.11		0.18		1	0.1	16.75
	5/03/2005	22	58		51	0.85		0.68		1	0.1	16.75
	5/26/2005	23	142	161		0.7	0.4			1	1	16.75

Again it can be said that although most of the NECSEL based FILD sensors behaved with the trend of an increase in slope efficiency and decrease in threshold current with an increase in fluid index, and only some of them showed other trends. It is interesting that some of the FILD sensors (7, 8), although constructed by the same NECSEL diode (3) show opposite trends in measurements, exhibiting the variability of an unknown process dependent factor. Chapter 6 presents qualitative and quantitative analysis on the above experimental measurements based on certain theoretical phenomena.

5.3 Top emitting VCSEL based fluidic cavity biosensor system

The top emitting VCSEL used in the fabrication of the prototype top emitting VCSEL based fluidic cavity biosensor system is not well suited for extended cavity applications. It is only used to devise the various fabrication steps and understand the challenges involved in fabrication of an ideal extended cavity-top emitting VCSEL based biosensor system. However, the device is tested for functionality. Figure 5.12 shows L-I characteristics of the top emitting VCSEL device, with and without an external mirror, and with water inside the fluidic cavity.

It can be seen from this figure that the characteristics of the top emitting VCSEL are modulated when optical feedback is provided to the laser diode by an external mirror with and without fluid inside the laser cavity. These characteristics are measured just for the proof the concept and they are not intended to exhibit any sort of sensing.

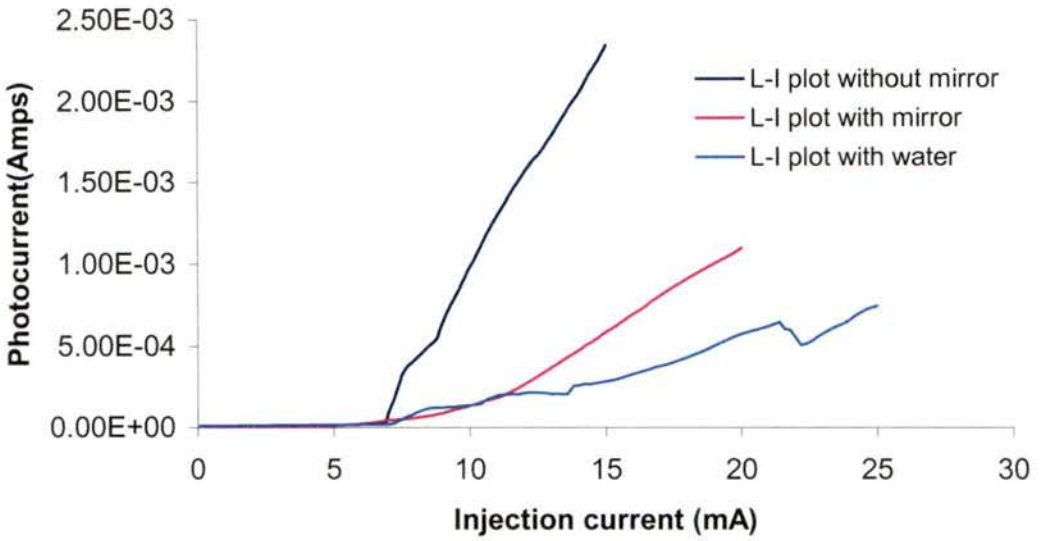

Figure 5.12L-I characteristics of top emitting VCSEL under different conditions

5.3.1 Transverse confinement of laser beam

Spectral measurements were also performed on the top emitting VCSEL based sensors but because of the difficulties in coupling light from the sensor systems to the Acton research optical spectrum analyzer, a wavelength spectrum could not be measured. While the shorter overall cavity length of the top-emitting structure would be expected to give a greater change in wavelength for a given shift in fluid index, the reflectivity of the interior mirror, in this case the top p-DBR, also affects the wavelength sensitivity of the coupled cavity resonator.

In an ideal top emitting VCSEL based fluidic cavity sensor, the top DBR must be partial and less reflective. This will result in increase in circulating power in the fluidic cavity

and thus greater interaction of light with the fluid. The details about the expected mode shift analysis and theoretical explanation are given in Section 5.2.4.2 and in Appendix B.

5.4 Summary

This chapter presents the construction of a special experimental setup for testing of the biosensor devices and discusses and addresses the various requirements for biosensor testing. It also presents the experimental results obtained on bottom and top-emitting VCSEL based biosensor and proves the concept of electrically pumped vertical cavity surface emitting laser based fluidic cavity biosensor. It was observed that the FILD sensors exhibited different trends of measurements of output characteristics with change in fluid index. The most common trend was increase in slope efficiency and decrease in threshold current with increase in fluid index. The wavelength spectra measurements and the associated spectral analysis in Appendix B suggests occurrence of mode-hopping due to change in fluid index from 1 to 1.33.

References:

[1] A.Siegman, Lasers, Chapter 19

[2] P. L. Gourley, "Biocavity laser for high-speed cell and tumor biology", *Journal of Applied Physics D*, 36 pp R228-R239 (2003)

Chapter 6

Theoretical modeling and simulations

INTRODUCTION

From Table 5.1, it was observed that the threshold current and slope efficiency of most of the FILD sensors decreases and increases respectively with increase in fluid refractive index inside the fluidic cavity. It was also demonstrated by a sequence of four frames of a movie captured by a digital camera that the light intensity of the fluidic intracavity laser diode sensor, increased when water was introduced inside the fluidic cavity. It is important to analyze physical principles that can explain the experimental data qualitatively and quantitatively. This chapter presents theoretical investigations of the five different phenomena that are either directly or indirectly associated with the modulation of laser threshold current and slope efficiency of laser diode. Qualitative analysis of these phenomena is compared to the different trends of the experimental data shown in Table 5.1. This chapter intends to present a comprehensive study of the possible mechanisms. Table 6.1 lists all five phenomena with corresponding effects on slope efficiency and threshold current of an increase in fluid refractive index. The last column of the table suggests if the specific theoretical phenomenon "agrees" or "disagrees" with the most common trend of experimental measurements, which is an increase in slope efficiency and decrease of threshold current with an increase in fluid index. The red and blue arrows in the table indicate if the physical property increases or decreases with an increase in refractive index of the fluid inside the laser cavity.

Table 6.1 Theoretical phenomena agreeing or disagreeing with the most common trend of experimental data

1	Reflection at laser diode's substrate-fluid cavity interface ↑	η ↓	J_{th} ↓	**DISAGREE**
2	Absorption losses inside the fluid cavity ↑	η ↓	J_{th} ↑	**DISAGREE**
3	Cooling due to fluid ↑	η ↑	J_{th} ↑ or ↓	**AGREE OR DISAGREE**
4	Scattering losses at laser diode's substrate-fluid cavity interface ↓	η ↑	J_{th} ↓	**AGREE**
5	Transverse confinement of laser beam at the gain region ↑	η ↑	J_{th} ↓	**AGREE**

η=Slope efficiency J_{th} = Threshold current density

Before each one of the above phenomena is discussed in detail, it is important to analyze the actual resonator configuration and compare it with the two versions of approximate models used in the subsequent explanations. This chapter thus first presents a section on resonator construction, which is followed by another section with five sub-sections on the theoretical phenomena listed above.

6.1 Resonator construction

As already described in Chapter 4, the FILD sensor consists of a bottom emitting vertical cavity surface emitting laser diode, a microfluidic channel and an external dielectric mirror. The epitaxial structure of the laser diode, properties of the external mirror and the fabrication of the complete FILD sensor has already been discussed in Chapter 3 and 4. This section presents two resonator models of the FILD sensor used in the theoretical phenomena and compares them with the actual resonator configuration.

6.1.1 Actual configuration of the FILD sensor resonator

The FILD sensor resonator consists of three mirrors: the top distributed Bragg reflector (top DBR), bottom DBR and an external dielectric mirror. In addition, there is a substrate-fluidic cavity interface, where there is an abrupt discontinuity in refractive index within the resonator. Figures 6.1 (a) and (b) show a cross sectional schematic diagram and the corresponding resonator diagram of the FILD sensor.

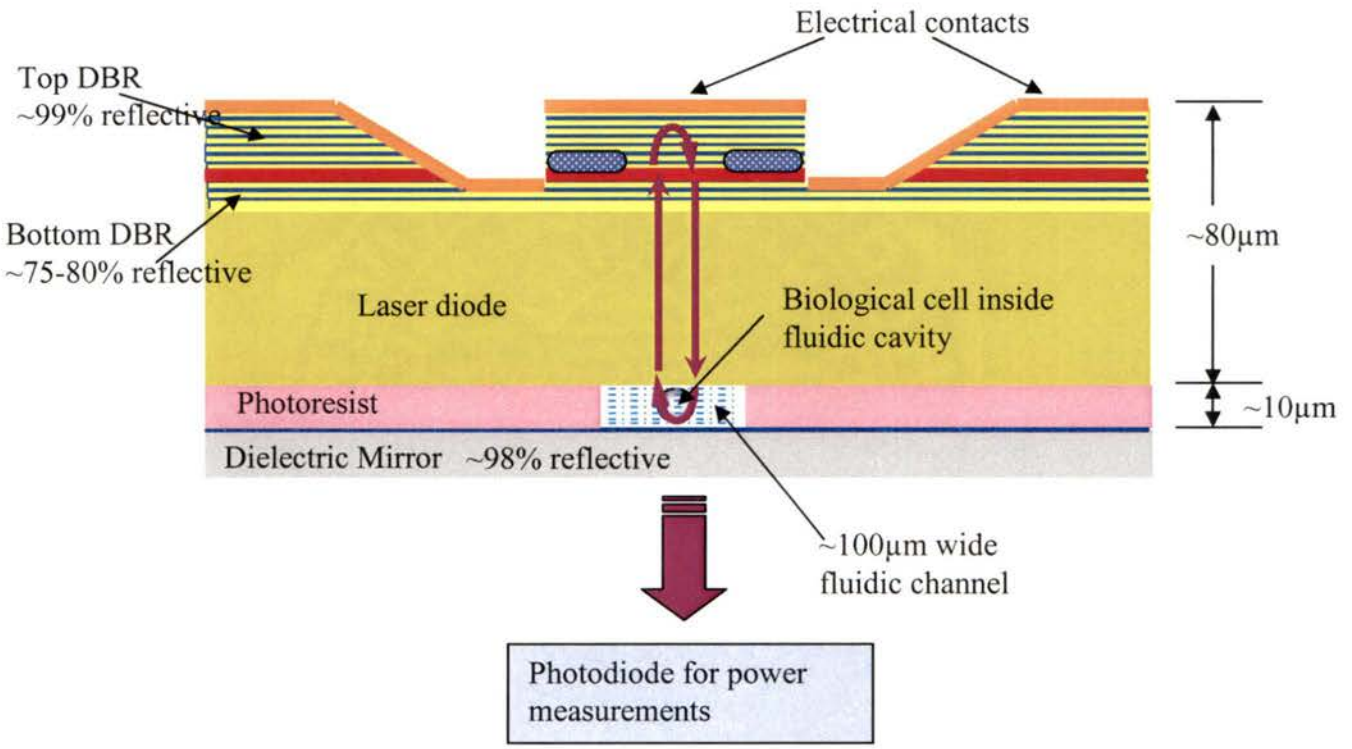

Figure 6.1 (a) Schematic diagram of NECSEL based fluidic cavity biosensor system or FILD sensor

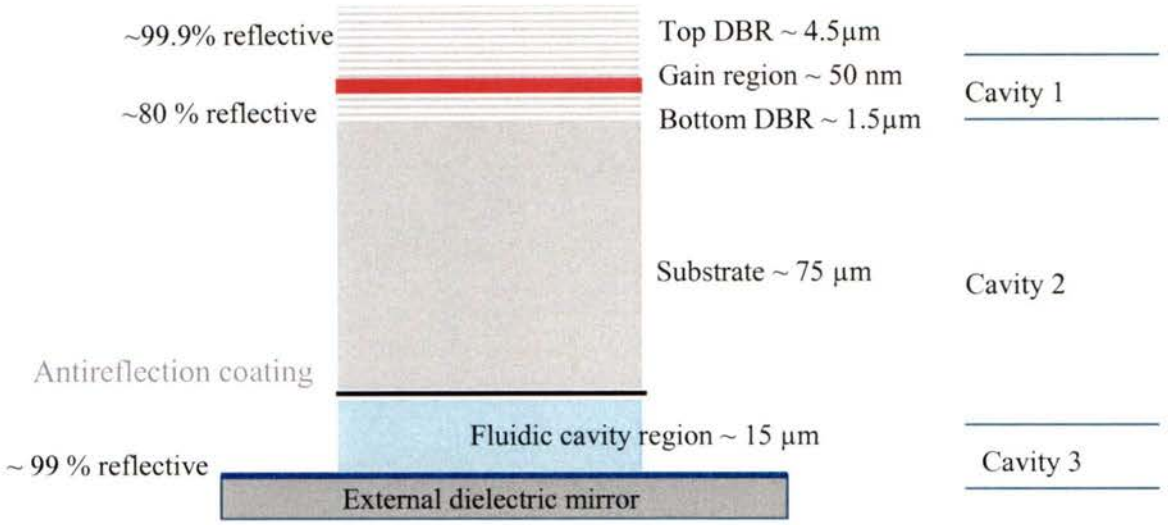

Figure 6.1 (b) Resonator diagram of the FILD sensor

As already mentioned in Section 4.1.1, the top DBR has 33 pairs of AlGaAs-GaAs layers, which corresponds to an approximate power reflectivity of ~99.9 %, and the bottom DBR has 10 pairs, corresponding to an approximate reflectivity of ~80 % at the lasing wavelength (980 nm). The external mirror has a reflectivity of 99 %. The substrate has an anti-reflective coating at the fluidic cavity interface, which nulls any back reflection from the interface when the adjacent medium is air.

As seen from Figure 6.1 (b), there are three cavities in the FILD sensor resonator. The first cavity is between the top DBR and the bottom DBR, which contains the gain region providing gain to the complete resonator. The second cavity is the passive substrate region between the bottom DBR and the substrate-fluidic cavity interface. The third cavity is the fluidic cavity, which is the region between laser diode and external dielectric mirror. The complete structure is a coupled cavity resonator, which is quite complicated

to analyze, and is thus simplified to two different approximate resonator models for mathematical analysis.

6.1.2 Resonator configurations for modeling

The theoretical phenomena discussed in this chapter can be divided into two categories. The first category involves calculation of modulated optical power within the sensor resonator and thus requires only numerical values of the mirror reflectivities, gain and loss coefficients and optical lengths of the three cavities within the resonator. The second category involves analysis of laser beam propagation within the resonator, and thus requires information about the gain region's transverse profile, the shape of the resonator mirrors, and the temperature of the laser during operation. The different requirements of the two categories for mathematical analysis necessitated two different resonator structures, both of which are simplified versions of the actual resonator structure (Figure 6.1 (b)). The key idea behind constructing two different simplified resonators is to convert the complicated 3-cavity resonator into a single cavity resonator for easy analysis.

6.1.2.1 Gain and loss modeling

The actual and the simplified resonator models of a FILD sensor, for performing optical power calculations are shown in Figures 6.2(a) and (b) respectively. The simplified resonator model (Figure 6.2 (b)) has two mirrors M_1 and M_{eff}, with reflection coefficients r_1 and r_{eff} respectively. The mirror M_1 represents a hard mirror for the top DBR and the mirror M_{eff} represents the bottom DBR and external mirror and the cavity between them.

The key idea of this resonator model is to simplify the complex three-mirror resonator to a simple two-mirror configuration. The reflection coefficient of the mirror M_{eff} is calculated by transfer matrix method and is discussed in detail in the respective theoretical phenomenon in Section 6.2. The simplified resonator also consists of a 50 nm thick gain region, which represents the narrow quantum wells inside the laser diode.

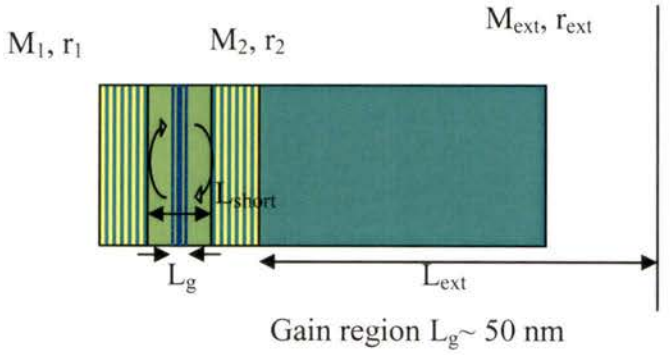

(a)

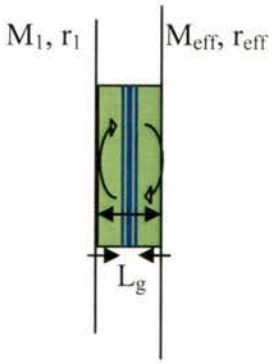

(b)

Figure 6.2 (a) Actual FILD sensor resonator model and (b) the simplified version of the FILD sensor resonator for optical gain and loss modeling

The mirror M_{eff} includes the fluidic cavity region and any perturbation of the fluidic cavity index modulates the effective reflection coefficient r_{eff}. Thus the effective reflection coefficient r_{eff} is a function of all the physical properties perturbed by a fluid flowing into the fluidic cavity, such as refractive index, absorption coefficient etc. Since the threshold gain and slope efficiency of the FILD sensor are functions of the effective reflection coefficient r_{eff}, the effects of fluidic cavity perturbation can be analyzed with this method. Appendix C presents calculations of the effective reflection coefficient of the lumped extended cavity and discusses its dependence on fluid index. Appendix B also shows coupled cavity mode calculations of a FILD sensor that utilize the above resonator simplification. Appendix D utilizes both the above simplified resonator model and the one discussed in next section to perform calculations on transverse beam confinement and associated perturbation effects on laser characteristics.

6.1.2.2 Beam propagation modeling

The simplified device structure and resonator model for modeling laser beam propagation within the resonator are shown in Figures 6.3(a) and (b) respectively. The resonator model is different from the one discussed in the previous section, as it does not require information about the mirrors' reflectivity. This model is more dependent on the transverse profile of the mirrors and gain region. In this model, a single hard mirror M_1, together represents the epitaxially grown top and bottom DBRs and the gain region of the laser diode. This assumption is valid because the bottom DBR is less reflective (~80%) as compared to the top reflector (99.9%) and external mirror (~99%). It also assumes that the majority of the diffraction occurs within the substrate and fluidic cavity, which is

reasonable due to the relatively long L/n values of these regions. Note the L/n ratio of the epitaxial cavity must be multiplied by the epitaxial cavity finesse before comparing it to the substrate and fluidic cavity L/n. Due to thermal lensing effects, the diffraction losses inside the laser diode are temperature dependent. Section 6.2.4 discuss more about the simplified resonator structure and explains the relation between device temperature and mirror curvature. Figure 6.3 (a) and (b) show the simplified device structure and resonator diagrams for beam propagation analysis.

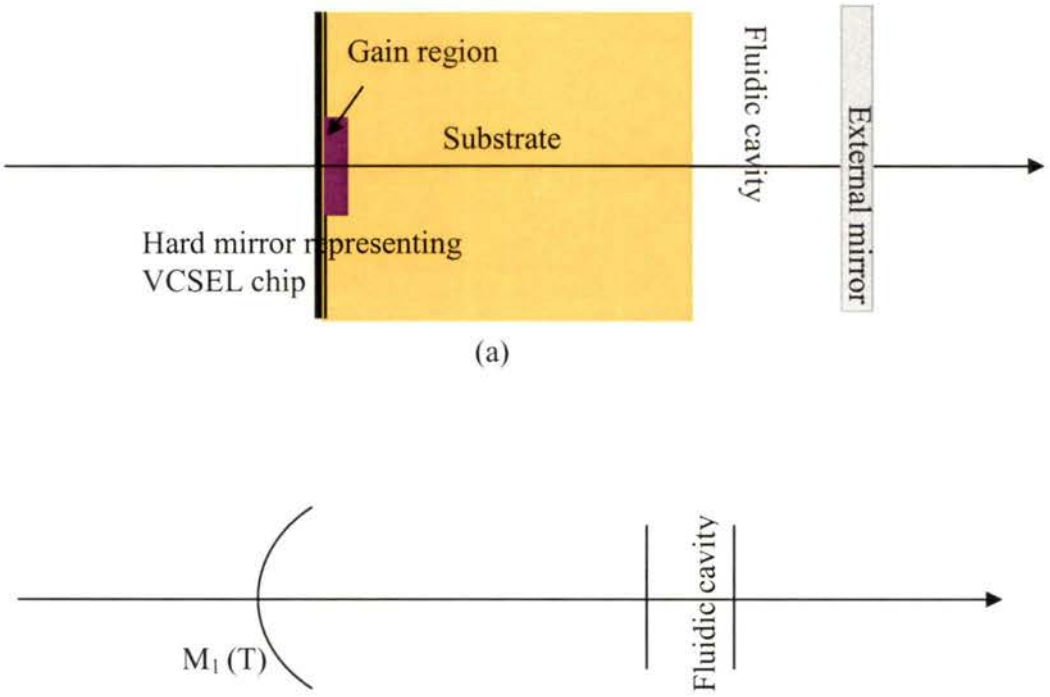

Figure 6.3 (a) Simplified device structure and (b) resonator diagrams for beam propagation analysis

This resonator model analyzes the beam propagation inside the FILD sensor. Under constant temperature conditions, and hence constant mirror curvatures, the diffraction of the laser beam inside the resonator is modeled, and its modulation is analyzed due to perturbation in the fluidic cavity. Modulation of diffraction losses are further associated with threshold gain and slope efficiency of the FILD sensor. Sections 6.2.3 and 6.2.4 utilize this resonator construction to explain the respective theoretical phenomenon. Appendix D presents calculations of transverse confinement factor and its dependence on fluid index, by utilizing this resonator model.

6.2 Theoretical phenomena

This section discuss in detail five theoretical phenomena to qualitatively and quantitatively explain the experimental results on the FILD sensor's threshold current and slope efficiency due to perturbation in fluidic cavity refractive index. They are discussed in this chapter to present a comprehensive analysis of the physics of the FILD sensors. The following subsections start with a qualitative analysis of the respective phenomenon, and if they conform to the most common trend observed, then a rigorous mathematical calculation is followed.

6.2.1 Reflection at substrate to fluidic cavity interface

An abrupt discontinuity in refractive index between the substrate (n = 3.57) and fluidic cavity region (n = 1~1.4) would induce modulation of back reflection into the substrate. Without an antireflection coating, the power reflectivity at this interface would change from ~30 % to ~18% as the fluid changes from air to water, which can cause a significant

amount of modulation of threshold current and slope efficiency. However, due to the presence of an antireflection coating at this interface, there is no back reflection when fluidic cavity index is equal to 1. The reflection coefficient r_{eff}, of the passive cavity equivalent mirror M_{eff} is analyzed in this section. It turns out that the magnitude of the effective reflection coefficient is a monotonically increasing function of refractive index of the fluid. An increase in reflectivity of a laser end mirror results in a decrease of the threshold current and differential slope efficiency. This phenomenon thus does not conform to the most common trend of experimental measurements, where, an increase in slope efficiency is observed along with a decrease in threshold current. However it does match with the trend of the L-I measurements exhibited by FILD sensor 22 constructed by using NECSEL 9, from Table 5.1. The next couple of paragraphs present analysis of r_{eff}, as a function of refractive index of the fluid, using transfer matrix method.

The transfer matrix method is utilized here to analyze the effective reflection coefficient r_{eff}. A transfer matrix relates the amplitudes of the left and right going electric fields between two sides of a dielectric interface or a dielectric propagation medium. The transfer matrix theory allows cascading of two or more matrices, which simplifies calculation of reflection or transmission coefficients of complicated dielectric structures. More details on transfer matrix theory can be found in [2]. Figure 6.4 shows the actual dielectric structure of the mirror, M_{eff} of the FILD sensor. It can be seen here that there are four dielectric interfaces and three different dielectric propagation mediums. By cascading the transfer matrices of all these seven dielectric elements, a transfer matrix is formed, which represents the complete dielectric structure.

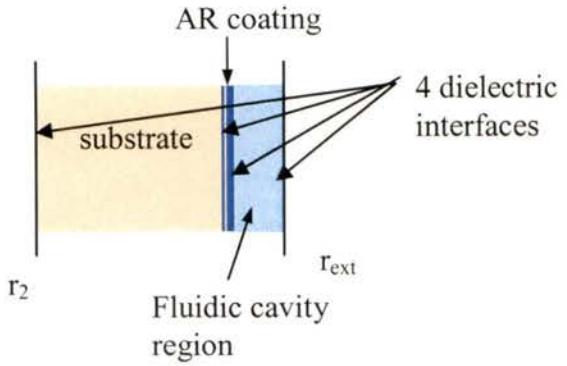

Figure 6.4 Dielectric structure of the passive cavity region of the FILD sensor

In Figure 6.4, r_2 represents the reflection coefficient of the bottom DBR and r_{ext} represents that of the external mirror. The transfer matrices of the individual elements and the calculation of the effective reflection coefficient are given in Appendix C. Figure 6.5 shows a plot of the effective reflection coefficient's magnitude squared as a function of refractive index of the fluid. It can be seen here that the reflection of the end mirror increases with an increase in fluid index, and thus does not conform with the most common trend of experimental results.

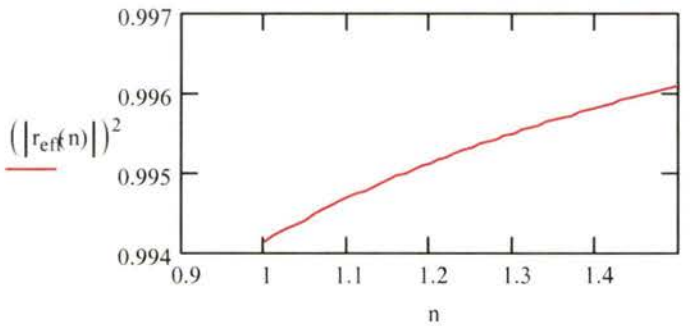

Figure 6.5 Reflectivity of the mirror M_{eff} as a function of refractive index of the fluidic cavity

6.2.2 Absorption losses inside fluidic cavity

Different fluids have different absorption coefficients at the lasing wavelength. Thus, when a FILD sensor is perturbed with a change in absorption losses inside the laser cavity, it may result in modulation of threshold current and slope efficiency. The fluids, water and diffusion pump oil used in the experiments, are expected to have a higher absorption coefficient than that of air. Thus an increase in absorption losses with increase in fluid index is a viable assumption made in this study. Since the fluidic cavity is an integral part of the laser resonator, the losses incurred due to optical absorption by fluids adds to the laser internal losses. Since the threshold current increases and slope efficiency decreases with an increase in internal losses, it can be said here that this phenomenon also does not conform to the most common trend of experimental data. It does match with the measurements exhibited by the FILD sensors 23 and 7 constructed by NECSEL diodes 9 and 3 respectively, from Table 5.1.

6.2.3 Transverse confinement of laser beam at gain region

As already discussed in detail in Section 5.2.4.1, transverse confinement of a laser beam is sensitive to any perturbation of refractive index inside the laser resonator. If a fluid with homogeneous refractive index profile, or to a greater extent, a biological cell, with a non-uniform and sophisticated index profile flows into the laser cavity, it will perturb the optical field inside the resonator, and modulate the transverse confinement of laser beam. Such a perturbation may have a direct impact on the laser beam's spatial profile at the gain region, and hence the modal frequencies. The other physical properties of the FILD sensor that could be indirectly affected are threshold current and slope efficiency. While

it is difficult to analyze the perturbation effects on laser properties due to an inhomogenous biological cell (or polystyrene sphere), this section presents mathematical analysis on modulation of laser properties due to perturbation by a fluid with a homogenous refractive index profile, i.e. constant refractive index.

6.2.3.1 Plano concave resonator

This phenomenon can be understood intuitively by considering a plano-concave laser resonator. For a stable resonator configuration, the wavefronts of the laser beam must match with the radius of curvature of the end mirrors. That is, the radius of the beam wavefront must be equal to R at the curved mirror and infinity at the plane mirror (Figures 6.6 (a) & (b)). A simple Gaussian beam analysis of such a resonator suggests that if the length of the resonator is decreased, the beam spot sizes at the end mirrors also decrease [3]. This further implies that the laser beam has to diffract more in order to match with the end mirror's radius of curvature, to retain the stability of the resonator configuration. Figure 6.6 (a) and (b) schematically show laser beam paths within the plano-concave resonator.

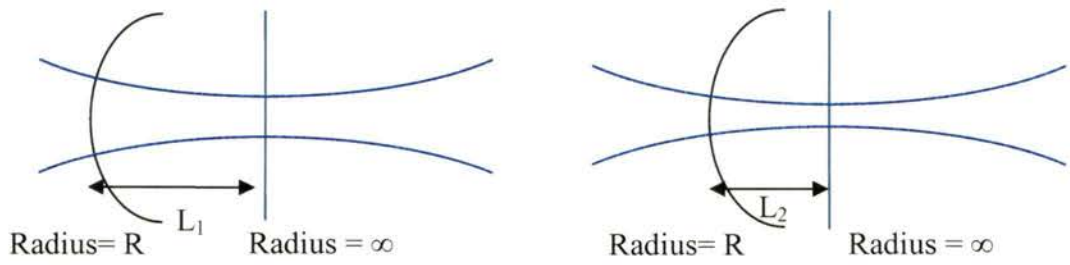

Figure 6.6 Plano-concave resonators with resonator lengths (a) L_1 (b) L_2 with $L_1 > L_2$

Consider a gain region of fixed transverse width and longitudinal thickness is defined close to the curved mirror (See Figures 6.7). Also consider that the gain region is surrounded by loss region in the transverse plane. In such a case, a change in length of the laser resonator can modulate the overlap of the laser beam with the gain and loss regions. If the resonator length is decreased by a small amount, the beam widths at both the end mirrors decrease, and thus the laser beam overlaps more with the (green shaded) gain region and less with the (red shaded) loss region. This implies that the laser beam will incur less loss and more gain inside the resonator, which will improve the laser's output efficiency and decrease the input power required for laser threshold.

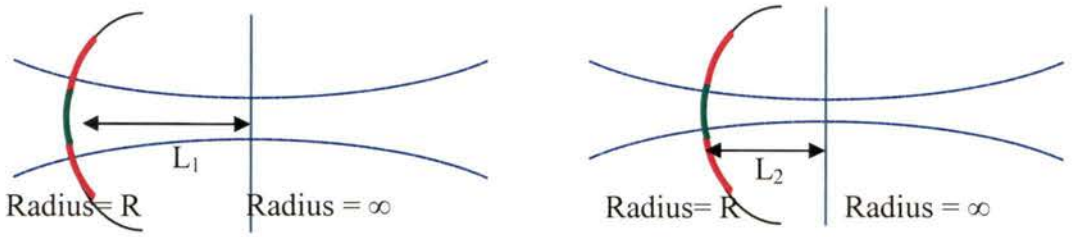

(a) (b)

Figure 6.7 Plano concave resonators with transversely defined gain and loss regions and resonator lengths. (a) L1 and (b) L2 with L1>L2

The above example of the laser resonator represents the actual FILD sensor, except there is no physical change in the resonator's length. Also, none of the FILD sensor's mirrors are physically curved, but the thermal lens provides focusing. However, an analogy can still be drawn between the two models, the details of which are given in the next paragraph.

6.2.3.2 Analogy with the FILD sensor

The optical length of a laser resonator can either be taken as nL or L/n, where L is the physical length of the cavity and n is the refractive index of the physical medium, depending on the type of optical phenomena. When the phase information is analyzed, then the product "nL" is generally considered, and when diffraction of the laser beam is investigated, the L/n ratio represents the normalized optical length of the medium. For the present case of FILD sensor analysis, the laser beam's diffraction is studied, and thus the ratio L/n is considered. Thus an increase in refractive index of the fluidic cavity can be considered as a decrease in normalized length of the laser resonator. For the FILD sensor, there is an approximately 7% decrease in the optical length of the laser resonator when air in a 10μm thick fluidic cavity is replaced with water.

Additionally, the NECSEL chip itself can be considered as a curved mirror with transversely defined gain and loss regions. The comparison between a curved mirror and NECSEL chip can be better understood by considering the thermal lensing effect exhibited by ion-implanted and selectively oxidized VCSEL diodes [4] [5]. Thermal lensing is a phenomenon most common in ion-implanted VCSELs, in which the heat generated inside the laser diode due to non-radiative recombination of carriers and resistive heating at the current path produces a temperature rise, and hence a refractive index profile which tends to focus the laser beam modes, and thus reduce diffraction losses. The degree of 'lensing effect' depends upon the thermal resistance and temperature difference between the center and edge of the laser diode. In the simplified resonator for the FILD sensor system, a single curved mirror represents thermal lensing

for top DBR, bottom DBR and the gain region, with a temperature dependent radius of curvature of the mirror. The relation between temperature and the mirror's curvature is explained as under.

6.2.3.3 Thermal mirror's radius of curvature

In order to determine the focal length of the thermal lens, it is important to first determine the temperature difference ΔT between the center and the edge of the device. For InGaAs devices, the rate of change of refractive index with temperature is given as $\partial n/\partial t \approx 10^{-4}$ /°K. Thus for a temperature difference of ΔT, the increase in refractive index at the center of the diode is given by

$$\Delta n = (\partial n/\partial t)\, \Delta T$$

Now assuming that the refractive index at the gain region has a parabolic profile

$$n(r) = n_1 - \tfrac{1}{2} n_2 r^2 \qquad \text{where } n_1 = n_{center} = n_{edge} + \Delta n \text{ and } n_2 = -\partial^2 n/\partial r^2$$

If the thickness of the VCSEL's thermally affected region is Δz, which in this case is assumed to be that of the gain region, and top and bottom DBRs, then the focal length of the thermal lens is given by [6,7]

$f = \dfrac{1}{n_2 \Delta z}$ and the radius of curvature is given by $R = \dfrac{2}{n_2 \Delta z}$

From the above equations,

$n_2 = \frac{2\Delta n}{r_{edge}^2}$ where r_{edge} is the radius of the laser diode's gain aperture, and thus

$$f = \frac{r_{edge}^2}{2\Delta n\, \Delta z} \qquad \text{or} \qquad R = \frac{r_{edge}^2}{\Delta n\, \Delta z}$$

It will be discussed in Section 6.2.4, that $\Delta T < 2$ C, and thus $R \cong 6$m.

Lastly the gain and the loss regions depicted in Figures 6.7 can also be compared to those in an ion-implanted VCSEL. In a real ion-implanted VCSEL, the current confinement aperture is defined by implanting (or damaging) certain area of the epitaxially grown top DBR . The damaged region surrounds the non-damaged active region thus preventing the quantum wells outside the active region from being electrically injected, contributing to loss in the optical fields outside the active region. The quantum wells under the non-damaged circular region contributes gain to the optical fields in the laser cavity. The red and green colored regions thus represent the loss and gain respectively to an optical field in Figures 6.7.

So far, this section has presented a simplified FILD sensor-resonator model, and some technical arguments to develop an understanding of modulation of transverse confinement of laser beam and its effects on cavity gain and losses. In the next few paragraphs and sub-sections, two different approaches are discussed to analyze the beam profile and associated phenomena. Those two approaches are:

1. Ray matrix method
2. Fox-Li approach

In both of the two approaches, a fundamental Gaussian beam is propagated inside the simplified model of the FILD sensor resonator. The goal of both the analyses is to quantitatively determine the modulation of beam overlap with the gain region due to change in fluid index in the fluidic cavity. This is achieved by calculating the transverse confinement factor Γ_{xy} at the gain region, which turns out to be a function of refractive index of the fluidic cavity. Γ_{xy} is defined as the fraction of the total optical energy that overlaps with the gain region. The details of each of the above two approaches are given in the next sub-sections.

6.2.3.4 Ray matrix method

A ray matrix of a dielectric element is a characteristic of its reflective, refractive and diffractive capabilities. In the words of Siegman [7], "Ray matrices or ABCD matrices are widely used to describe the propagation of geometrical optical rays through paraxial optical elements, such as lenses, curved mirrors and ducts. These ray matrices also turn out to be very useful for describing a large number of other optical beam and resonator problems, including even problems that involve the diffractive nature of light." A ray matrix of a dielectric element, relates the radial position and slope of an input ray to those of an output ray from that element. Just like in transfer matrices, ray matrices can also be cascaded to construct bigger ray matrices for complicated optical systems. More details

and derivations for determining ray matrices for basic optical elements are discussed in Reference [8].

The ray matrix approach used to analyze laser beam's transverse confinement in the FILD sensor is fairly simple. A ray matrix of the complete resonator is constructed by cascading matrices of the individual elements, which are the curved mirror (thermal mirror), gain region, and the propagation medium (substrate and fluidic cavity). A fundamental order Gaussian beam is propagated inside the resonator by determining the values of the complex 'q-parameter' at the end mirrors. The 'q-parameter' is defined as the complex radius of the Gaussian beam, and it contains information about the beam spot size and the radius of curvature of the beam's wavefront at a particular position. The q parameter is first determined at one of the end mirrors by propagating a Gaussian beam for one round-trip inside the resonator, and the condition that the beam radius is conserved after one round-trip helps in determining a q value at that mirror. From the complex q parameter values, an electric field distribution can be determined at the specific transverse planes by using Gaussian beam formulas. The electric field distribution at the gain region is analyzed as a function of refractive index of the fluid. From this distribution, the overlap of the laser beam with the gain region is analyzed, and transverse confinement factor is evaluated. Appendix D presents all the calculations done to evaluate transverse confinement factor by using the ray matrix method. It is found that the relative change in transverse confinement factor is about 2 % for a refractive index change from air to water in the fluid channel.

While analyzing the beam overlap at the gain region in Appendix D, it is assumed that radius of curvature of the thermal mirror is 6m, which was calculated in Section 6.2.3.3 based on the results obtained from thermal resistance measurements presented in Section 6.2.4. It is interesting to determine if the mode profile at the gain region is defined by thermal lensing or the gain guiding effects. Appendix D plots the beam waist at the gain region as a function of the thermal mirror's radius of curvature under two different conditions. These conditions correspond to the unity gain ABCD matrix and the ABCD matrix for parabolic gain approximation respectively. Figures 6.8 (a) and (b) show the beam waist vs. thermal mirror's radius plots for the two conditions.

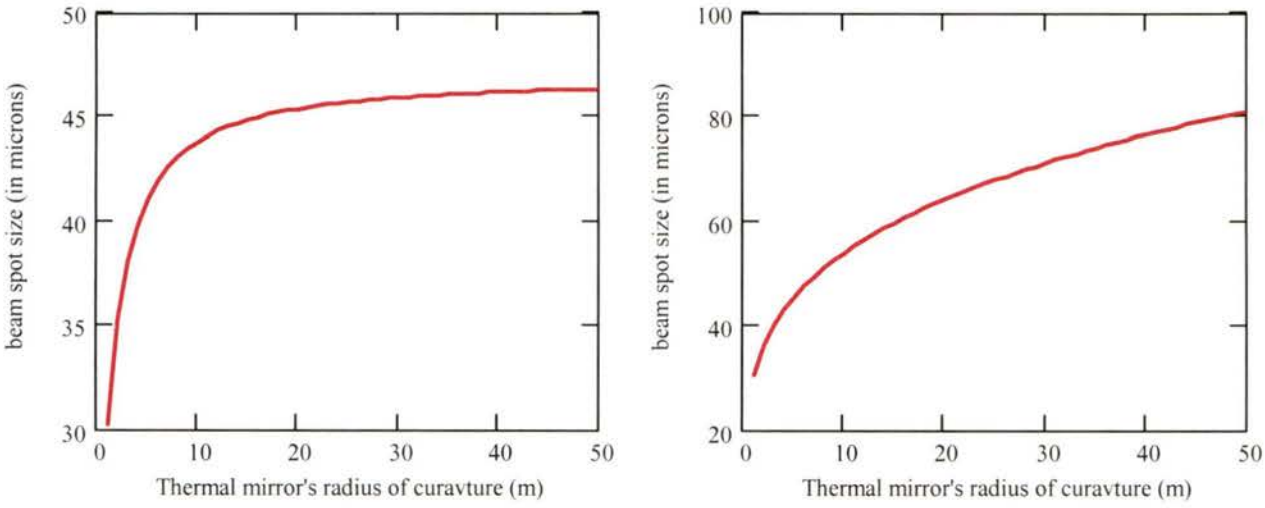

(a) (b)

Figure 6.8 Beam spot diameter vs. thermal mirror radius of curvature for FILD sensor resonator with (a) parabolic gain approximation and (b) unity gain (or no gain) approximation

It can be seen from the above figures, that the beam spot size is mainly defined by gain guiding for thermal mirror's radii greater than ~20m. At R=6m (for the FILD sensor), the spot size is defined both by gain guiding and thermal lensing effects.

6.2.3.5 Fox-Li approach

In 1960, A.G. Fox and Tingye Li introduced a numerical method to study diffraction of electromagnetic waves in optical interferometers [9]. In this method, an initially launched electromagnetic wave is propagated back and forth between the mirrors of the resonator using numerical calculations of electric fields within the resonator. It was found that after many round-trips of the electric field, a steady state is reached and the field distributions inside the resonator do not change. This approach is used to determine electric field distributions at the gain region of the FILD sensor, with and without perturbations to the fluidic cavity. By comparing these field distributions, the modulation of laser beam transverse confinement can be analyzed.

To implement this method, a prototype resonator structure is designed in RSoft's beam propagation software. The structure is then repeated a number of times to model back and forth reflection of electric fields inside the effectively unfolded resonator. Different electric field distributions are launched at the beginning of the structure and the steady state field distributions are analyzed, with and without perturbation of the fluidic cavity. From this analysis, it was found that the relative change in transverse confinement factor is less than 1 %. The structure design is shown in Figures 6.9. Note that the above

structure is repeated several times with alternate inverted and non-inverted geometry to simulate for back and forth beam propagation inside the laser resonator.

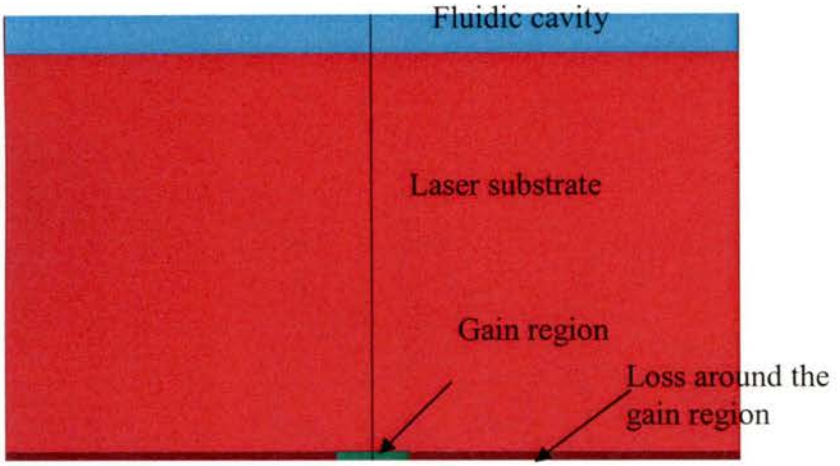

Figure 6.9 FILD sensor resonator designed in RSoft's beam propagation software.

6.2.3.6 Transverse confinement factor analysis

Both, the ABCD ray matrix and Fox & Li approaches suggested that there is an approximately 1-2% increase in transverse confinement factor Γ_{xy} with an increase in fluid index from 1(air) to 1.33(water). Appendix D presents a quantitative analysis on the change in threshold current and slope efficiency of the FILD sensor due to ~2% increase in transverse confinement. This corresponds to an approximate increase in slope efficiency by ~1.3 % and decrease in threshold gain by ~3%. From Table 5.1, it was observed that more than 50 % of the FILD sensors exhibited a trend of increase in slope efficiency and decrease in threshold current with increase in fluid index. The average relative increase in slope efficiency is ~60 % and decrease in threshold current is ~16 %. Thus it can be said that although the most common trend of experimental data

qualitatively matches with this theoretical phenomenon, the observed relative changes in the slope efficiencies and threshold currents are an order of magnitude higher than those predicted by the calculations.

.

6.2.4 Cooling due to fluid

Another important phenomenon that might explain one of the trends of experimental results is due to a possible heat exchange between fluid and the laser diode. As already discussed in Sections 2.3 and 6.2.3, a NECSEL diode is an ion-implanted device, and can exhibit thermal lensing effects. Thermal lensing can affect the diffraction losses incurred by the laser beam and hence the modulation of lensing effects with a change in fluid index is critical to the sensor operation. This section investigates if the thermal operating conditions are the same under different fluid conditions inside the fluidic cavity.

Figures 6.10 (a) and (b) shows graphs plotting wavelengths of various longitudinal modes of the FILD sensor as a function of input power for air and water inside the fluidic cavity respectively. These measurements show that the modal wavelength shifts towards higher values with an increase in input power. This is a thermal phenomenon, and such a measurement helps in determining the thermal resistance of a laser diode. It was found from these measurements that the wavelength shift is about 40 nm/W with air inside the fluidic cavity and about 20 nm/W with water inside the fluidic cavity. For InGaAs laser diodes, the cavity mode wavelength shifts by approximately 0.08 nm with an increase in device temperature by 1°C. Thus the thermal resistances for the FILD sensor are

approximately 500 °C/W and 250 °C/W for air and water inside the fluid cavity respectively.

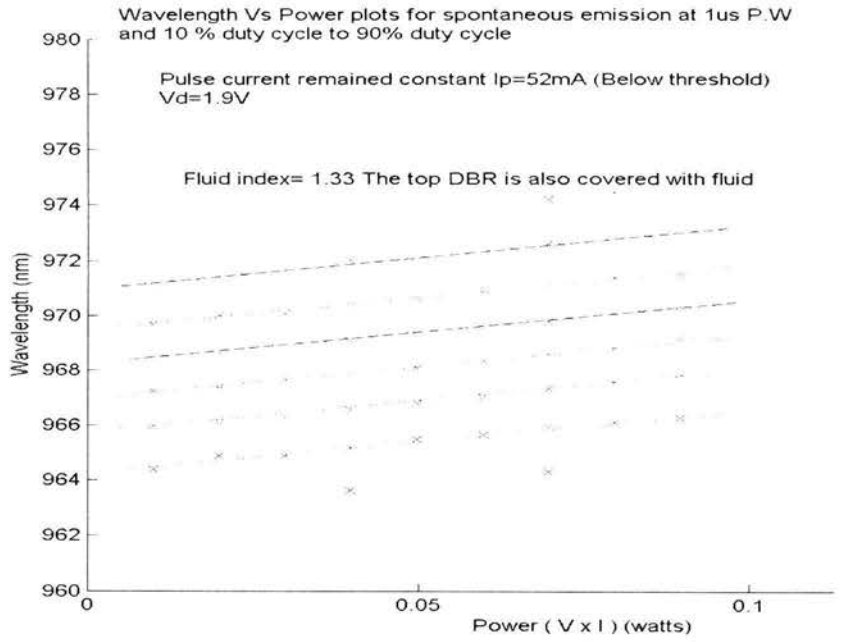

(a)

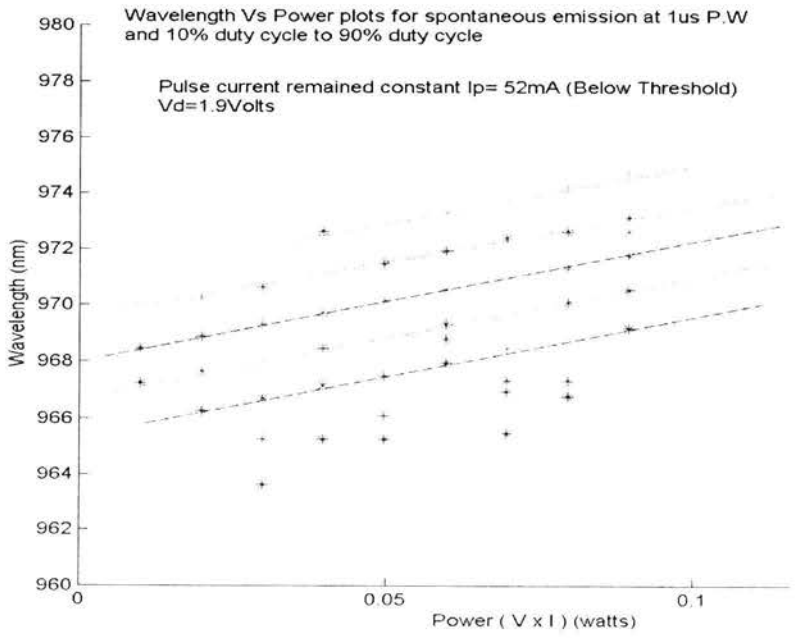

(b)

Figure 6.10 Thermal resistance measurement of a FILD sensor with (a) water inside the fluidic cavity and (b) air inside the fluidic cavity

As already mentioned in Chapter 5, these devices were pulsed at low duty cycles to prevent device heating and thus avoiding heat exchange with fluids. A simple mathematical analysis of the device operating temperature is presented next.

With a maximum-pulsed current of about 150 mA and voltage of approximately 3 V, the input power to the device is approximately 4.5mW at 1 % duty cycle. This corresponds to a device temperature rise of 2.25 °C and 1.13 °C with air and water inside the fluidic cavity respectively. Thus there is a temperature decrease of less than 1 °C of the NECSEL device, when air is replaced by water inside the fluidic cavity. With this negligible change in temperature, it can be considered there are no thermal lensing effects to modulate the transverse confinement of laser beam, and this phenomenon does not dominate under the mentioned operating conditions.

6.2.5 Scattering losses at the substrate and fluidic cavity interface

The antireflection coating at the substrate has a surface roughness of 5 nm to 40nm based on AFM measurements. When the light generated inside the laser diode propagates and passes through this interface, it incurs scattering loss due to the rough surface. This loss is directly proportional to the RMS roughness of the coating. It turns out that this loss is also proportional to the square of refractive index difference between the antireflection

coating and fluidic cavity. With the change in fluid medium from air to water, the refractive index difference at the substrate interface decreases, and thus the scattering losses are modulated by a change in refractive index of the fluidic cavity. The next paragraph explains the scattering loss mechanism in detail. This is followed by a detailed analysis on modulation of effective reflection coefficient and losses of the mirror M_{eff}.

The mechanism of scattering loss is very simple. Let us consider the substrate – fluidic cavity interface, where this phenomenon occurs. Figures 6.11 (a) and (b) show a "zoomed in" version of the substrate interface, with two different levels of surface roughness of the antireflection coating.

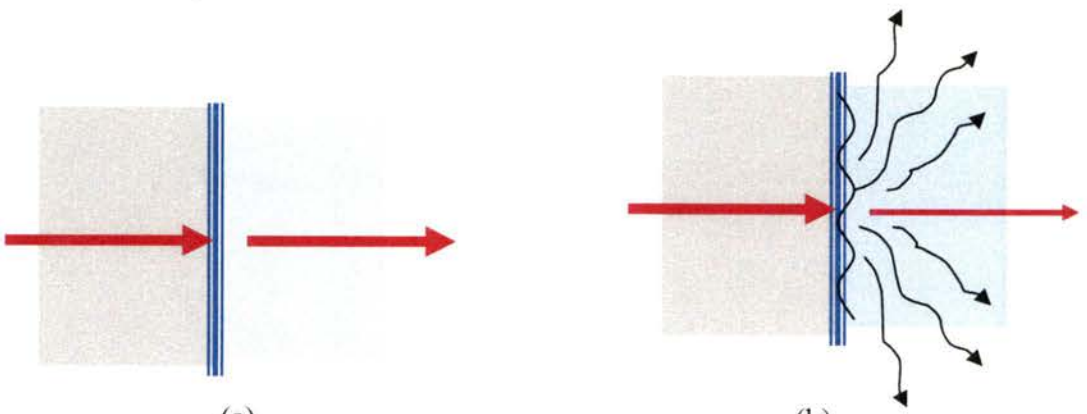

Figure 6.11 Zoomed in version of substrate-fluidic cavity interface with (a) perfectly smooth AR coating and (b) AR coatings with some level of roughness

Figure 6.11 (a) assumes that the AR coating is perfectly smooth and there is no scattering loss associated with it. On the other hand, Figure 6.11 (b) assumes that the AR coating has some level of roughness and thus each time when light passes through this interface, a fraction of it is lost due to surface scattering. While it is intuitive that amount of

scattering loss is a monotonically increasing function of surface roughness, it is difficult to quantify without doing a real experiment on scattering loss measurement. There is yet another method which helps in approximating scattering loss as a function of surface roughness and refractive index difference at the interface. This method is called the "total integrated scattering" method. Total integrated scattering (TIS) is a method, used by researchers to approximate the RMS roughness of a surface, of determining the scatter loss experimentally. In this method, the amount of scattered light is measured in a hemispherical area around the rough surface, as a fraction of incident light [10, 11]. A mathematical model based on this method, relates the scattering loss with the RMS surface roughness and the refractive index difference at the interface [12]. This relation is given as

$$TIS = (2 \pi \sigma \Delta n / \lambda)^2$$

where TIS is the ratio between the amount of light scattered in the forward direction to the incident light, σ is the RMS surface roughness, Δn is the refractive index difference at the interface and λ is the wavelength of the light. Since the RMS surface roughness is already measured on different laser diodes by atomic force microscopy, the total integrated scatter loss can be estimated for different fluid indices at the lasing wavelength.

Now that the surface roughness mechanism is well understood, the modulation of laser threshold and slope efficiency by fluid index is explained next. In order to explain this phenomenon, the "gain and loss model resonator" discussed in Section 6.1.2.1 is considered. The mirror M_{eff} represents the complete passive cavity, and the scattering

losses are embedded in the complex effective reflection coefficient r_{eff}. Appendix E presents transfer matrix calculations in determining the modulation of threshold current and slope efficiency due to change in fluid index at different roughness levels of the AR coating. From the results discussed in the appendix, it can be said the experimental data on the FILD sensors 13-23 with their RMS roughness ranging from 5nm to 40nm do not conform to the theoretically calculated values. Note that the most common trend of experimental data matches with the qualitative analysis of this phenomenon. However, the functionality of a particular sensor still cannot be based on this phenomenon due to the different values of the measured shifts in threshold currents and slope efficiencies of different FILD sensors.

6.3 Summary

This chapter presents qualitative and quantitative analysis of different theoretical phenomena that explain the physics of a FILD sensor. All of these phenomena play an important role in determining the characteristics exhibited by FILD sensors. However, it is extremely difficult to determine which one of them dominates over the others to define the sensor's characteristics. As a result, a complete quantitative mathematical model based on these phenomena could not be constructed because the FILD sensors exhibited different trends of measurements with different values of threshold current and slope efficiency shifts with fluid index. Some theoretical phenomena like "modulation of beam transverse confinement" and "modulation of scatter loss at the fluidic cavity" do match the qualitative trend of most of the FILD sensors. This indicates that these two

phenomena dominate most of the time, but not always. However quantitative analysis of both the above phenomena shows results that are orders of magnitude off the actual measured data.

References:

[1] Larry A.Coldren and Scott W. Corzine, *"Diode Lasers and Photonic Integrated Circuits"*, Wiley Series in Microwave and Optical Engineering, Chapter 3

[2] Larry A.Coldren and Scott W. Corzine, *"Diode Lasers and Photonic Integrated Circuits"*, Wiley Series in Microwave and Optical Engineering, Chapter 2

[3] Anthony E. Siegman, *"Lasers"* Chapter 14, University Science Books, 1986

[4] Young EW, Choquette KD, Chuang SL, et al. *"Single-transverse-mode vertical-cavity lasers under continuous and pulsed operation"*, IEEE Photonics Technology Letters **13 (9),** 927-929 SEP 2001

[5] Ghulam Hasnain, Kuochou Tai, L. Yang, Y. H. Wang, R. J. Fisher, James D. Wynn, Bonnie Weir, Niloy K. Dutta, and Alfred Y. Cho, *"Performance of gain guided surface emitting lasers with semiconductor distributed Bragg reflectors"*, IEEE Journal of Quantum Electronics, **27(6)**, page 1377-1385, June 1991.

[6] M. Brunner, K. Gulden, R. Hovel, and M. Moser, *"Thermal lensing effects in small oxide confined vertical-cavity surface-emitting lasers"*, Applied Physics Letters, Vol **26**, page 7-9, January 2000

[7] Anthony E. Siegman, *"Lasers"* Chapter 20, University Science Books, 1986

[8] Anthony E. Siegman, *"Lasers"* Chapters 14-15, University Science Books, 1986

[9] A. G. Fox and Tingye Li, *"Resonant modes in a maser interferometer"*, The Bell system technical journal, pages 453-488, March 1961

[10] Daniel Ronnow, Mikael Bergkvist, Arne Roos, and C. G. Ribbing, *"Determination of interface roughness by using a spectroscopic total integrated scatter instrument"*, Applied Optics, **32 (19)**, pages 3458-3451, 1993

[11] Karl h. Guenther, Peter G. Wierer, and Jean M. Bennett, *"Surface roughness measurements of low-scatter mirrors and roughness standards"*, Applied Optics, **23 (21)**, pages 3820-3835, 1984

[12] Breault Research Organisation, *"Advanced system analysis program-technical guide for light scattering"*, http://www.breault.com/resources/kbasePDF/brotg0922_scatter.pdf

Chapter 7

Conclusions and future work

This chapter summarizes the work done in this master's thesis on vertical cavity surface emitting laser based fluid intracavity laser diode sensors. As already mentioned in Chapter 1, FILD sensors are a candidate for the platforms for the next generation photonic sensors integrated to micro-total analytical systems (μ-TAS) for performing biological and chemical assays. This chapter presents a summary of the various advantages and limitations of a FILD sensor. It also discusses some future work which can improve the structure and overall performance of a FILD sensor.

7.1 Advantages of a FILD sensor

A FILD sensor takes advantage of the combined capabilities of a microfluidic chip and a micro-laser in an integrated system. A FILD sensor can facilitate applications involving fluorescence excitation, cell spectroscopy, intracavity spectroscopy, cell lysing, optical tweezers etc. It is electrically pumped and thus does not require external lasers for optical pumping. It is portable, less expensive than conventional externally pumped fluorescence based sensor systems and can incorporate other optical elements like photo-detectors and optical filters to enhance its functionality. The construction methods of a FILD sensor are fairly simple and straightforward.

7.2 Limitations of a FILD sensor

As already discussed in Chapters 5 and 6, different FILD sensors constructed by even the same laser diode exhibited different trends of experimental data which do not conform with each other quantitatively. This is the main drawback of a FILD sensor as it leads to an incomplete theoretical analysis of the sensor. Different data points and experimental trends match with different theoretical phenomena discussed in Chapter 6, leading to a greater uncertainty on a sensor's response to a change in fluid index. In an ideal world, a user should be able to determine the change in refractive index of fluid inside the fluid cavity by interpreting information on threshold current and slope efficiency shift. But, if the sensor exhibits different trends of measurements, even though they are repeatable, it will lead to confusion for the user to rely on a particular theoretical phenomenon to interpret the results. Another limitation of a FILD sensor is its non-linear and unpredictable spectral response to a non-homogeneous or even homogeneous fluid index change. As discussed in detail in Appendix B, fluid index change induces mode hopping, which is an unpredictable phenomenon as it is related to operating temperature also. On the other hand, Dr.Gourley's biocavity laser would exhibit a linear spectral response to a change in fluid index due to the simplicity of a two-mirror resonator. Lastly, as compared to a biocavity laser, the FILD sensor has a relatively long external cavity, which leads to smaller mode spacing that might not be large enough to resolve all the higher order modes of a biological cell. The sub-sections discusse some of those uncontrolled parameters, which are assumed to be responsible for different trends of measurements exhibited by FILD sensors.

7.2.1 Tilt of laser diode

During the construction of a FILD sensor, it is important that a NECSEL diode is parallel to the external mirror. The process of constructing a fluidic sealed cavity between the diode and the external mirror involves reflowing of patterned photoresist. There is a possibility that if the photoresist is not uniformly coated on an external mirror then its reflow will also be non-uniform, leading to an induced tilt of the NECSEL diode with respect to the dielectric mirror. While spinning of photoresist AZ 5440 above 3000 rpm does produce a uniform coating on a substrate, multiple spins on the same substrate may result in non-uniformity of photoresist. Multiple spins were performed to achieve thicker micofluidic channels. It is thus critical to measure the parallelism of a NECSEL diode with the external mirror before a FILD sensor is characterized. Laser resonators with tilted mirrors may result in an unstable operation or increased threshold currents to compensate for higher losses. It is important that an accurate method of NECSEL tilt measurement is devised, because even a tilt of 1 degree can cause significant modulation of laser characteristics. The quantitative analysis of laser diode's tilt on the threshold current and slope efficiency is beyond the scope of this thesis work.Or, on the other hand, another method of fluidic cavity sealing can be devised, which is less prone to device tilt with respect to the external mirror. Such a method would not employ photoresist or any other soft polymers to construct a gasket between the device and external mirror. A possible way to achieve a non-tilted cavity sealing process is to get dielectric mirror coatings on glass substrates with already etched fluidic channels. Laser diodes (like NECSELs) can then be aligned over the fluidic channels and glued to the substrate.

7.2.2 Surface roughness of dielectric mirror and laser substrate

As discussed in Chapter 6, the surface roughness on the substrate of a NECSEL diode is associated with scattering losses, which in turn affects laser's threshold current and slope efficiency. Surface roughnesses of the external mirror or laser substrate are uncontrolled parameters as they might change after continuous use of FILD sensors. It is thus necessary that surface roughness measurements on both external mirror and laser substrate must be performed each time before a FILD sensor is constructed. In this thesis work, surface roughness measurements were not performed until the particular theoretical phenomenon was considered to explain experimental data.

7.2.3 Aging of device and device handling

The NECSEL device is a 1mm x 1mm x 80μm chip, which is very fragile and difficult to handle without special vacuum tweezers. Handling of these devices with general lab tweezers and aligning their apertures over patterned microfluidic channels may result in device degradation. Also these devices are subjected to physical contacts with different fluids and chemicals like water, oil, acetone, methanol and photoresist, which might also be a reason for early aging of these devices. While all the above factors are uncontrollable, still they might not be the only ones responsible for different trends of measurements on these devices.

7.2.4 Experimental errors

Experimental error like improper alignment of the photodiode with the FILD sensor may result in exhibition of different slope efficiencies by the sensor. It is thus important that a

photodiode must always be properly aligned with the sensor to ensure accurate measurements. Some other common experimental errors that may result in incorrect measurements of injection current could be incorrect settings on the Labview program for L-I measurement control or impedance mismatch induced oscillations on the current pulse.

7.3 Future work proposed

Despite all the above limitations, FILD sensor still serve as a basic platform for photonic lab-on-a-chip type systems. This section proposes some future work that can be implemented on FILD sensors to improve their overall design and performance.

7.3.1 Better understanding of the physics of a FILD sensor

Chapter 6 presented different phenomena, which qualitatively matches with different trends of experimental measurements. However, it is still unclear, if there is only one phenomenon dominant on a particular sensor, or there is a combined effect of different phenomena to produce different results. There is a need to construct a mathematical model that combines the effects of all the phenomena discussed in Chapter 6 and then analyze the characteristics of different sensors. In order to implement this, more data points on different FILD sensors are required. It is also important that all the physical and optical characteristics of the diodes must be thoroughly studied, before these devices are characterized.

7.3.2 Integration with silicon technology

A FILD sensor can be integrated to a silicon photo-detector. This can be achieved by re-designing the dielectric mirror coatings on a silicon photodiode, instead of glass substrate. The key idea here is to make a lab-on-a-chip type system that is intelligent enough to detect the presence of a biological cell, and does not require bulky optical spectrum analyzers for doing the analysis. This can be achieved by first characterizing a FILD sensor spectral response to a biological cell using a spectrum analyzer, and then integrating it to a photo-diode. This photodiode would have special optical filter coatings that are designed to allow only certain wavelengths to be absorbed by the photodiode. In this way, if the optical filter coatings are designed for only those wavelengths that are modulated most by a biological cell perturbation, then the system can detect the presence of a cell by measuring the variations in photocurrent from the photodiode.

7.3.3 Top emitting VCSEL based extended fluidic cavity sensor

Chapters 4 and 5 already discussed the fabrication steps of a top emitting VCSEL based extended fluidic cavity sensor. Although the top emitting VCSELs used for fabricating the sensor systems were not suitable for extended cavity applications, the sensor fabrication techniques would be the same for an ideal top emitting VCSEL based sensor system suitable for extended cavity applications. Appendix B presents a mode shift analysis of such sensor system and compares it with that of the FILD sensor presented in thesis report. Due to larger mode spacing as compared to that of a FILD sensor system, a top emitting VCSEL based sensor system will exhibit greater sensitivity of wavelength shifts to change in fluid index.

7.4 Summary

This chapter presents a brief conclusion to the work done on FILD sensors, by presenting their advantages and limiting factors. It also discusses briefly some future work, which can eliminate the requirements of bulky spectrum analyzers and still be able to act as biological cell sensors.

Appendix A

Labview-automated pulsed L-I measurements of a laser diode

This appendix provides details about the Labview program "Pulsed LI characteristics", which was written in order to automate measurements of L-I characteristics of a laser diode under pulsed operation. The testing of FILD sensors required L-I measurements under low duty cycle (< 1%) to prevent any thermal effects on the sensors' characteristics. In order to fulfill this requirement, a Labview code was written, the functionality of which is explained in great detail in this appendix.

Ideally, pulsed L-I measurements of laser based devices require a "current pulse generator", which has infinite output impedance and can output current pulses of known pulse widths and currents, at different frequencies. At the same time, a photodiode is required to convert optical power into photocurrent, and a meter is needed to measure the photocurrent. Thus in an ideal case, a current pulse generator and a power meter must be connected to a computer in an automation environment like Labview, to control an L-I measurement process. Unfortunately, due to the unavailability of a current pulse generator, a voltage pulse generator was used instead to supply known current pulses to a laser diode. This required another piece of equipment, an oscilloscope, to be connected in the automation environment to control L-I measurements in order to measure the magnitude of the current during the voltage pulse. Figure A.1 shows the block diagram of the control circuit.

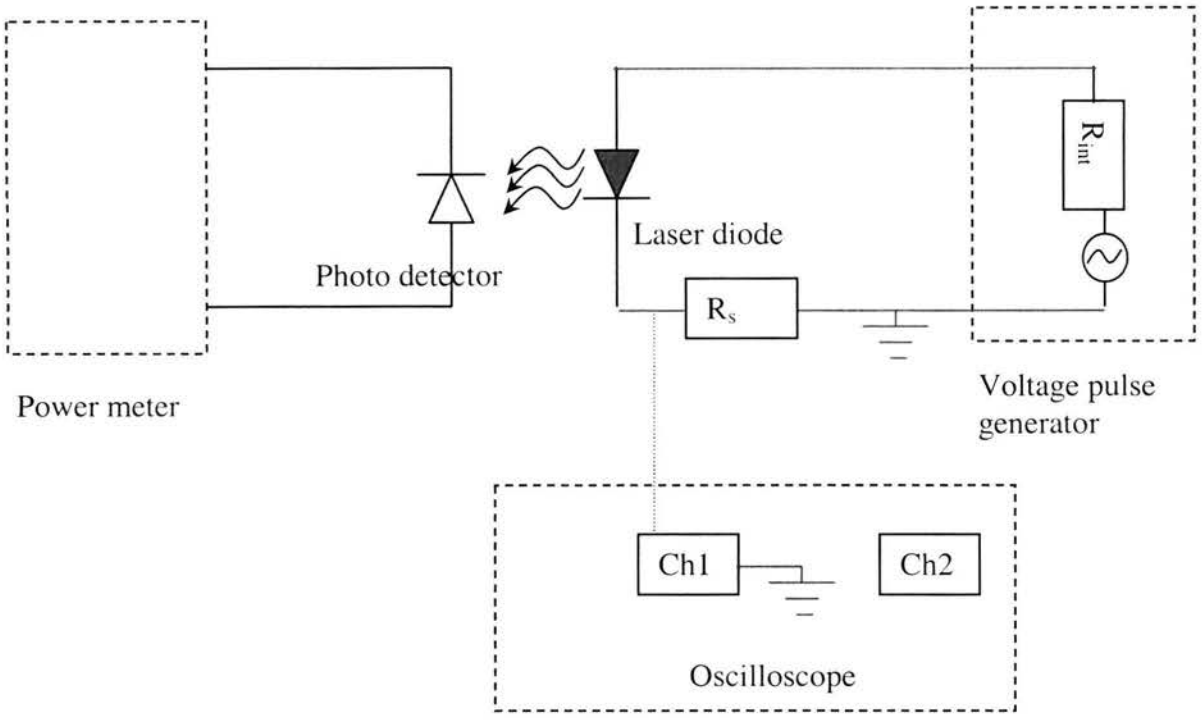

Figure A.1 Block diagram of the control circuit of pulsed LI measurement setup

Control circuit description

The control circuit consists of a voltage pulse generator (HP 8611A), an oscilloscope (HP 54501A), and a power meter (Keithely 2400 source/meter). All the above equipments are connected via GPIB ports to a computer to run the automation environment. A GPIB (General Purpose Interface Bus) port supports the IEEE-488 bus standard, which was developed to connect and control programmable instruments, and to provide a standard interface for communication between instruments from different sources. Hewlett-Packard originally developed the interfacing technique, and that is why it is also called HP-IB. The controlling computer needs to have a GPIB compatible network card in order

to hold the automation environment. The model number of the GPIB interface card used here is AT-GPIB/TNT (plug and play). This interface card is a high-performance IEEE 488 interface for PCs with ISA slots. (The picture of an ISA slot on a motherboard is shown in Figure A.2). The AT-GPIB/TNT can sustain data transfer rates greater than 1.5 Mbytes/s using the IEEE 488.1 3-wire handshake. The AT-GPIB/TNT also implements the high-speed GPIB protocol (HS488) and is compatible with Windows Me/98/95 operating systems only.

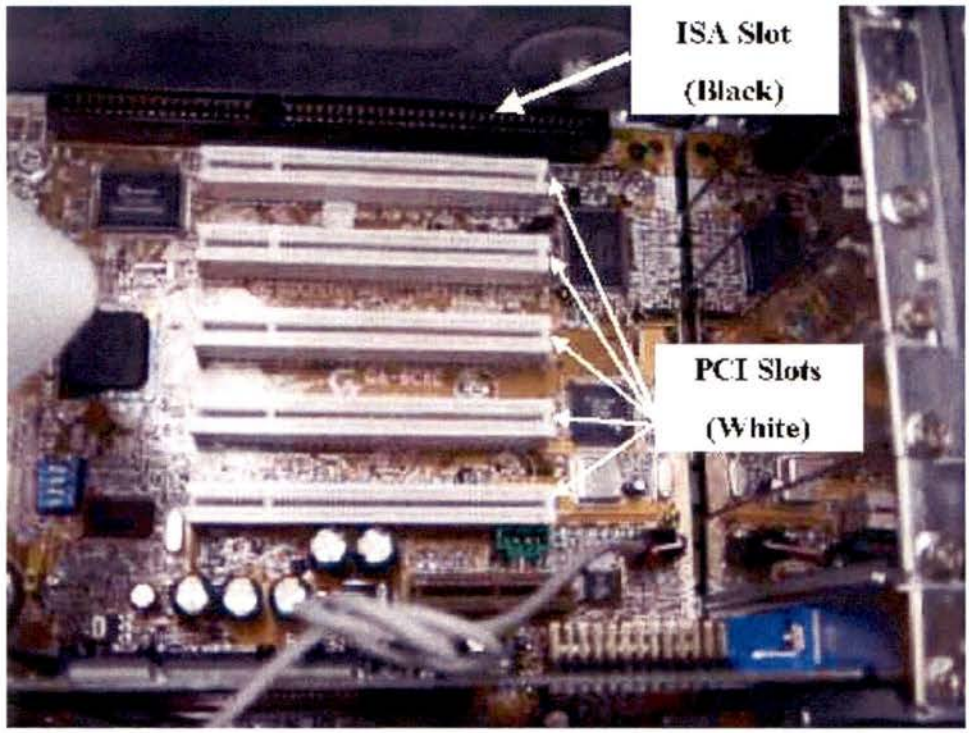

Figure A.2 Picture of a motherboard showing and ISA slot and four PCI slots. (Reproduced from Reference [1])

There are three versions of the AT-GPIB/TNT - the AT-GPIB/TNT (Plug and Play), which features a jumperless configuration; the legacy AT-GPIB/TNT, which uses DIP

switches and jumpers to configure the interface; and the AT-GPIB/TNT+, which is a combination of an AT-GPIB/TNT (Plug and Play) and a GPIB analyzer in one board. All three interfaces contain identical GPIB interface functionality. More information on different types of GPIB interface cards can be obtained from Reference [2].

The voltage pulse generator supplies known voltage pulses to a circuit containing the laser diode and a known resistance connected in series. The oscilloscope probe is connected across the series resistance to determine the current through the series circuit. The power meter measures the photocurrent from a photodiode, which is aligned to the laser diode. The photodetector used here is a silicon PIN photodiode, part number PDBC 618 bought from Photonic Detectors Inc [3]. It is a wide area detector (371.1mm^2) and has a response time of 200ns with a load resistance of 1kΩ at a reverse bias of 5V. It is used under zero reverse bias conditions. The Keithley 2400 source/meter is not synchronized with the voltage pulse generator to measure the peak photocurrent from the detector. Hence it measures the average photocurrent over several current pulses to the laser diode. Thus in order to determine the actual peak photocurrent value (proportional to the laser output), the measured average current data is divided by the duty cycle of the voltage pulse. The Labview automation program controls the complete L-I measurement by communicating with all the equipment. The next couple of paragraphs discuss the two graphical user interfaces of the Labview program.

Labview GUI

Labview has two graphical user interfaces. They are called the "block diagram window" and the "control window". The block diagram window shows all the controls which are set by the user to run a Labview program. It may also contain some indicators in the form of graphs, Boolean displays or even numeric values, to inform the user about the status of certain variables. Figure A.3 shows the block diagram window of the "Pulsed L-I characteristics" Labview program. It consists of different controls including pulse parameters, oscilloscope parameters, time delay parameters, and voltage sweep parameters. All these parameters are set by the user depending upon the type to L-I measurement to be taken on a particular laser diode. The user also inputs the GPIB address of specific pieces of equipment so that the program can communicate with that equipment.

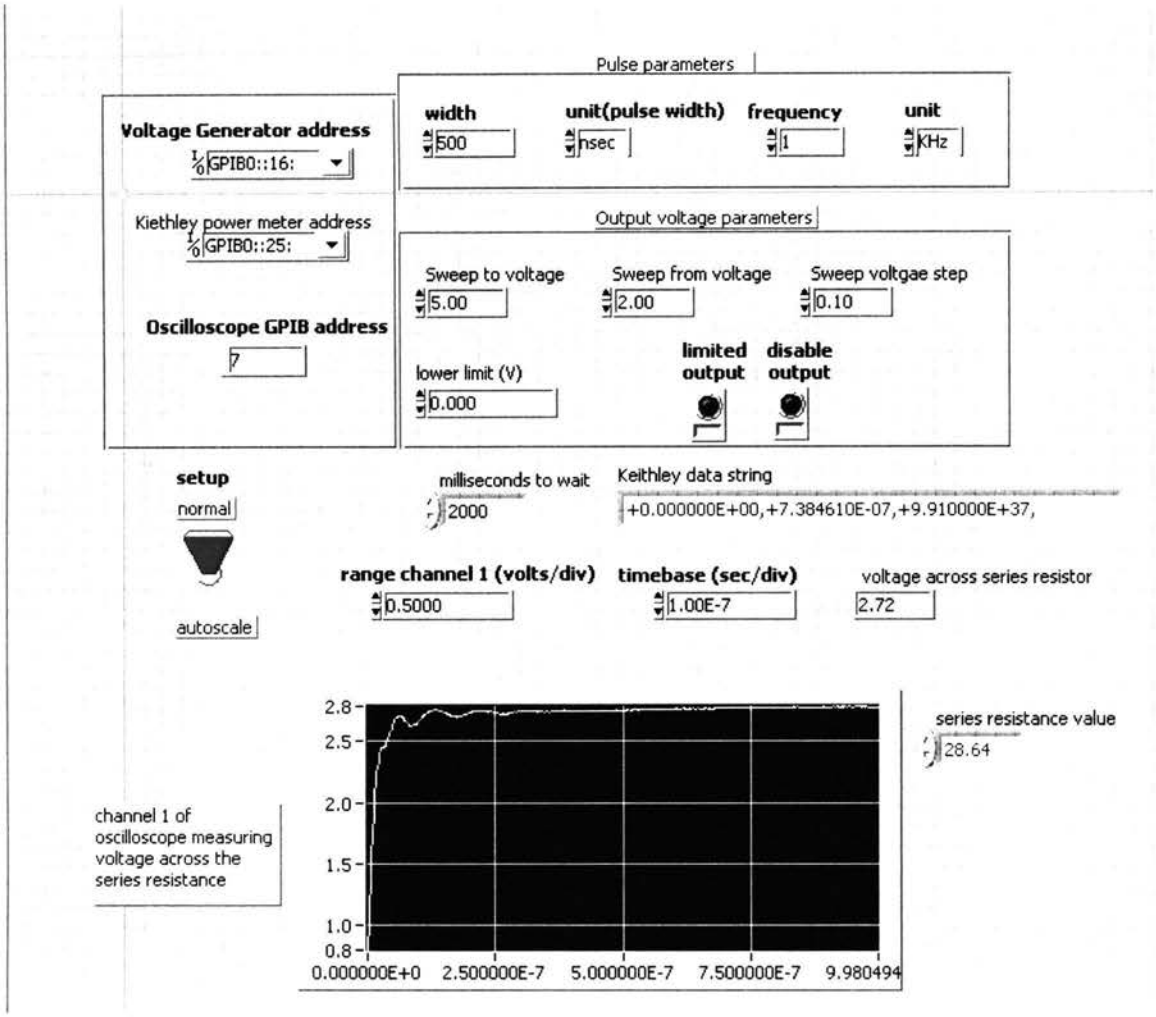

Figure A.3 Block diagram window or front panel of the 'Pulsed LI characteristics' Labview program

The control window of a Labview program, on the other hand shows the physical connection between different instruments in the automation environment. The control window defines the whole structure of the Labview program by holding all the logical, mathematical and iterative operations. Unlike other programming languages, where these methods are represented by suitable programming codes, Labview has special symbols

and prototype "wires" to graphically represent the logical/mathematical operations and data flow. Figure A.4 shows the control window of the pulsed current driver program.

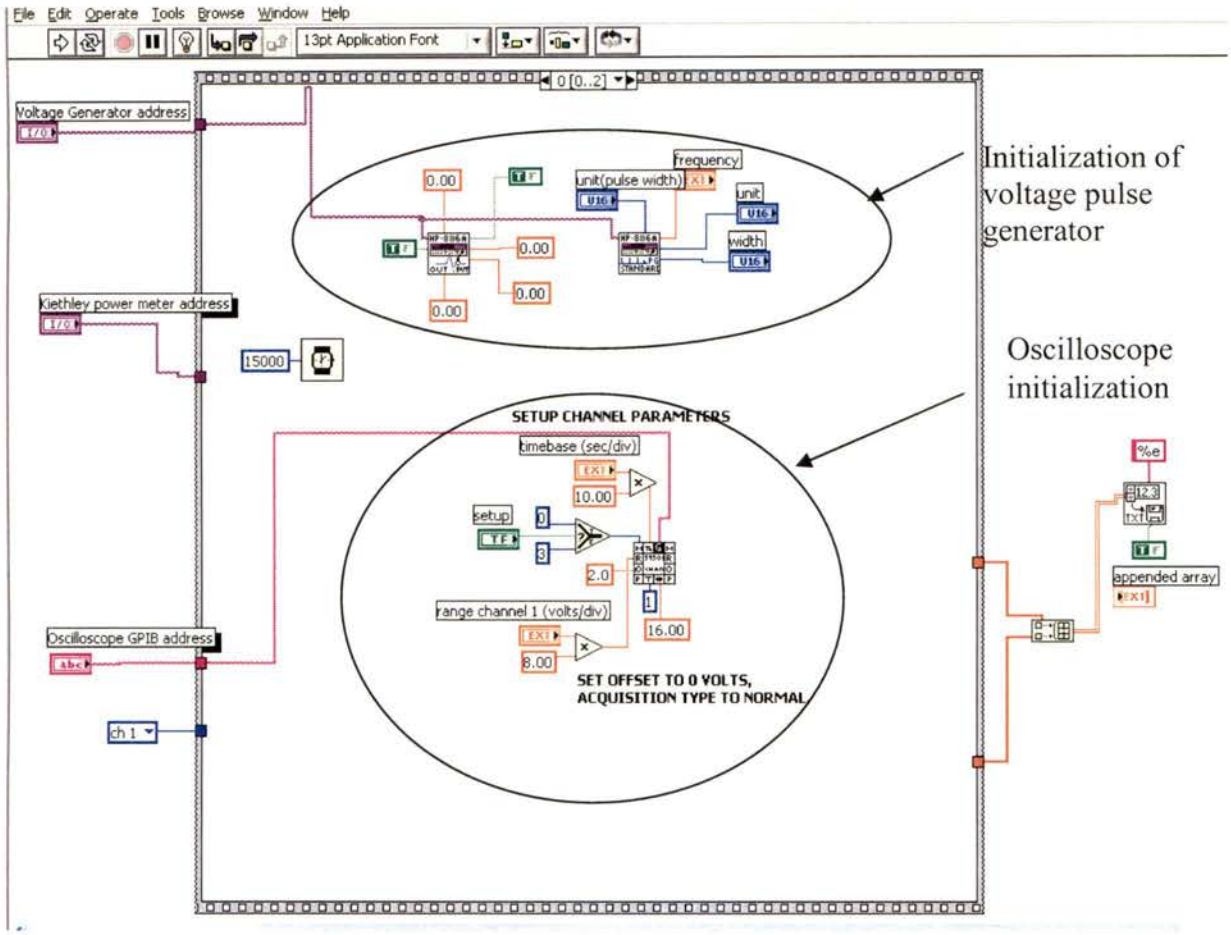

Figure A.4 Instrument initialization code on the control window

Figure A.4 shows a rectangular block, with an index "0 [0..2]". This block represents a sequence, which has three frames. The indices of the frames are 0, 1 and 2, and the one shown on the figure is the 0^{th} frame. A frame in Labview programming can be compared to a set of programming codes or statements in any conventional programming language.

In this Labview program, three different frames are constructed and are sequenced so that three different sets of programming instructions are executed in a sequence. The frame shown in Figure A.3 is the initialization frame. It consists of programming instructions which initializes the voltage pulse generator and the oscilloscope for L-I measurements. The initialization parameters for the voltage pulse generator include pulse width, frequency, and starting and ending values of sweep voltages. The values of these parameters are input by the user on the front panel or the "block diagram window" of the program. Similarly the initialization parameters for the oscilloscope are voltage and time ranges, and auto-scaling. There are other parameters like averaging factor of oscilloscope scans, offset voltages etc, which are not shown on the block diagram, but are initialized by default values on the "control panel window". The power meter is not as complicated as voltage pulse generator and oscilloscope are, so it does not need to be initialized.

After initialization, the pulsed current driver program controls the three equipments by sending them appropriate commands. Figure A.5 shows the control window with the second frame of sequence. The second frame with index (1 [0..2]) consists of another rectangular block, which represents a "while loop". A "while loop" is an interative method, which executes a set of statements or programming code until some logical condition is satisfied. This loop consists of certain commands to the voltage pulse generator, oscilloscope and to the power meter. These commands are outputting certain voltage pulse to the laser circuit, measure voltage across the series resistance on oscilloscope and to measure the photocurrent respectively. Since these commands need to be executed repeatedly until the voltage is swept from starting value to the desired end

values, they are executed in a loop. After each execution of these statements, a counter variable is incremented, and the logical condition is checked. In the case of the Pulsed LI

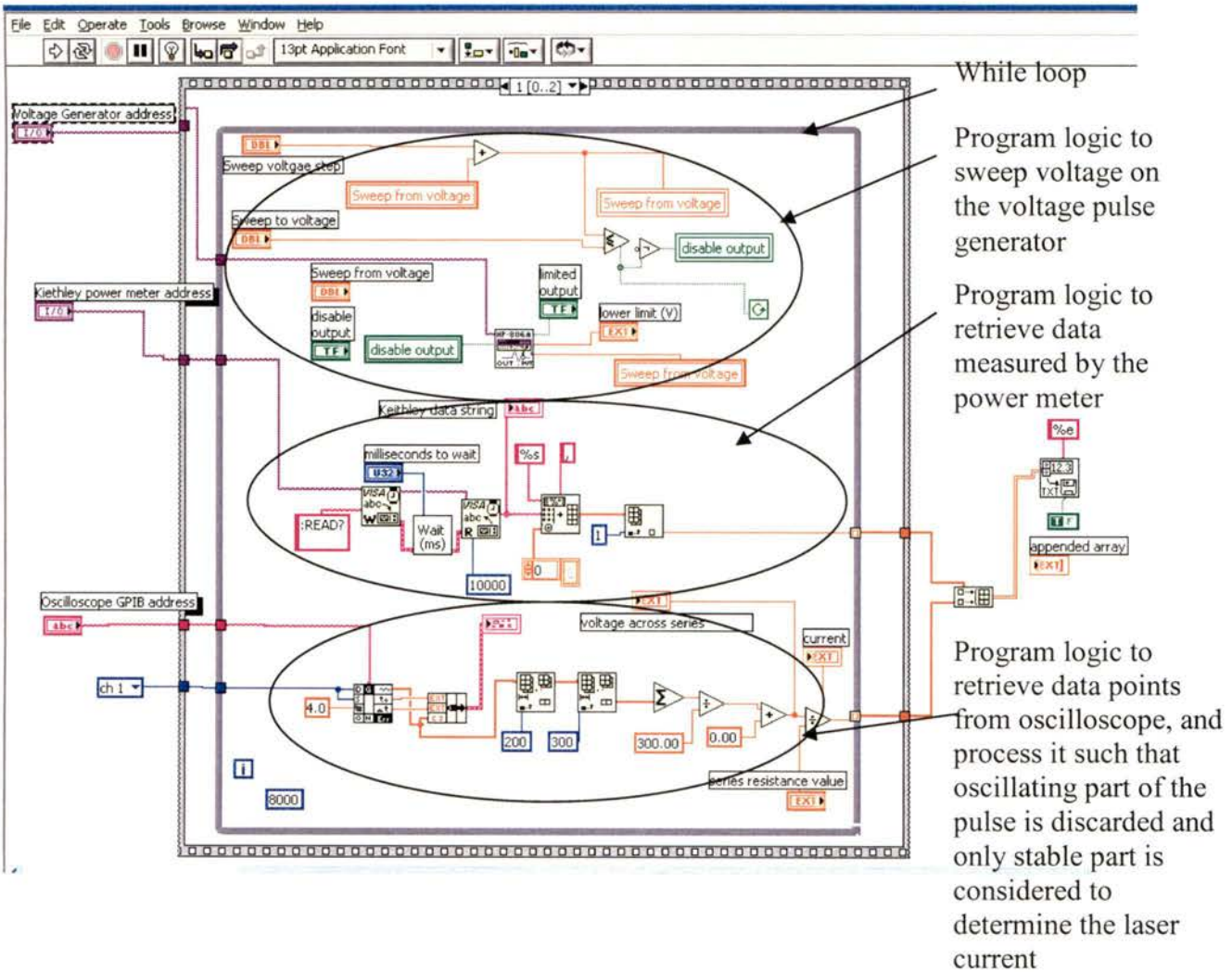

Figure A.5 Second frame of the Pulsed LI characteristics Labview program showing set of programming instructions being executed in a 'while loop'

characteristics program, the logical condition is whether the voltage generator output voltage is equal to the "stop-voltage" set by the user. As soon as the condition is met, the program control comes out of the loop and proceeds to the next frame.

Figure A.5 also shows certain mathematical operations with the data measured by the oscilloscope. These operations perform the "pulse cleaning" of the voltage pulse measured by the oscillator to determine accurate value of the circuit current. As can be seen in Figure A.6 (also shown in Figure A.2), the shape of the voltage pulse across the series resistance is not perfectly rectangular. Figure A.6 shows a 1μs long pulse with oscillations in the first 200ns.

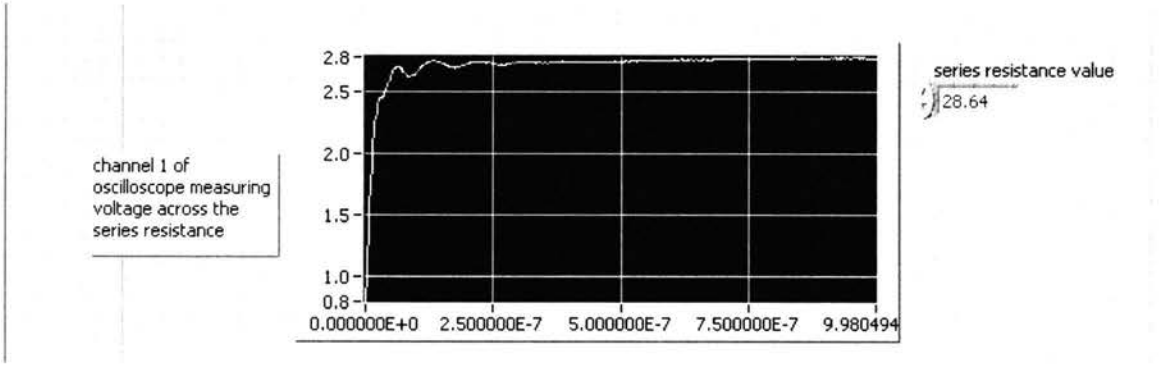

Figure A.6 A part of front panel showing oscilloscope measurement

These oscillations are due to imperfect impedance matching between the voltage pulse generator and the laser circuit. The voltage pulse generator has an output impedance of 50Ω and in order to prevent any circuit oscillations the output circuit, which is also the laser circuit must also have an impedance of 50Ω. The series resistance 28.64Ω is chosen in such a way that the equivalent circuit impedance is close to 50Ω. The circuit current is

determined by dividing the measured voltage by the series resistance value. It is thus important that measured voltage value must be determined by averaging over stable and non-oscillating part of the voltage pulse. This is achieved by temporarily storing all the data points across the pulse in an array (512 points), and then discarding the first 200 points, which contains the oscillating part of the pulse, and taking average over rest of the data points.

The third and the last frame of the program is shown in the Figure A. 7. In this frame, instructions are given to the voltage pulse generator to shut off the voltage supply. At the end of execution of this frame, the program control processes the data measured in the previous frame and prompts the user to save the data file on the computer.

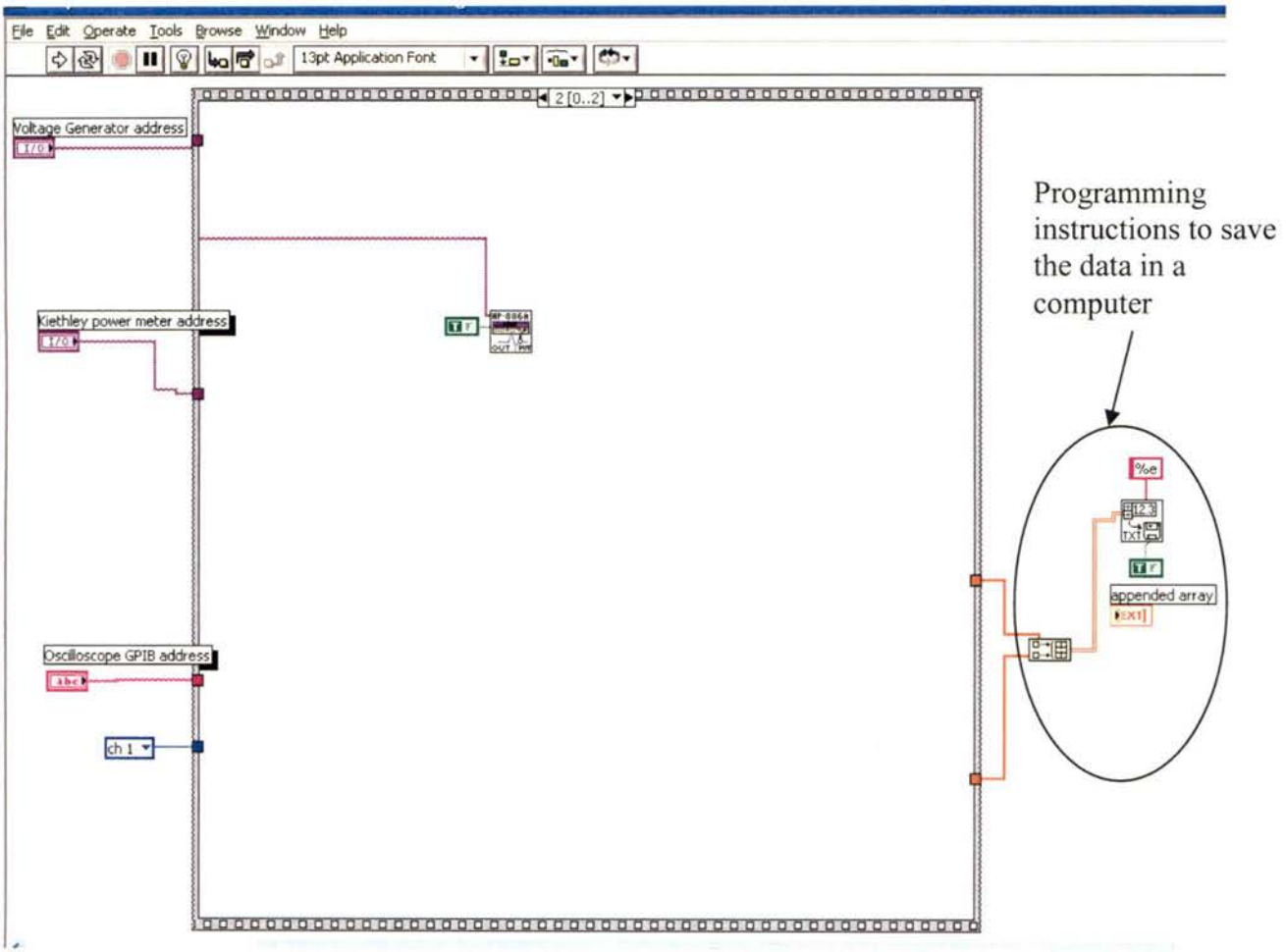

Figure A.7 Last frame of the Pulsed LI characteristics Labview program showing 'disable output' instructions being given to the voltage pulse generator

References:

[1] http://www.st-andrews.ac.uk/its/resnet/equipment.shtml

[2] http://www.ni.com/gpib/

[3] http://www.photonicdetectors.com/pdf/pdbc618.pdf

Appendix B
Mode shift anaysis of a vertical extended cavity surface emitting laser with an internal DBR

This appendix is a MathCAD sheet which calculates the modes of a vertical extended cavity surface emitting laser by determining the round trip phase of the laser resonator. This analysis is done in order to present a comparison with the mode shifts observed with the FILD sensor, shown in Figure 5.8(a). The author greatly acknowledge the help and the guidance provided by Dr. Lear in presenting these calculations.

The FILD sensor resonator is shown in Figure B.1.

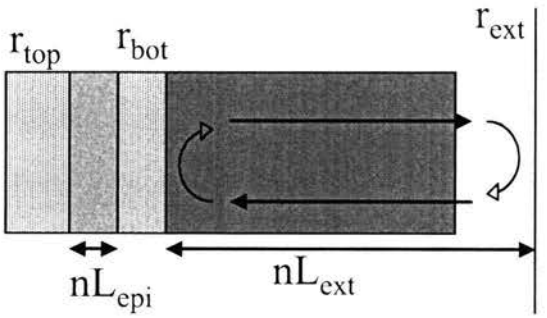

Consider a coupled-cavity resonator where one cavity is very short, such as an epitaxial cavity of a NECSEL, and the other cavity is much longer, such as the external cavity of the FILD sensor. Let the outside mirror on the epitaxial end of the cavity be called the top mirror, and the intermediate mirror be called the bottom mirror, and the external mirror be called 'external mirror'.

The resonant freespace wavelength of the epitaxial cavit $\lambda_r := 972 \cdot 10^{-9} \cdot m$

and the corresponding wavevector: $k_r := \frac{2 \cdot \pi}{\lambda_r}$

$nL_{ext} := 3.5 \cdot 75 \cdot 10^{-6} \cdot m$ The external cavity's optical length

$nL_{epi} := \lambda_r$

The optical length of the internal cavity is generally equal to an integral multiple of resonant freespace wavelength.

$r_{top} := \sqrt{0.999}$ The field reflection coefficient of the top mirror

$g_{epi} := \sqrt{1.02}$ This is the roundtrip gain of the epitaxial cavity (not in /cm, but just as a simple ratio of the output field over the input field.

$r_{bot} := \sqrt{0.8}$ The field reflection coefficient of the bottom mirror

Viewed from the external cavity, the field reflection coefficient of the epitaxial cavity can easliy calculated by using transfer matrix method, which gives

$$r_{epi}(k_0) := \frac{-r_{bot} + r_{top} \cdot g_{epi} \cdot \exp\left[i \cdot (k_0 - k_r) \cdot 2 \cdot nL_{epi}\right]}{1 - \left[r_{bot} \cdot r_{top} \cdot g_{epi} \cdot \exp\left[i \cdot (k_0 - k_r) \cdot 2 \cdot nL_{epi}\right]\right]}$$

where k_0 is the wavevector in space and $k_0 - k_r$ is the detuning factor.

Simplifying the calculations

$\phi(k_0) := (k_0 - k_r) \cdot 2 \cdot nL_{epi}$ $r_{top\_g} := r_{top} \cdot g_{epi}$

Using these simplifications,

$$r_{epi}(\phi) := \frac{-r_{bot} + r_{top\_g} \cdot \exp(i \cdot \phi)}{1 - \left[r_{bot} \cdot \left(r_{top\_g} \cdot \exp(i \cdot \phi)\right)\right]}$$

The phase of the reflection coefficient of the epitaxial structure can be plotted as a functio of detuing factor,

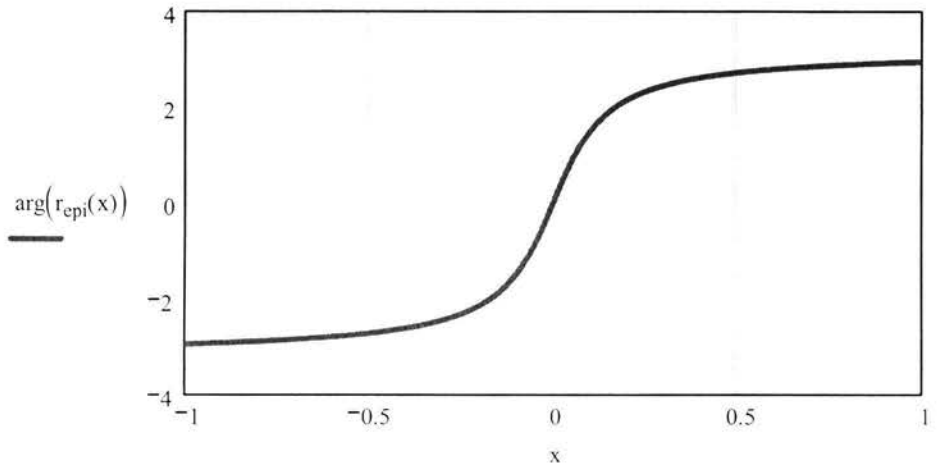

Now if we write the roundtrip phase for the external cavity we get:

$\theta_{RT}(k_0, nL_{ext}) := k_0 \cdot 2 \cdot nL_{ext} + \arg(r_{epi}(\phi(k_0)))$

The corresponding optical lengths of the external cavity with air and water are

$nL_{air} := 3.5 \cdot (75 \cdot 10^{-6} \cdot m) + 1 \cdot (10 \cdot 10^{-6} \cdot m)$

$nL_{water} := 3.5 \cdot (75 \cdot 10^{-6} \cdot m) + 1.33 \cdot (10 \cdot 10^{-6} \cdot m)$

the roundtrip phase must be equal to an integral multiple of 2π, thus plotting the mode number as a function of wavelength,

$a(x) := 970.5 \cdot 10^{-9} m \qquad b(x) := 973.5 \cdot 10^{-9} m \qquad x := 500, 501 .. 700$

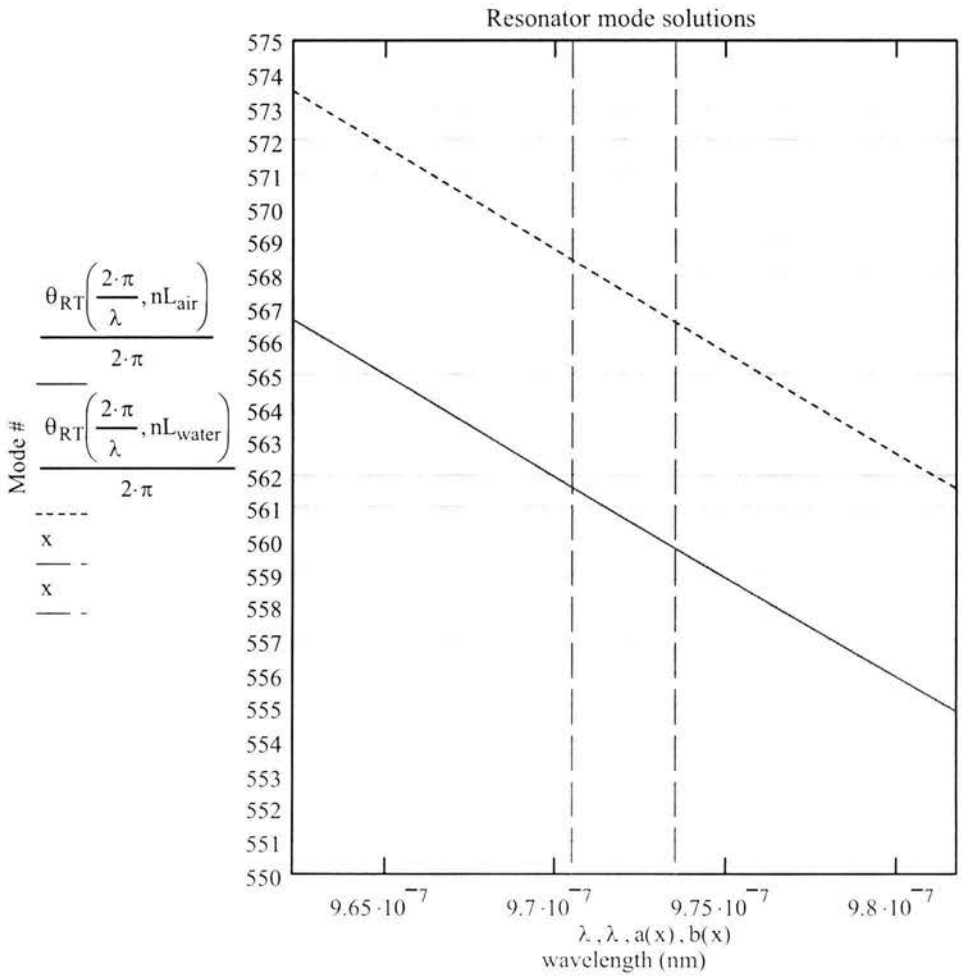

The intersections of the green grid lines and curves are the allowed mode solutions. It can be seen from the above plots that a single mode would shift by about ~10 nm with the fluid perturbation, but since, the linewidth of the laser diode (~3nm) is less than 10 nm, it will result in mode hopping withing the linewidth. On the above plot, the dashed brown lines show the boundaries of the laser linewidth. Within the linewidth, there are 2 modal solutions for each of the two fluidic conditions.

Thus in other words, perturbation of the fluidic cavity would result in mode hopping rather than shifting of a single longitudinal mode. Ideally, for refractive index sensing purposes, the shift of a single longitudinal mode would be easier to relate to the sensor sensitivity. However, due mode hopping, even though the phenomenon is well understood, it is difficult to determine the mode number.

Top emitting VCSEL based sensor

The top emitting VCSEL based sensor would show different resutls due to a smaller external cavity length. Following parameters are assumed for prototype top emitting VCSEL based sensor:

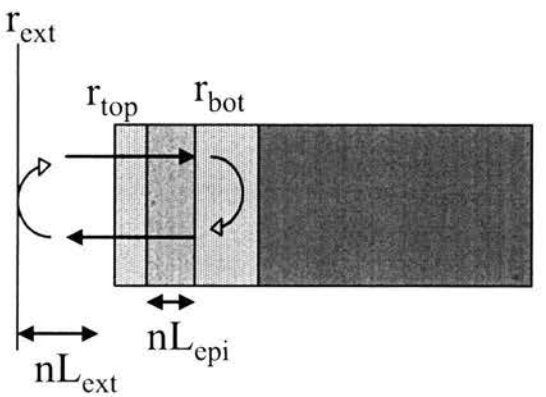

The resonant freespace wavelength of the epitaxial cavit $\lambda_r := 850 \cdot 10^{-9} \cdot m$

and the corresponding wavevector: $k_r := \frac{2 \cdot \pi}{\lambda_r}$

$nL_{epi} := \lambda_r$ The optical length of the internal cavity is generally equal to an integral multiple of resonant freespace wavelength.

$r_{bot} := \sqrt{0.999}$ The field reflection coefficient of the bottom mirror

$g_{epi} := \sqrt{1.02}$ This is the roundtrip gain of the epitaxial cavity (not in /cm, but just as a simple ratio of the output field over the input field.

$r_{top} := \sqrt{0.8}$ The field reflection coefficient of the top mirror

Viewed from the external cavity, the field reflection coefficient of the epitaxial cavity can easliy calculated by using transfer matrix method, which gives

$$r_{epi}(k_0) := \frac{-r_{top} + r_{bot} \cdot g_{epi} \cdot \exp\left[i \cdot (k_0 - k_r) \cdot 2 \cdot nL_{epi}\right]}{1 - \left[r_{bot} \cdot r_{top} \cdot g_{epi} \cdot \exp\left[i \cdot (k_0 - k_r) \cdot 2 \cdot nL_{epi}\right]\right]}$$

where k_0 is the wavevector in space and $k_0 - k_r$ is the detuning factor.

Simplifying the calculations

$\phi(k_0) := (k_0 - k_r) \cdot 2 \cdot nL_{epi}$ $r_{bot\_g} := r_{bot} \cdot g_{epi}$

Using these simplifications,

$$r_{epi}(\phi) := \frac{-r_{top} + r_{bot\_g} \cdot \exp(i \cdot \phi)}{1 - \left[r_{top} \cdot (r_{bot\_g} \cdot \exp(i \cdot \phi))\right]}$$

The phase of the reflection coefficient of the epitaxial structure can be plotted as a function of detuing factor,

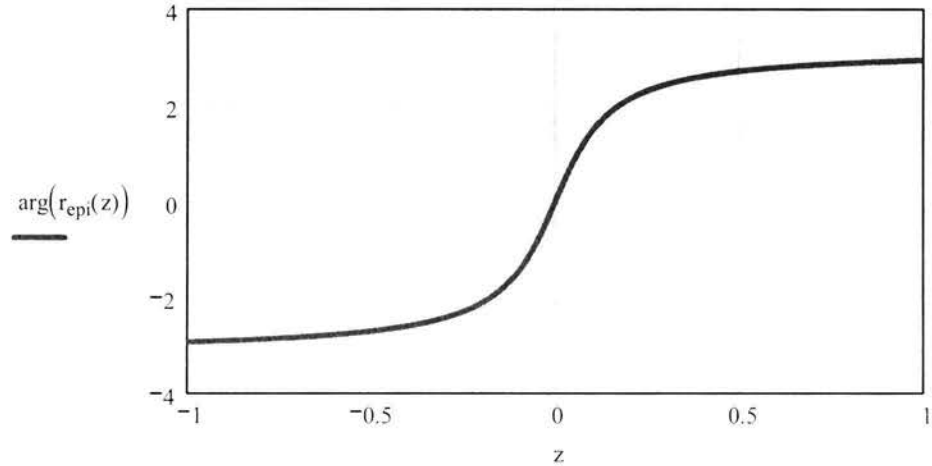

Now if we write the roundtrip phase for the external cavity we get:

$\theta_{RT}(k_0, nL_{ext}) := k_0 \cdot 2 \cdot nL_{ext} + \arg(r_{epi}(\phi(k_0)))$

The corresponding opitcal lengths of the external cavity with air and water are

$nL_{air} := 1 \cdot (10 \cdot 10^{-6} \cdot m)$

$nL_{water} := 1.33 \cdot (10 \cdot 10^{-6} \cdot m)$

the roundtrip phase must be equal to an integral multiple of 2π, thus plotting the mode number as a function of wavelength,

$a(x) := 847 \cdot 10^{-9} m \qquad b(x) := 853 \cdot 10^{-9} m$

$x := -50, -49 .. 100$

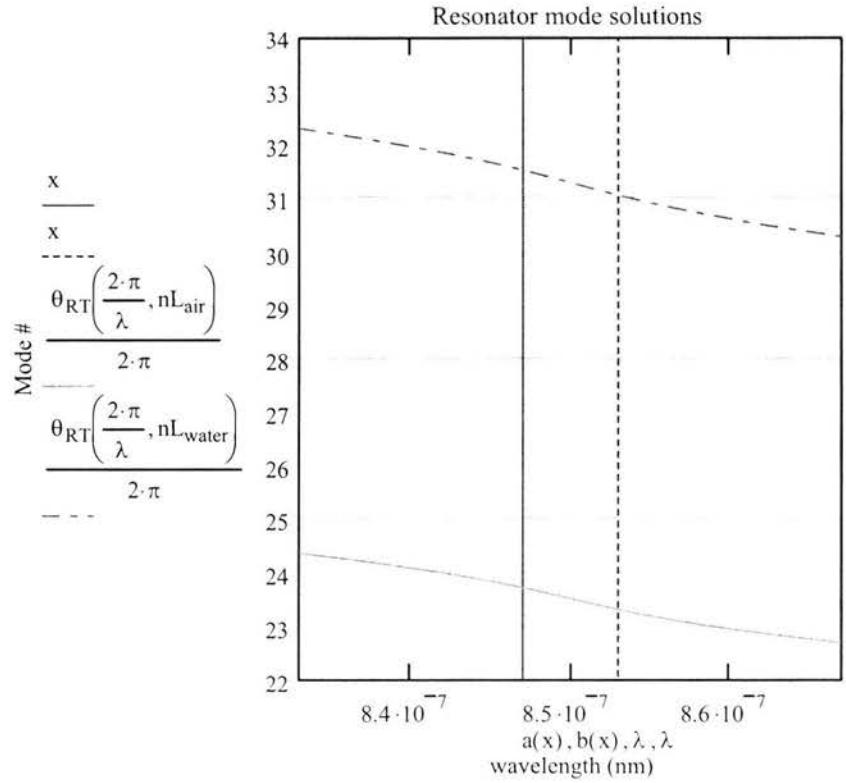

From the above plots, it can be seen that the mode spacing is much larger as compared to those in a FILD sensor. Even though, there is still some mode hopping, but the sensor's wavelength spectrum is comparatively more sensitive to fluid index change.

Appendix C
Calculation of effective reflection coefficient using transfer matrix method

This appendix is a MathCAD sheet which presents basic calculations to determine the effective reflection coefficient of the complete passive cavity region of a FILD sensor.

As already discussed in Section 6.2.1, the passive cavity portion of a FILD sensor consists of the substrate length, AR coatings, and fluidic cavity region as propagation media, and four dielectric interfaces including external mirror r_{ext}, bottom DBR r_2 and two AR interfaces.

It is extremely useful to lump all these passive dielectric elements into one effective mirror, which can be used in other calculations. This technique not only simplifies the resonator model, but also helps in developing a better understanding of a coupled cavity resonator.

This MathCAD sheet starts with a description of the passive cavity region of a FILD sensor resonator. This is followed by definition of transfer matrices of each of the dielectric elements of the passive cavity.

The passive cavity region of a FILD sensor resonator is shown in Figure C.1.

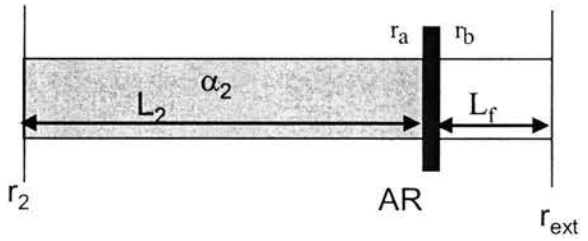

Figure C.1 Passive cavity region of a FILD sensor

where r_2 represents a hard mirror for the bottom DBR, r_{ext} is the reflection coefficient of the external mirror, r_{ar} is the reflection coefficient of the AR coating, L_2 and L_f are the substrate and fluidic caivty thicknesses respectively, and α_2 is the absorption coefficient of the passive cavity region.

Transfer matrix definition

Constants

Mirrors' reflection and tranmissioncoefficients:

$r_1 := \sqrt{0.999}$ $t_1 := \sqrt{1 - r_1 \cdot \overline{r_1}}$

$r_2 := \sqrt{0.8}$ $t_2 := \sqrt{1 - r_2 \cdot \overline{r_2}}$

$r_{ext} := \sqrt{0.99}$ $t_{ext} := \sqrt{1 - r_{ext} \cdot \overline{r_{ext}}}$

Substrate refractive index: $n_{substrate} := 3.527$

Air refractive index: $n_{air} := 1$

Passive cavity parameters $L_2 := 75 \cdot 10^{-6} m$

$\alpha_2 := 5 cm^{-1}$

$L_f := 10 \cdot 10^{-6} m$

The transfer matrix of a dielectric interface is given by

$$T_{interface} = \frac{1}{t}\begin{pmatrix} 1 & \bar{r} \\ r & \bar{t} \\ \frac{}{t} & \frac{}{t} \\ r & 1 \\ \frac{}{t} & \frac{}{\bar{t}} \end{pmatrix}$$

where r is the reflection coefficient of that interface, and t is its transmission coefficient.

Similarly the transfer matrix of a propagation medium is given by

$$T_{prop} = \begin{pmatrix} e^{j\phi} & 0 \\ 0 & e^{-j\phi} \end{pmatrix}$$

where ϕ is the change in phase of an electric field in going from right to left across that medium.

Before determining the individual dielectric elements of the passive part of a FILD sensor, it is important to discuss some properties of an AR coating.

An antireflection coating is generally coated on a dielectric interface between two medi in order to prevent any back reflection at that interface. The refractive index of the AR coating is the square root of the product of refractive indices of the two media at the interface.

In case of a FILD sensor, an AR coating is designed for null reflection between air and substrate. Thus

$$n_{ar} := \sqrt{n_{substrate} \cdot n_{air}}$$

The AR coating has two dielectric interfaces, one with the substrate and the other with fluidic cavity medium. The key idea behind the operation of an AR coating is to obtain

destructive interference between the reflections at these two interfaces. For this reason, the propagation medium of this interface is chosen to be a quarter wavelength thick.The reflection coefficients of the two dielectric interfaces of the AR coating are given by

$$r_a := \frac{n_{substrate} - n_{ar}}{n_{substrate} + n_{ar}} \qquad r_b(n) := \frac{n_{ar} - n}{n_{ar} + n}$$ where n is the fluid index

and corresponding transmission coefficients as

$$t_a := \sqrt{1 - r_a \cdot \overline{r_a}} \qquad t_b(n) := \sqrt{1 - r_b(n) \cdot \overline{r_b(n)}}$$

Now determining the transfer matrices of all the elements

Trasfer matrices of dielectric interfaces

Mirror 2 $$T_2 := \begin{pmatrix} \frac{1}{t_2} & \frac{\overline{r_2}}{\overline{t_2}} \\ \frac{r_2}{t_2} & \frac{1}{\overline{t_2}} \end{pmatrix}$$

External mirr $$T_{ext} := \begin{pmatrix} \frac{1}{t_{ext}} & \frac{\overline{r_{ext}}}{\overline{t_{ext}}} \\ \frac{r_{ext}}{t_{ext}} & \frac{1}{\overline{t_{ext}}} \end{pmatrix}$$

AR interfaces: $$T_{ra} := \begin{pmatrix} \frac{1}{t_a} & \frac{\overline{r_a}}{\overline{t_a}} \\ \frac{r_a}{t_a} & \frac{1}{\overline{t_a}} \end{pmatrix} \qquad T_{rb}(n) := \begin{pmatrix} \frac{1}{t_b(n)} & \frac{\overline{r_b(n)}}{\overline{t_b(n)}} \\ \frac{r_b(n)}{t_b(n)} & \frac{1}{\overline{t_b(n)}} \end{pmatrix}$$

Transfer matrices of propagation media:

$\phi_s := 0 \qquad \phi_f := 0$ assuming that phases are modulo of 2π, that is, constructive interference for the substrate and fluidic cavity,

$$T_{substrate} := \begin{pmatrix} e^{i\cdot\phi_s + \frac{\alpha_2 \cdot L_2}{2}} & 0 \\ 0 & e^{-i\cdot\phi_s - \frac{\alpha_2 \cdot L_2}{2}} \end{pmatrix} \qquad T_{fluid} := \begin{pmatrix} e^{i\cdot\phi_f} & 0 \\ 0 & e^{-i\cdot\phi_f} \end{pmatrix}$$

$$T_{ar} := \begin{pmatrix} i & 0 \\ 0 & -i \end{pmatrix}$$ Assuming destructive interference inside the AR coating

Calculating the effective reflection coefficient for the AR coating,

$$T_{ar\_coating}(n) := T_{ra} \cdot T_{ar} \cdot T_{rb}(n)$$

$$r_{ar}(n) := \frac{T_{ar\_coating}(n)_{1,0}}{T_{ar\_coating}(n)_{0,0}}$$

which is also equal to $$r_{ar}(n) := \frac{r_a - r_b(n)}{1 - r_a \cdot r_b(n)}$$

Now since the reflections from r_2, r_{ext} and r_{ar} interfere constructively, the effective reflection coefficient can be calculated as

$$r_3(n) := \frac{r_{ar}(n) + r_{ext}}{1 + r_{ar}(n) \cdot r_{ext}}$$ for AR coating and external mirror

and $$r_{eff}(n) := \frac{r_2 + r_3(n)}{1 + r_2 \cdot r_3(n)}$$ for complete passive dielectric structure

Now plotting the effective reflectance from the passive cavity as a function of fluid ir

$$n := 1, 1.01 .. 1.5$$

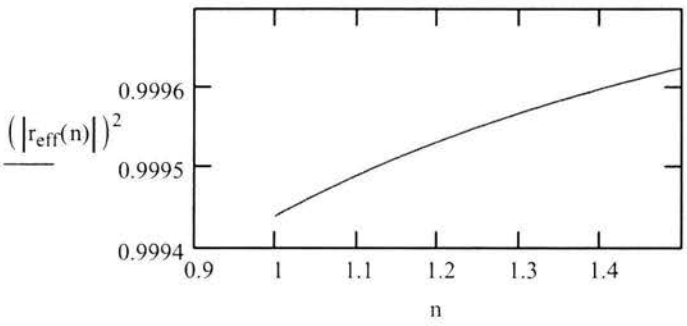

It can be seen from the above plot, the effective reflectance from the passive dielectric cavity increases with increase in fluid index. The increase in reflection from an end mirror leads to lower threshold currents and slope efficiencies of a laser resonator. Since most of the FILD sensors exhibited a trend of increase in slope efficiency and decrease in threshold current with increase in fluid index, thus it can be said that only considering this phenomenon does not completely explain the physics of a FILD sensor.

Appendix D

Transverse confinement factor analysis by using ray matrix method

This appendix is a MathCAD sheet which calculates the modulation of the transverse confinement factor at the gain region of the FILD sensor, by performing a beam propagation analysis using an ABCD matrix method. In this analysis, an ABCD matrix model is constructed for the resonator structure shown in Figure 6.3(b). The resonator is redrawan here in Figure D.1 The author greatly acknowledge Dr.Lear's help in presenting these calculations in the form of an Appendix.

The ABCD matrix approach used to analyze the laser beam's transverse confinement in the FILD sensor is fairly simple. An ABCD matrix of the complete resonator is constructed by cascading matrices of the individual elements, which are the curved mirror (thermal mirror), gain region, and the propagation media (substrate and fluidic cavity).

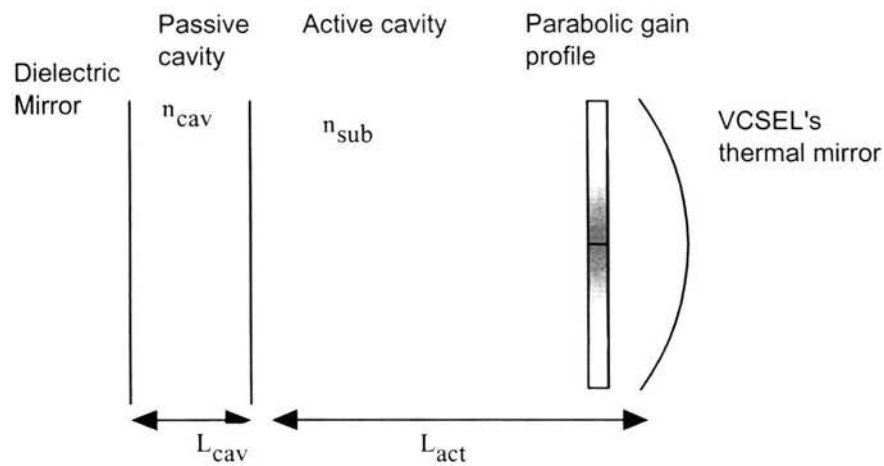

Figue D.1

The transverse confinement of a laser beam at the gain region is calculated by propagating a fundamental order Gaussian beam inside the resonator, and analyzing the beam overlap at the gain region. The fundamental order Gaussian beam is propagated by determining the values of the complex 'q-parameter' at the end mirrors.

The 'q-parameter' is defined as the complex radius of curvature of a Gaussian beam, and it contains information about the beam spot size and the radius of curvature of the beam's wavefront at a particular position. The 'q-parameter' or the complex radius of curvature of a Gaussian beam is analogous to the radius of curvature of a spherical beam under the paraxial

approximation. A paraxial spherical wave has infinite energy in its transverse plane, whereas the amplitude of a Gaussian spherical decays radially from the center of the beam. In order to account for the decay of electric field, the radius of curvature of a paraxial spherical wave is replaced by a complex quantity to covert it into a Gaussian sphreical wave, and thus the name "complex radius of curvature" can be explained.

The expression for q parameter is given by

$$\frac{1}{q(z)} = \frac{1}{R(z)} - i\cdot\frac{\lambda}{\pi\cdot w(z)^2}$$

where R(z) is the real radius of curvature of a Gaussian wave and w(z) is the waist of the beam at plane z and λ is the free space wavelength.

The q parameter is first determined at one of the end mirrors by propagating a Gaussian beam for one round-trip inside the resonator, and the condition that the beam radius is conserved after one round-trip helps in determining a q value at that mirror.

From the complex q parameter values, an electric field distribution can be determined at specific transverse planes by using the Gaussian beam formulas. The electric field distribution at the gain region is analyzed as a function of refractive index of the fluid. From this distribution, the overlap of the laser beam with the gain region is analyzed, and the transverse confinement factor is evaluated.

This MathCAD sheet starts with definitions of ABCD matrices of all the dielectric elements, which is followed by a definition of the parabolic gain profile. Next are the calculations for q parameter and beam waist at the gain region. This is further followed by defintion of transverse confinement factor. At the end of this appendix, the modal gain equation of a FILD sensor is analyzed and expressions for gain threshold and slope efficiency are determined as functions of transverse confinement factor.

Constants

Lengths

$L_{sub} := 75\cdot10^{-6}\ m$	substrate	$\lambda_o := 980\cdot10^{-9}\ m$	Wavelength of laser diode
$L_{ext} := 85\cdot10^{-6}\ m$	complete external cavity	$k_0 := \frac{2\cdot\pi}{\lambda_o}$	Wave vector
$L_g := 50\cdot10^{-9}\ m$	Quantum well gain region	$n_{sub} := 3.525$	Refractive index of substrate
$L_{short} := \lambda_o$	VCSEL cavity		

Reflection and transmission coefficients:

$r_{ext} := \sqrt{0.98}$ $\quad t_{ext} := \sqrt{1 - r_{ext}^2}$ External mirror

$r_{bot} := \sqrt{0.8}$ $t_{bot} := \sqrt{1 - r_{bot}^2}$ Bottom DBR

$r_{top} := \sqrt{0.99}$ $t_{top} := \sqrt{1 - r_{top}^2}$ Top DBR

Gain and loss coefficients:

$\alpha_{sub} := 500 \ m^{-1}$ Substrate loss coefficient

$\alpha_g := 3 \cdot 10^5 \ m^{-1}$ Absorption loss coefficient at the gain region (under the implanted region)

$\alpha_{short} := 500 \ m^{-1}$ Absorption coefficient representing distributed losses inside the VCSEL (short) cavity

$g_{max} := 2 \cdot 10^5 \ m^{-1}$ Maximum gain at the center of laser diode

$x_{edge} := 50 \cdot 10^{-6} \ m$ Edge of the gain aperture from the center of laser diode (100μm gain aperture diameter)

ABCD marices of dielectric elements

External cavity

$$M_{ext}(L_{ext}) := \begin{pmatrix} 1 & L_{ext} \\ 0 & 1 \end{pmatrix}$$

Thermal mirror

$$M_{mirr}(R) := \begin{pmatrix} 1 & 0 \\ \frac{-2 \cdot n_{sub}}{R} & 1 \end{pmatrix}$$

where L_{ext} is the normalized external cavity length, given by

$$L(L_f, n_f) := \frac{L_{sub}}{n_{sub}} + \frac{L_f}{n_f}$$

Thus for a 10μm fluidic cavity length, we get

$L_{air} := L(10^{-5}, 1)$ $L_{water} := L(10^{-5}, 1.33)$

The ABCD matric of parabolic gain profile is discussed as under:

Parabolic gain profile

The gain region is assumed to have a parabolic gain profile. Figure D.2 shows a plot of the gain coefficient as a function of radial distance from the center of the laser diode. It is also assumed that there is maximum gain at the center of the diode and it decreases parabolically away from the center. At the edge of the gain aperture, there is loss due to absorption under the implanted region.

$$g(x) := \begin{cases} g_{max} - \dfrac{g_{max}}{x_{edge}^2} \cdot x^2 & \text{if } (x \geq -x_{edge}) \wedge (x \leq x_{edge}) \\ -\alpha_g & \text{if } (x < -x_{edge}) \\ -\alpha_g & \text{if } (x > x_{edge}) \end{cases}$$

Gain profile at the gain region

$$x := -1 \cdot 10^{-4}, -9.9 \cdot 10^{-5} .. 1 \cdot 10^{-4}$$

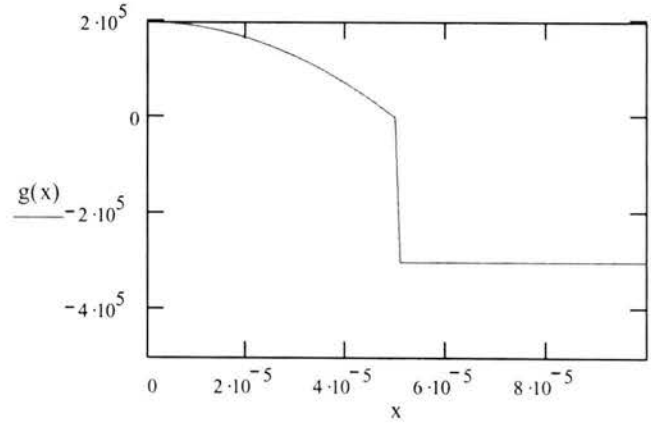

Figure D.2

$$\alpha_2 := \frac{2 \cdot g_{max}}{x_{edge}^2}$$

α_2 is the second derivative of the gain function which is calculated to determine the equivalent ABCD matrix of the gain region

The length d_q is the thickness of the quantum wells, which corresponds to the gain region. Thus from the formulae given in Reference [1] , the ABCD ray matrix for the gain region can be defined as

$$\gamma := \sqrt{\frac{i\alpha_2}{n_{sub} \cdot k_0}} \qquad M_g := \begin{pmatrix} \cos(\gamma \cdot L_g) & \dfrac{\sin(\gamma \cdot L_g)}{n_{sub} \cdot \gamma} \\ -n_{sub} \cdot \gamma \cdot \sin(\gamma \cdot L_g) & \cos(\gamma \cdot L_g) \end{pmatrix} \qquad M_{unity\_gain} := \begin{pmatrix} 1 & 0 \\ 0 & 1 \end{pmatrix}$$

Complete unfolded resonator

Under stable operating condition of a resonator, the electric field distribution at any specific transverse plane would repeat itself after each round-trip inside the resonator. Thus, the 'q-parameter', which contains information about the field distribution at specific plane, should also repeat itself after one round-trip.

An ABCD matrix for the complete unfolded resonator is determined by unfolding the FILD sensor resonator and cascading the matrices of individual dielectric elements.

$$M(L,R) := M_{ext}(L)\cdot M_g\cdot M_{mirr}(R)\cdot M_g\cdot M_{ext}(L)$$

Now the normalized q parameter is transformed by the following formula

$$q_2 = \frac{A\cdot q_1 + B}{C\cdot q_1 + D}$$

For the matrix M, defined above for the unfolded resonator $q_2 = q_1$ which gives

$$q_1(L,R) := \left[\frac{\frac{M(L,R)_{0,0} - M(L,R)_{1,1}}{M(L,R)_{1,0}} + \sqrt{\left(\frac{M(L,R)_{0,0} - M(L,R)_{1,1}}{M(L,R)_{1,0}}\right)^2 + \frac{4\cdot M(L,R)_{0,1}}{M(L,R)_{1,0}}}}{2}\right]$$

In order to determine the beam waist at the gain region, the above q parameter must be transformed to that plane. The corresponding ABCD matrix for the q transformation is

$$M_f(L,R) := M_{mirr}(R)\cdot M_g\cdot M_{ext}(L)$$

q parameter at the gain region is given by

$$q_2(L,R) := \frac{M_f(L,R)_{0,0}\cdot q_1(L,R) + M_f(L,R)_{0,1}}{M_f(L,R)_{1,0}\cdot q_1(L,R) + M_f(L,R)_{1,1}}$$

which gives the following expression for beam waist at the gain region

$$w_2(L,R) := \sqrt{\frac{-\lambda_o}{\pi\cdot \mathrm{Im}\left(q_2(L,R)^{-1}\right)}}$$

Now plotting the beam waist as a function of refractive index of the fluidic cavity

$$n_{cav} := 1, 1.01 .. 1.5$$

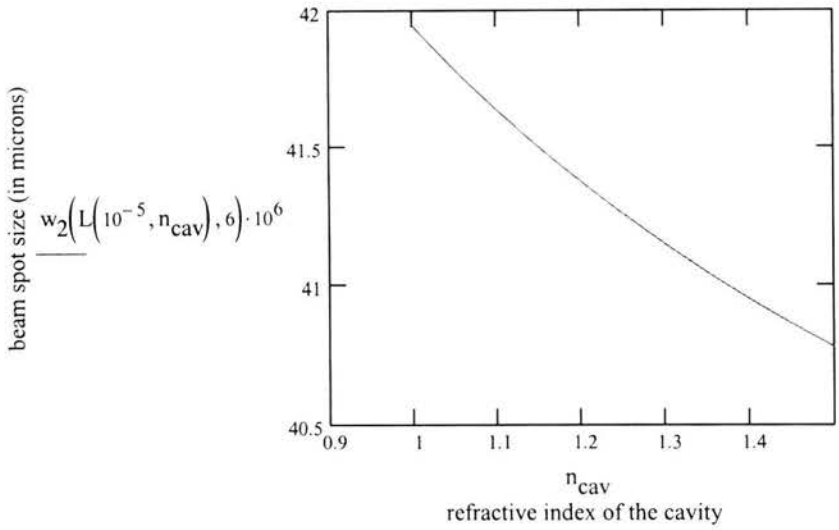

Figure D.3

It can be seen here that as the fluid index increases, the beam spot size decreases, resulting in a better overlap with the gain region.

As already discussed in Chapter 6, thermal mirror's radius of curvature is a function of device operating temperature. From the calculations and themal resistance measurements discussed in Chapter 6, it was found that the thermal mirror's radius of curvature must be ~6m under both air and water fluidic conditions. It is for this reason, that the value of R is assumed to be equal to 6m in this appendix.

Also, it is however interesting to determine if the beam profile at the gain region is dominated by the thermal mirror or due to gain guiding effect. In order to determine this, the beam waist at the gain region is analyzed as a function of thermal mirror radius of curvature. Higher values of thermal mirror's radius indicates lower thermal lensing effects. The figures below, plot beam waist at the gain region at a fluid index equal to 1, as a funtion of R. Figure D.4 (a) plots the beam waist with the consideration of parabolic gain guiding effect, and Figure D.4 (b) plots the same beam waist vs. R with a consideration that there is unity or no gain at the gain region.

Thus the ABCD matrix for the unity gain FILD sensor is

$$M_{ug}(L,R) := M_{ext}(L)\cdot M_{unity\_gain}\cdot M_{mirr}(R)\cdot M_{unity\_gain}\cdot M_{ext}(L)$$

The corresponding q parmeter and beam waist expressions are

$$q_{1\_ug}(L,R) := \left[\frac{M_{ug}(L,R)_{0,0} - M_{ug}(L,R)_{1,1}}{M_{ug}(L,R)_{1,0}} + \sqrt{\left(\frac{M_{ug}(L,R)_{0,0} - M_{ug}(L,R)_{1,1}}{M_{ug}(L,R)_{1,0}} \right)^2 + \frac{4 \cdot M_{ug}(L,R)_{0,1}}{M_{ug}(L,R)_{1,0}}} \right] \cdot \frac{1}{2}$$

$$M_{f\_ug}(L,R) := M_{mirr}(R) \cdot M_{unity\_gain} \cdot M_{ext}(L)$$

$$q_{2\_ug}(L,R) := \frac{M_{f\_ug}(L,R)_{0,0} \cdot q_{1\_ug}(L,R) + M_{f\_ug}(L,R)_{0,1}}{M_{f\_ug}(L,R)_{1,0} \cdot q_{1\_ug}(L,R) + M_{f\_ug}(L,R)_{1,1}}$$

$$R := 1,2..1000$$

$$w_{2\_ug}(L,R) := \sqrt{\frac{-\lambda_o}{\pi \cdot Im\left(q_{2\_ug}(L,R)^{-1}\right)}}$$

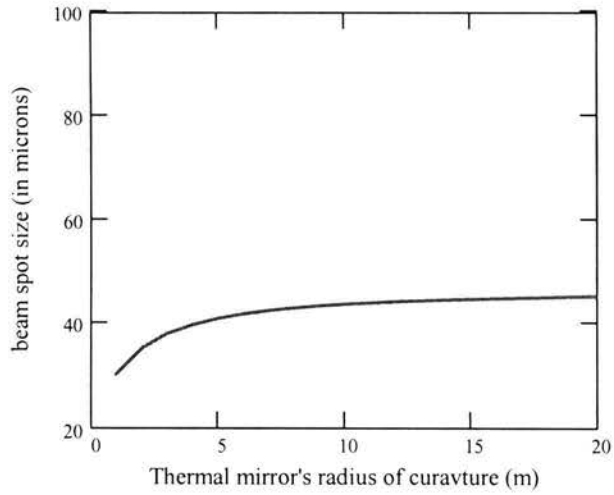

Figue D.4 (a)

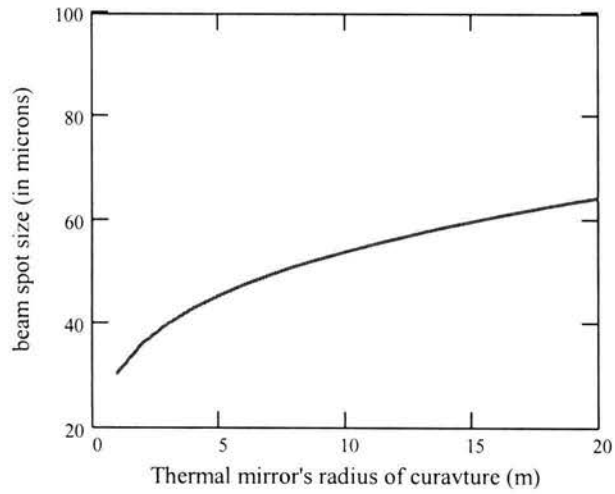

Figue D.4 (b)

It can be seen from the Figure D.4 (a), at R = 6m, the beam waist at the gain region starts to saturate due to gain guiding. On the other hand, under unity gain conditions, the beam waist would increase as R increase, indicating that at R = 6m the gain guiding effect dominates.

Now from the formulae given in Reference [1], the electric field distribuition can be determined at the gain region and is shown below.

$$u_2(x,L,R) := e^{\left(\frac{-i\cdot x^2\cdot\pi}{q_2(L,R)\cdot\lambda_o}\right)}$$

$$\frac{\left(\left|u_2(x,L_{air},6)\right|\right)^2}{\left(\left|u_2(x,L_{water},6)\right|\right)^2}$$

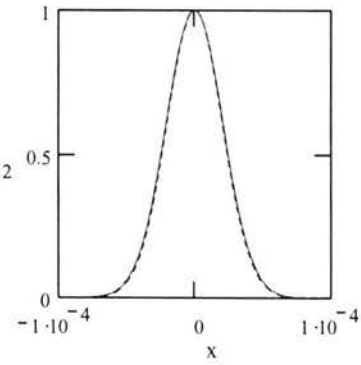

Figure D.5

The transverse confinement factor can be calculated by determining the overlap of the Gaussian beam with the gain region. This is shown below.

$$n_{moaw} := 1, 1.1 .. 1.5$$

$$\Gamma_{trans}(L,R) := \frac{\int_0^{2\cdot\pi}\int_0^{x_{edge}} \left(\left|u_2(r,L,R)\right|\right)^2\cdot r\cdot\frac{g(r)}{g_{max}}\,dr\,d\theta}{\int_0^{2\cdot\pi}\int_0^{10^{-3}} \left(\left|u_2(r,L,R)\right|\right)^2\cdot r\,dr\,d\theta}$$

$\Gamma_{trans}\left(L\left(10^{-5}, n_{cav}\right), 6\right)$

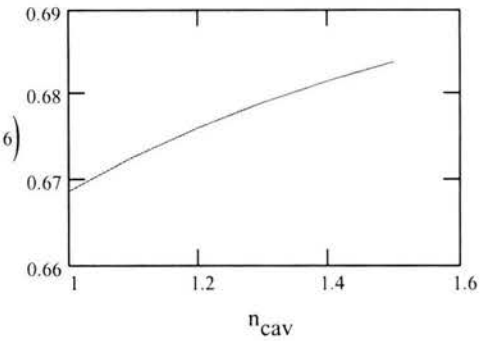

Figure D.6

It can be seen from the above plot, that the transverse confinement factor Γ_{xy} increases with an increase in the fluidic cavity refractive index. The next step is to analyze the effect of modulation of the transverse confiment on the FILD sensor's threshold gain and slope efficiency.

The FILD sensor is a coupled cavity resonator. In order to analyze the round-trip gain the extenal cavity elements (passive elements) are lumped together, as shown in the Figures D.7 (a) and (b). The mirror r_{eff} represents the complete passive cavity of the FILD sensor, including the substrate and fluidic cavity.

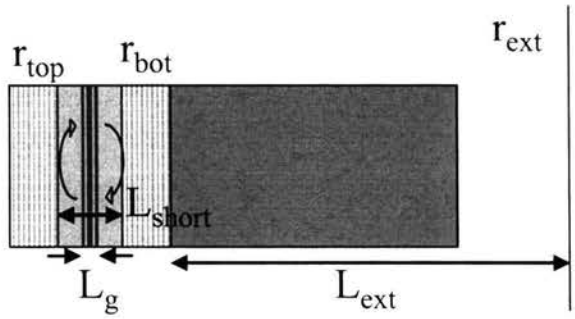

Figure D.7 (a) FILD sensor resonator

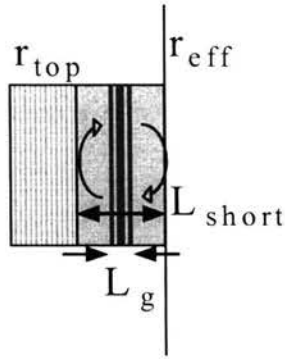

Figure D.7 (b) Simplified FILD sensor resonator with lumped passive cavity

The round trip gain equation can be written as

$$r_{top}\cdot\exp\left[\Gamma_{xy}\cdot g_{th}\cdot L_g-\left(1-\Gamma_{xy}\right)\cdot\alpha_g\cdot L_g\right]\cdot\exp\left(-\alpha\cdot L_{short}\right)\cdot r_{eff}=1$$

where g_{th} is the material gain at threshold condition, α_g is the absorption loss coefficient at the gain region, α is the distributed loss coefficient, L_g is the width of quantum well region, and L_{short} is the VCSEL cavity (short cavity) length.

Assuming that there are no fluid induced absorption losses or modulation of scattering losses at the substrate-fluidic cavity interface, r_{eff} will have a constant value, which can be easily calculated by Transfer matrix method.

$$r_{eff}:=\frac{r_{bot}+r_{ext}\cdot\exp\left(-\alpha_{sub}\cdot L_{ext}\right)}{1+r_{bot}\cdot r_{ext}\cdot\exp\left(-\alpha_{sub}\cdot L_{ext}\right)}$$

Assuming that the reflections from bottom DBR and external mirror interfere constructively

From the above explanation, and the dependence of the transvese confinement factor Γ_{xy} on fluid index, the following expression can written for material gain at the threshold condition.

$$g_{th}\left(\Gamma_{xy}\right):=\left[\frac{\ln\left(\frac{1}{r_{top}\cdot r_{eff}}\right)}{\Gamma_{xy}\cdot L_g}+\frac{\alpha_{short}\cdot L_{short}}{\Gamma_{xy}\cdot L_g}+\frac{\left(1-\Gamma_{xy}\right)\cdot\alpha_g}{\Gamma_{xy}}\right]$$

$g_{th}\left(\Gamma_{trans}\left(L\left(10^{-5},n_{cav}\right),6\right)\right)$

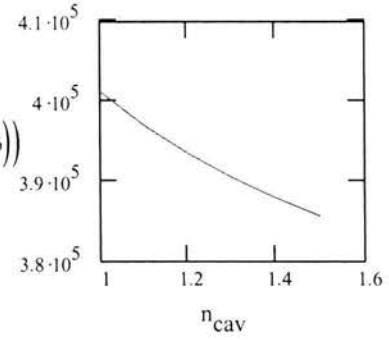

On the other hand, for the differential slope efficiency, losses incurred in the external cavity need to be considered carefully. From the formulae discussed in Reference[2], it can be calculated as

$$\eta_d=\frac{\ln\left(\frac{1}{r_{top}\cdot r_{eff}}\right)}{\ln\left(\frac{1}{r_{top}\cdot r_{eff}}\right)+\alpha_{short}\cdot L_{short}+\left(1-\Gamma_{xy}\right)\cdot\alpha_g\cdot L_g}\cdot F_{ext}$$

where F_{ext} is given by

$$F_{ext} := \frac{t_{eff}^{2}}{\left(1 - r_{eff}^{2}\right) + \frac{r_{eff}}{r_{top}} \cdot \left(1 - r_{top}^{2}\right)}$$

t_{eff} can be easily calculated by using the Transfer matrix method. It is given by

$$t_{eff} := \frac{t_{bot} \cdot t_{ext} \cdot \exp\left(-\alpha_{sub} \cdot L_{ext}\right)}{1 + r_{bot} \cdot r_{ext} \cdot \exp\left(-2 \cdot \alpha_{sub} \cdot L_{ext}\right)}$$

$$\eta_d\left(\Gamma_{xy}\right) := \frac{\ln\left(\frac{1}{r_{top} \cdot r_{eff}}\right)}{\ln\left(\frac{1}{r_{top} \cdot r_{eff}}\right) + \alpha_{short} \cdot L_{short} + \left(1 - \Gamma_{xy}\right) \cdot \alpha_g \cdot L_g} \cdot F_{ext}$$

$\eta_d\left(\Gamma_{trans}\left(L\left(10^{-5}, n_{cav}\right), 6\right)\right)$

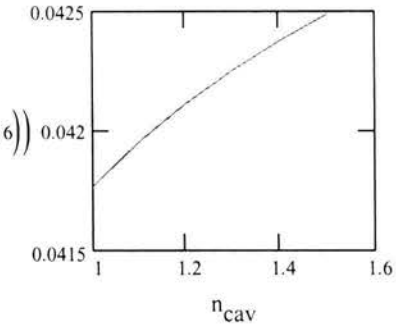

Note that the threshold gain decreases, and slope efficiency increases with an increase in fluid index of the fluidic cavity, which matches with most common trend of the FILD sensor. It is however intersting to determine if the above calculations qualitatively match with the experimental data. In Table 5.1, it was observed that the FILD sensors that exhibited the trend of increase in slope efficiency and decrease in threshold current, showed an average relative increse in slope efficiency by 60% and relative decrease in threshold current by 16%.

From the above calculations on slope efficiency and threshold current, the relative change in slope efficiency and threshold current are calculated.

$$\frac{\eta_d\left(\Gamma_{trans}\left(L_{water}, 6\right)\right) - \eta_d\left(\Gamma_{trans}\left(L_{air}, 6\right)\right)}{\eta_d\left(\Gamma_{trans}\left(L_{air}, 6\right)\right)} \cdot 100 = 1.266$$

$$\frac{g_{th}\left(\Gamma_{trans}\left(L_{air}, 6\right)\right) - g_{th}\left(\Gamma_{trans}\left(L_{water}, 6\right)\right)}{g_{th}\left(\Gamma_{trans}\left(L_{air}, 6\right)\right)} \cdot 100 = 2.875$$

The above calcuations shows that theoretically (with consideration of "transverse beam confinement analysis"), the slope efficiency should increase by only 1.3% and the the threshold current should decrease by only ~3%. Here we have assumed that threshold material gain is directly proportional to the current density.

Thus from the above results and from the data presented in Table 5.1, it can be said that, although this phenomenon conforms to the trend of experimental data, but qualitatively, the results are off by order of magnitude.

References:

[1] Anthony E. Siegman, *"Lasers"* Chapters 14-15, University Science Books, 1986

[2] Larry A.Coldren and Scott W. Corzine, "*Diode Lasers and Photonic Integrated Circuits*", Wiley Series in Microwave and Optical Engineering, Chapter 3

Appendix E
Slope efficiency and threshold current analysis of a FILD sensor utilizing scattering loss dependence on fluid index

This appendix is a MathCAD sheet which presents calculations of the slope efficiency and threshold current of a FILD sensor by utilizing the transfer matrix method to account for scattering losses inside the fluidic cavity. The author greatly acknowledge the help and guidance provided by Dr. Lear in presenting these calculations.

As discussed in detail in Section 6.2.5, scattering losses are caused due to the rough surface of the AR coatings at the backside of a NECSEL substrate. AFM measurements showed that the RMS roughness values of some of the NECSEL diodes used for constructing FILD sensors range from 5nm to 40 nm.

This MathCAD sheet starts with a description of a FILD sensor resonator. This is followed by the definition of transfer matrices of each of the sensor resonator's elements, like mirrors, propagation media, gain region, dielectric interfaces, etc. A transfer matrix is also defined for consideration of scattering losses.

The FILD sensor resonator is shown in Figure E.1.

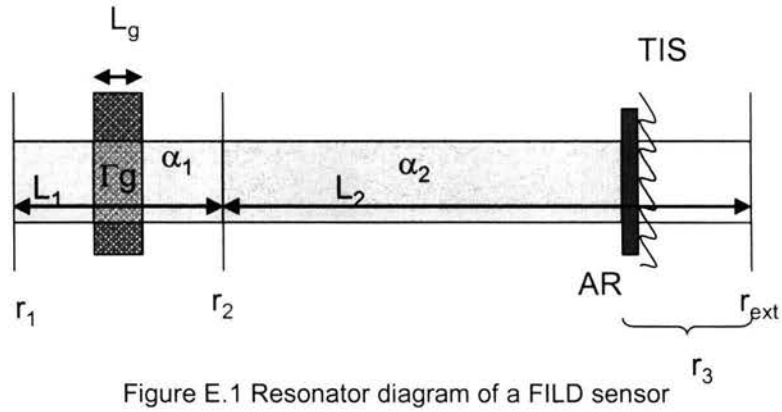

Figure E.1 Resonator diagram of a FILD sensor

Figure E.1, shown above is similar to the Figure 6.1 (b), except the DBR mirrors are represented by hard mirrors with reflecition coefficients r_1 and r_2.

r_{ext} is the reflection coefficient of external mirror, r_3 is the combined reflection coefficient of the AR coating and external mirror, L_1 is the cavity length of a NECSEL diode, L_2 is the external cavity length which includes substrate thickness and fluidic caivty, α_1 and α_2 are the absorption coefficients of the active and passive cavity regions, L_g is the length of the gain region, Γg is the modal gain and TIS is the total integrated scattering loss parameter, which is defined in Section 6.2.5.

Transfer matrix definition

Constants

Mirrors' reflection and tranmissioncoefficients:

$r_1 := 0.99 \quad t_1 := \sqrt{1 - r_1 \cdot \overline{r_1}}$

$r_2 := 0.8$

$r_{ext} := 0.98 \quad t_2 := \sqrt{1 - r_2 \cdot \overline{r_2}}$

Substrate refractive index: $n_s := 3.527$

AR coating RI: $n_{ar} := \sqrt{n_s}$

Gain region length $L_g := 60 \cdot 10^{-9} \cdot m$

Modal gain $\Gamma g := 2000 \cdot cm^{-1}$

VCSEL cavity length $L_1 := 2 \cdot 10^{-6} \cdot m$

VCSEL distributed loss $\alpha_1 := 20 \cdot cm^{-1}$

Substrate/external cavity length $L_2 := 100 \cdot 10^{-6} \cdot m$

Substrate distributed loss $\alpha_2 := 5 \cdot cm^{-1}$

Scattering loss $TS(n, \sigma) := \left[\frac{2 \cdot \pi \cdot \sigma \cdot (n_{ar} - n)}{972}\right]^2$

Here σ is the RMS rougness (in nm) of the rough surface, and (n_{ar}-n) is index difference at the interface, and 972 is the operating wavelength (also in nm)

Antireflection coating parameters:

$$r_a := \frac{n_s - n_{ar}}{n_s + n_{ar}} \qquad r_b(n) := \frac{n_{ar} - n}{n_{ar} + n} \qquad r_{ar}(n) := \frac{r_a - r_b(n)}{1 - r_a \cdot r_b(n)}$$

$$r_3(n) := \frac{r_{ext} + r_{ar}(n)}{1 + r_{ext} \cdot r_{ar}(n)} \quad \text{and} \quad t_3(n) := \sqrt{1 - r_3(n) \cdot \overline{r_3(n)}}$$

Here r_{ar} and r_3 are calculated using simple mirror cascading formulas [1], with assumptions that antireflection coating creates destructive interference between its two surfaces, and constructive interference between r_{ar} and r_{ext}.

The dependence of a FILD sensor's slope efficiency and threshold current on fluid refractive index is determined by using simple laser gain equations, where the modal gain of a laser is equated with all the internal losses and mirror losses. The slope efficiency is calculated by determining the amount of mirror loss from the output coupler and dividing it by sum of total internal losses and mirror losses. [2]

In order to determine mirror losses of a FILD sensor, all dielectric elements starting from mirror r_2 to r_3 are compressed into one effective mirror, M_{eff}, with effective reflection coefficient r_{eff}. The calculation of r_{eff} assumes that reflections from mirror r_2 and r_3 interfere constructively at the operating wavelength.

The transfer matrix of scattering interface can be defined as

$$M_{TIS} = \begin{pmatrix} \frac{1}{\sqrt{1 - TIS}} & 0 \\ 0 & \sqrt{1 - TIS} \end{pmatrix}$$

Thus by including the above matrix into the calculations shown in Appendix C, the effective reflection coefficient reff can be calculated as

Phase difference across cavity 2 modulo 2π: $\phi := 0$

$$r_{eff}(TIS, n) := \frac{r_2 + r_3(n)\cdot\exp(j\cdot\phi)\cdot\left[\exp\left(-\alpha_2\cdot L_2\right)\cdot(1 - TIS)\right]}{1 + r_2\cdot\left[r_3(n)\cdot\exp(j\cdot\phi)\cdot\left[\exp\left(-\alpha_2\cdot L_2\right)\cdot(1 - TIS)\right]\right]}$$

and similarly the effective transmission coefficient can be calculated as

$$t_{eff}(TIS, n) := \frac{t_2\cdot t_3(n)\cdot\exp(j\cdot\phi)\cdot\left[\exp\left(\frac{-\alpha_2\cdot L_2}{2}\right)\cdot(1 - TIS)\right]}{1 + r_2\cdot r_3(n)\cdot\exp(j\cdot\phi)\cdot\left[\exp\left(-\alpha_2\cdot L_2\right)\cdot(1 - TIS)\right]}$$

The mirror losses are given by

$$\alpha_{m1} := \frac{1}{L_1}\cdot\ln\left(\frac{1}{r_1}\right) \qquad \alpha_{meff}(TIS, n) := \frac{1}{L_1}\cdot\ln\left(\frac{1}{r_{eff}(TIS, n)}\right)$$

It is tempting to calculate the differential quantum efficiency out mirror 3 as

$$\eta_{DQE}(TIS, n) := \frac{\alpha_{meff}(TIS, n)}{\alpha_1 + \alpha_{m1} + \alpha_{meff}(TIS, n)}$$

and the total differential quantum efficiency out mirrors 1 and 3 both as

$$\eta_{DQEtot}(TIS, n) := \frac{\alpha_{m1} + \alpha_{meff}(TIS, n)}{\alpha_1 + \alpha_{m1} + \alpha_{meff}(TIS, n)}$$

but this does not account for the loss in the substrate.

To account for the effective loss in mirror M_{eff}, i.e. the combination of mirrors 2 and 3 along with the substrate loss and the scattering loss, the formulae from the Reference [1] can be used.

They give a correction factor, F. To calculate F, the effective transmission coefficient, t_{eff}, needs to be calculated. This is most easily done using transmission matrices.

$$F(TIS,n) := \frac{t_{eff}(TIS,n)^2}{\left(1 - r_{eff}(TIS,n)^2\right) + \frac{r_{eff}(TIS,n)}{r_1}\cdot\left(1 - r_1{}^2\right)}$$

Again using formulae from Reference [1], the correct differential quantum efficiency of the FILD sensor can be calculated as

$$\eta(TIS,n) := \eta_{DQEtot}(TIS,n)\cdot F(TIS,n)$$

$$TIS := 0, 0.001 .. 1$$

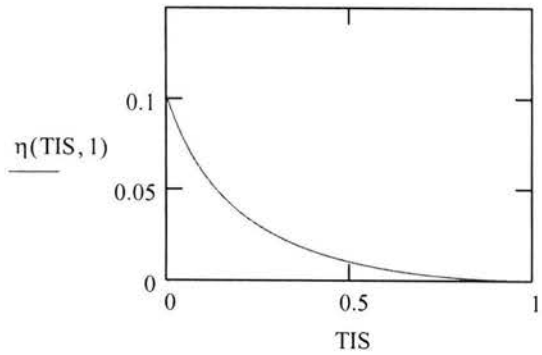

$$n := 1, 1.001 .. n_{ar}$$

The AFM measurments showed that the RMS surface roughness on AR coatings ranged from 5nm to 40nm. Thus for an average RMS roughness of ~20nm, the TIS can be plotted as a function of fluid index as

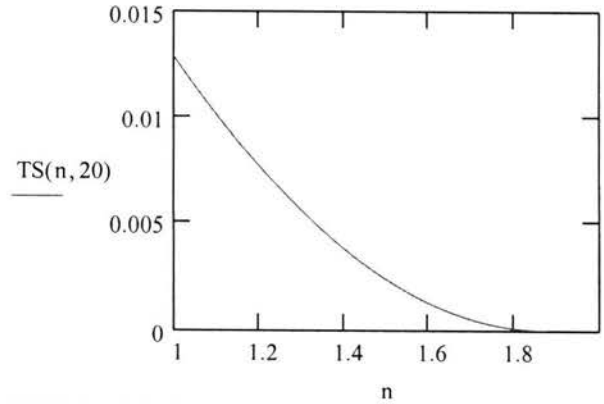

The differential slope efficiency can be plotted as a function of fluid index as

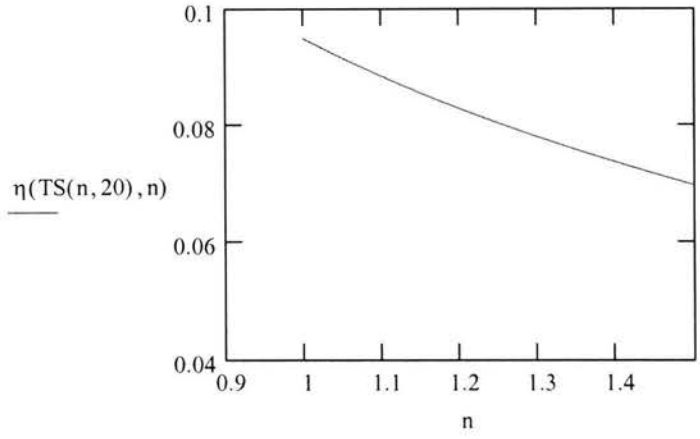

Similarly the material gain at threshold can also be defined and plotted as a function of fluid index, at an average suface roughness of 20nm.

$$\Gamma g_{th}(TIS, n) := \frac{L_1}{L_g} \cdot \left(\alpha_1 + \alpha_{m1} + \alpha_{meff}(TIS, n)\right)$$

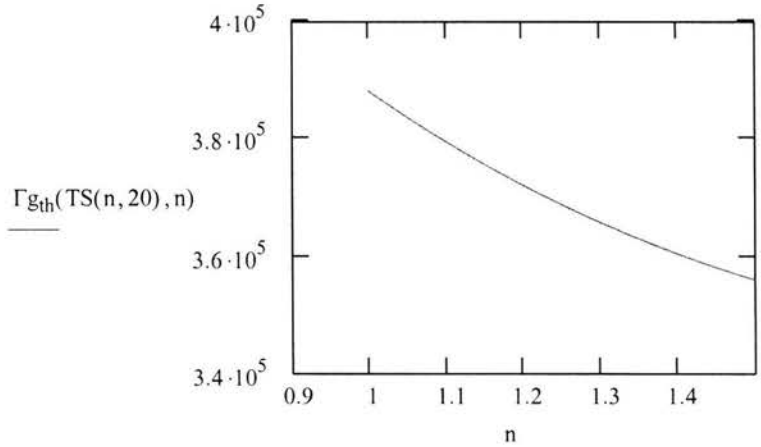

Thus the trend exhibited by this phenomenon is decrease in slope efficiency and gain threshold with increase in fluid index. It is interesting however to determine the trend of this phenomenon is affected by higher or lower surface roughnesses on the AR coating.

The graphs shown below plot the slope efficiency and modal gain at threshold as a function of surface roughness at a constant fluid index (equal to 1).

$\sigma := 0, .01 .. 150$

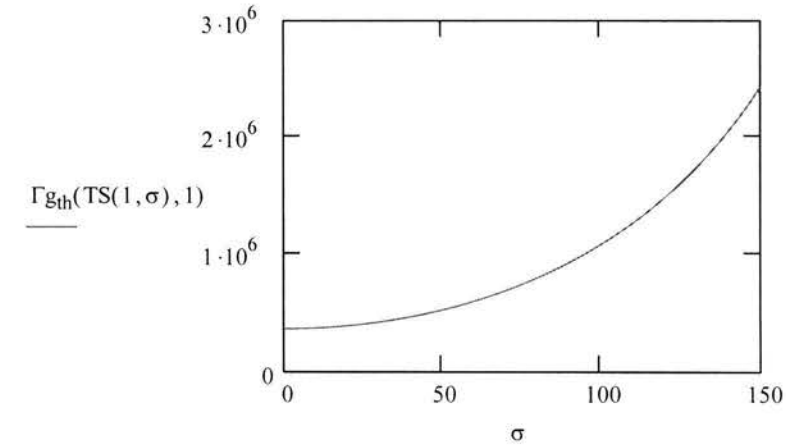

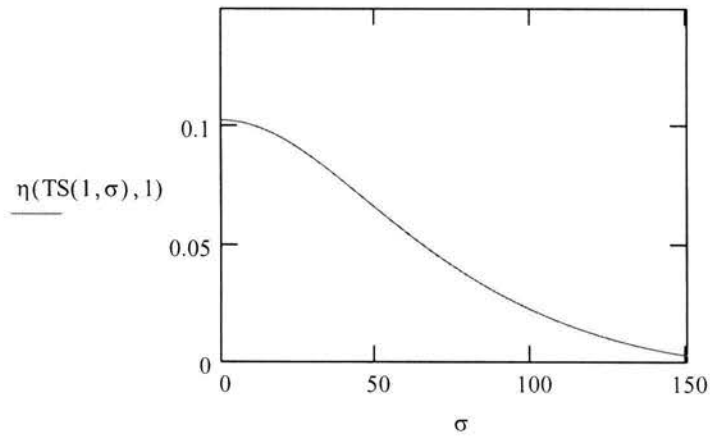

Thus as we would expect higher scatter loss induced by greater surface roughness would result in increase in gain threshold and decrease in slope efficiency of a FILD sensor. There is yet another investigation, which is to determine if the trend of slope efficiency vs fluid index is the same with different levels of surface roughness.

The following figure plots the slope efficiency as a function of fluid index, for surface roughness values ranging from 20nm to 150nm.

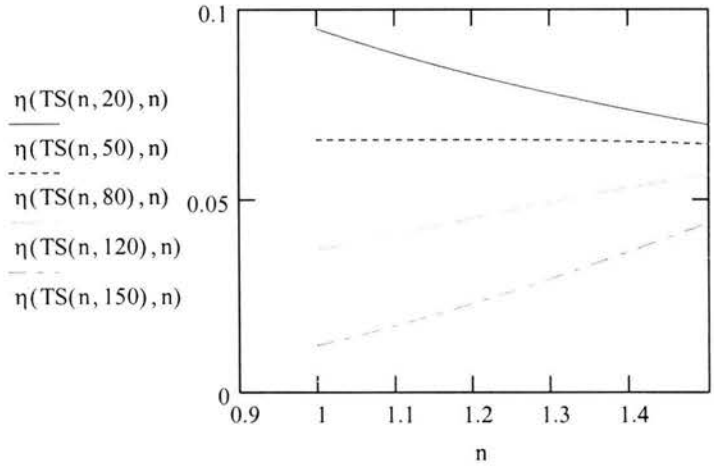

It can be seen here that trend of slope efficiency vs fluid index totally reverses for high surface roughness levels. This can be explained by considering that, at lower surface roughness levels, the antireflection coating is dominant in decreasing the mirror loss with fluid index, but at higher roughness levels, the TIS dominates and the mirror loss increases with fluid index.

Lastly, since the roughness levels measured on various NECSEL diodes range from 5nm to 40nm, and not as high as 8nm or 150nm to exhibit the trend of increase in slope efficiency and decrease in threshold current, it can be said that this theoretical phenomenon does not qualitatively match with the trend of experimental results.

References:

[1] Larry A. Coldren and Scott W. Corzine, *"Diode lasers and photonic integrated circuits"*, Wiley series in Microwave and optical engineering, Section 3.3, page 71

[2] Larry A. Coldren and Scott W. Corzine, *"Diode lasers and photonic integrated circuits"*, Wiley series in Microwave and optical engineering, Chapter 2, page 28